Molecular switch between mammalian MLL complexes dictates response to Menin-MLL inhibition

Yadira M. Soto-Feliciano[1,11,12,†], Francisco J. Sánchez-Rivera[2,11,12,,†], Florian Perner[3,4,5,†], Douglas W. Barrows[1,6], Edward R. Kastenhuber[2], Yu-Jui Ho[2], Thomas Carroll[6], Yijun Xiong[3,4], Disha Anand[3,5], Alexey Soshnev[1], Leah Gates[1], Mary Clare Beytagh[1], David Cheon[1], Shengqing Gu[7,8], X. Shirley Liu[7,8], Andrei V. Krivtsov[3,4], Maximiliano Meneses[9], Elisa de Stanchina[9], Richard M. Stone[10], Scott A. Armstrong[3,4,*], Scott W. Lowe[2,*], C. David Allis[1,*]

[1]Laboratory of Chromatin Biology & Epigenetics, The Rockefeller University, New York, NY 10065, USA.

[2]Cancer Biology and Genetics, MSKCC New York, NY 10065, USA.

[3]Department of Pediatric Oncology, Dana-Farber Cancer Institute, Boston, MA., 02215, USA.

[4]Division of Hematology/Oncology, Boston Children's Hospital and Harvard Medical School, Boston, MA, 02215, USA.

[5]Internal Medicine C, Greifswald University Medical Center, Greifswald, 17475, Germany.

[6]Bioinformatics Resource Center, The Rockefeller University, New York, NY 10065, USA.

[7]Department of Biostatistics and Computational Biology, Dana-Farber Cancer Institute, Harvard School of Public Health, Boston, 02215, MA, USA.

[8]Center for Functional Cancer Epigenetics, Dana-Farber Cancer Institute, Boston, 02215, MA, USA.

[9]Department of Molecular Pharmacology, MSKCC New York, NY 10065, USA.

21 [10]Leukemia Division, Department of Medical Oncology, Dana-Farber Cancer Institute, Boston,
22 MA, 02215, USA.

23 [11]**Current affiliation/address:** David H. Koch Institute for Integrative Cancer Research,
24 Massachusetts Institute of Technology, Cambridge, 02142, Massachusetts, USA

25 [12]**Current affiliation/address:** Department of Biology, Massachusetts Institute of Technology,
26 Cambridge, 02142, Massachusetts, USA

27 † Co-first authors

28 * Co-corresponding authors

29 Correspondence:

30 C. David Allis: The Rockefeller University, Allis Lab, Box #78, 1230 York Avenue, New York, NY
31 10065, USA. Email: alliscd@rockefeller.edu

32 Scott W. Lowe: Memorial Sloan Kettering Cancer Center (MSKCC), Sloan Kettering Institute,
33 Cancer Biology & Genetics Program, New York, NY, 10065, USA. Email: lowes@mskcc.org

34 Scott A. Armstrong: Harvard Medical School, Dana-Farber Cancer Institute, Department of
35 Pediatric Oncology, Boston, MA, 02115, USA. Email: Scott_Armstrong@dfci.harvard.edu

36 Keywords: Menin, MLL, UTX, chromatin, epigenetics, leukemia, CRISPR

ABSTRACT

The chromatin adaptor Menin interacts with oncogenic fusion proteins encoded by *MLL1*-rearrangements (*MLL1*-r), and small molecules that disrupt these associations are currently in clinical trials for the treatment of leukemia. Here, by integrating chromatin-focused and genome-wide CRISPR screens with genetic, pharmacological, and biochemical approaches in mouse and human systems, we discovered a molecular switch between the MLL1-Menin and MLL3/4-UTX chromatin modifying complexes that dictates response to Menin-MLL inhibitors. We show that MLL1-Menin safeguards leukemia survival by impeding binding of the MLL3/4-UTX complex at a subset of target gene promoters. Disrupting the interaction between Menin and MLL1 leads to UTX-dependent transcriptional activation of tumor suppressive genes, including factors that mediate cell cycle arrest and cellular senescence. We show that this epigenetic mechanism is operative in murine and human models of AML, and clinical responses to Menin-MLL inhibition in primary human leukemia are also accompanied by induction of these tumor suppressive genes. We provide proof-of-concept *in vivo* evidence that this mechanism can be rationally exploited to design combination therapies using FDA-approved CDK4/6 inhibitors to mitigate treatment resistance associated with MLL3/4-UTX complex mutations. These findings shed light on the context-dependent and often antagonistic roles that chromatin regulators exhibit in development and disease and provide mechanistic insight for rational design of targeted epigenetic therapies.

INTRODUCTION

Menin is an evolutionarily conserved nuclear factor that associates with chromatin to recruit (adapt) interacting proteins[1], including the Trithorax (*Trx*)-related MLL1 (KMT2A) and MLL2 (KMT2B) histone methyltransferase complexes[2,3] and the MLL1 oncogenic fusion proteins[4], transcription factors (e.g., c-MYC[5], JUND[6,7], SMADs[8,9]), and other chromatin-bound proteins (e.g.,

60 LEDGF[10] (reviewed in ref. 11)). However, the detailed underlying molecular mechanisms and
61 functional interactions associated with Menin remain elusive.

62 Menin is a core subunit of the MLL1 (ref. 12) and MLL2 complexes[2] and is responsible for targeting
63 these to chromatin[3]. Menin is required for MLL1/MLL2-dependent H3K4 trimethylation of *HOX*
64 genes and their stable long-term expression during development[2,13]. Menin has context-specific
65 functions in human diseases, acting as a tumor suppressor in neuroendocrine malignancies[14,15]
66 and in certain skin[16], lung[17], and CNS tumors[18], and as an oncogenic cofactor in other cancers,
67 including hepatocellular carcinoma[19] and *MLL1*-rearranged (*MLL1*-r) leukemias[4,20]. Furthermore,
68 over 1000 germline and somatic *MEN1* variants have been identified, some of which are linked
69 to cancer predisposition[21]. Owing to its pro-oncogenic roles in mixed lineage leukemia and other
70 malignancies, small molecule inhibitors targeting the Menin-MLL1 and Menin-MLL2 protein-
71 protein interactions have shown great promise for intercepting and treating different types of
72 cancers[19,22-27]. Notably, three structurally different Menin-MLL inhibitors have recently entered
73 clinical trials (NCT04065399, NCT04067336, NCT04811560) and at least one has been granted
74 fast track designation by the FDA for treatment of relapsed/refractory acute leukemias[25,27,28].
75 Thus, an understanding of the molecular mechanisms of action of these drugs would facilitate the
76 development of biomarkers to predict therapeutic response and resistance, and lead to rational
77 design of more effective combination treatments.

78 # RESULTS

79 **Functional interplay between MLL1-Menin and MLL3/4-UTX chromatin modifying**
80 **complexes**

81 We performed a series of CRISPR-based genetic screens to molecularly dissect the dependency
82 of *MLL1*-r leukemias to Menin and identify factors that dictate response and resistance to Menin-

83 MLL inhibitors. First, we screened a chromatin-focused CRISPR library in Cas9-expressing
84 Menin-dependent mouse leukemia cells driven by a human MLL-AF9 transgene (hereafter
85 referred to as MLL-AF9 cells)[29] (**Fig. 1A, Extended Data Fig. 1A-D, Supplementary Table 1**).
86 Library-transduced cells were cultured in media with DMSO (vehicle) or the Menin-MLL inhibitor
87 MI-503 (ref. 22) for 12 cell population doublings (CPDs), followed by screen deconvolution using
88 next-generation sequencing (**Fig. 1A**, **Extended Data Fig. 1E-F**). A gene score (mean $\log_2$ fold-
89 change) was calculated for each gene included in the library by assessing the change in
90 abundance of sgRNAs during the culture period (**Fig. 1B**). As expected, sgRNAs targeting known
91 *MLL1*-r leukemia dependencies, such as *Dot1l*[29-32], *Brd4* (ref. 33), and *Myb*[34] were strongly
92 depleted in both treatments while control sgRNAs remained largely neutral, thereby validating our
93 screening platform (**Supplementary Table 2**).

94 Among the sgRNAs that were enriched or depleted in the absence and presence of drug, sgRNAs
95 targeting the histone H3 lysine 27 (H3K27) demethylase *Utx* (*Kdm6a*) and the histone H3 lysine
96 4 (H3K4) mono-methyltransferases *Mll3* (*Kmt2c*) and *Mll4* (*Kmt2d*) were the most significantly
97 enriched in the Menin-MLL inhibitor context (**Fig. 1B**, red circles). This result was unexpected,
98 since the canonical activity of the MLL1/2-Menin complex (disrupted by MI-503) is to catalyze the
99 di/tri-methylation of H3K4 (H3K4me2/3) at *promoters*, resulting in loading of the transcriptional
100 machinery at such sites[13,35,36], while the MLL3/4-UTX complex regulates *enhancer* states by
101 serving as the major H3K4 mono-methyltransferase (H3K4me1) (refs. 37-41).

102 To assess whether these results were idiosyncratic of the cell line, library, or inhibitor used, we
103 performed a genome-wide CRISPR screen in an independently derived MLL-AF9 mouse cell line
104 using VTP-50469, a more potent, selective, and orally bioavailable Menin-MLL inhibitor that led
105 to the development of SNDX-5613, which is currently under investigation in a phase 1/2 clinical
106 trial for treatment of relapsed/refractory acute leukemia (NCT04065399) (refs. 25,27,28).
107 Remarkably, sgRNAs targeting *Utx* (*Kdm6a*), *Mll3* (*Kmt2c*), and *Mll4* (*Kmt2d*) were also among

108 the most significantly enriched candidate genes identified in this genome-wide screen (**Fig. 1C,**
109 **Extended Data Fig. 2A-C, Supplementary Table 2**). Interestingly, shared subunits between the
110 two types of MLL complexes scored similarly in both vehicle and Menin-MLL inhibitor conditions
111 (**Fig. 1B-D, Extended Data Fig. 1G, Extended Data Fig. 2D**). This suggests that core subunits
112 of the MLL3/4-UTX complex[42] modulate therapeutic responses to Menin-MLL inhibition and have
113 context-specific tumor suppressive functions[43,44], a result that is consistent with their
114 haploinsufficient tumor suppressor activity in some cancers[45].

115 *Utx* or *Mll3* loss-of-function did not affect leukemia cell proliferation *in vitro*, while *Mll4* inactivation
116 decreased cell growth, consistent with previous work[43] (**Extended Data Fig. 3A-D**). However, in
117 agreement with our screening results, *Utx* disruption using three distinct sgRNAs significantly
118 increased the viability of MI-503-treated leukemia cells, confirming that inactivation of *Utx* confers
119 resistance to Menin-MLL inhibition (**Fig. 1E, Extended Data Fig. 3E**). In addition, *Mll3*- and *Mll4*-
120 deficient cells treated with MI-503 exhibited a proliferative advantage over wild-type cells only in
121 the treatment context (**Extended Data Fig. 3F-G**). These orthogonal results establish the MLL3/4-
122 UTX complex as a central modulator of therapy response to Menin-MLL inhibition.

123 UTX was among the most significantly enriched chromatin factors in our screen (**Fig. 1B-C,**
124 **Extended Data Fig. 1G, Extended Data Fig. 2D**). As this factor is shared by both MLL3 and
125 MLL4 complexes[41,46,47], we focused on UTX disruption to functionally probe the molecular
126 mechanisms linked to resistance to Menin-MLL inhibition. We first tested whether genetic *Utx*
127 inactivation could rescue the effects of Menin-specific ablation in MLL-AF9 leukemia cells. While
128 CRISPR-mediated deletion of *Men1* led to robust inhibition of proliferation (**Extended Data Fig.**
129 **4A**), co-deletion of *Utx* suppressed this phenotype, such that *Men1*-deficient MLL-AF9 cells were
130 able to robustly proliferate (**Fig. 1F, Extended Data Fig. 4B-C**). Importantly, deletion of *Utx*, *Mll3*,
131 or *Mll4* in isolation did not confer any significant fitness advantage to cells, further validating our
132 findings obtained with pharmacologic inhibition of Menin-MLL (**Extended Data Fig. 3**).

133 To determine if the genetic interaction between Menin and UTX depends on the MLL-fusion
134 protein (MLL-FP), we ablated the human *MLL1-AF9* transgene expressed in MLL-AF9 leukemia
135 cells using sgRNAs selectively targeting exons 3 or 5 of the human *MLL1* gene (preceding the
136 breakpoint cluster region (exons 9-11) in *MLL1*-translocations)[48,49] (**Extended Data Fig. 5A**).
137 Cells deficient for *MLL-AF9* and *Utx* exhibited fitness defects similar to cells lacking *MLL-AF9*,
138 validating the exquisite dependency of leukemia cells to the pleiotropic gene regulatory activity of
139 this oncogenic fusion[20] (**Extended Data Fig. 5B-C**). However, MLL-AF9 leukemia cells deficient
140 for *Men1* and *Utx*, or those deficient for *Utx* and treated with Menin-MLL inhibitor, were able to
141 proliferate without reactivation of canonical fusion targets (**Extended Data Fig. 6**), demonstrating
142 that this genetic interaction is not entirely dependent on the oncogenic activity of the MLL-FP.
143 Similarly, co-deletion of *UTX* and *MEN1* in a Menin-dependent non *MLL1*-r human leukemia cell
144 line driven by *DNMT3A* and *NPM1* mutations[50,51] also rescued the fitness deficiency associated
145 with loss of *MEN1* alone (**Extended Data Fig. 5D-E**), suggesting that the functional Menin-UTX
146 interaction observed in our models is conserved in human cells. Similar results were obtained in
147 non *MLL1*-r AML1-ETO9a mouse leukemia cells treated with MI-503 (**Extended Data Fig. 5F-G**).
148 These data suggest that the phenotype of Menin-MLL inhibition is evolutionarily conserved, acts
149 in part through a pathway that involves crosstalk between Menin and UTX, and is downstream or
150 independent of MLL-FPs.

151 Menin is needed for expression of canonical MLL-FP target genes, such as *Meis1*, whose function
152 is required for leukemia maintenance[25,35,36,52,53], and *Meis1* over-expression was recently shown
153 to partially rescue the leukemic stem cell transcriptional program suppressed by Menin-MLL
154 inhibition[27]. We confirmed that treatment of mouse MLL-AF9 leukemia cells with MI-503 led to
155 robust downregulation of *Meis1* (**Extended Data Fig. 6A**). However, to our surprise, cells
156 genetically deficient for both *Men1* and *Utx* showed a similar reduction in *Meis1* levels (**Extended**
157 **Data Fig. 6B**), yet were able to proliferate *in vitro* (**Fig. 1F, Extended Data Fig. 4B**). We further

158 confirmed these findings in an additional Menin-dependent mouse MLL-AF9 cell line (**Extended**
159 **Data Fig. 6C-D**) and a human MLL-AF4-driven leukemia line[54] (**Extended Data Fig. 6E-F**). These
160 experiments reveal an epistatic relationship between Menin and UTX in Menin-dependent
161 mammalian cells and suggest that factors beyond *Meis1* can sustain the proliferative potential of
162 *MLL1*-r and non *MLL1*-r leukemia cells.

163 **MLL1-Menin complex and NF-Y restrict chromatin occupancy of MLL3/4-UTX at promoter**
164 **regions**

165 Menin is generally associated with chromatin-modifying and transcriptional complexes at
166 promoter regions[6,55], while UTX canonically resides in complexes that regulate enhancers[41]. To
167 determine the genomic distribution of Menin and UTX in the absence or presence of the Menin-
168 MLL inhibitor, we performed chromatin immunoprecipitation followed by sequencing (ChIP-Seq).
169 Menin showed strong enrichment at promoter regions (here defined as transcription start sites
170 (TSSs) ± 2kb), which was substantially decreased when its canonical interactions with MLL1/2
171 were disrupted by MI-503 (**Fig. 2A**). Genome-wide enrichment of Menin was also decreased, as
172 evidenced by a >10-fold reduction in the number of ChIP peaks post MI-503 treatment (**Extended**
173 **Data Fig. 7A**). Conversely, while only a very minor fraction of UTX appeared to be enriched on
174 chromatin at basal conditions, the genome-wide enrichment of UTX dramatically increased upon
175 treatment with MI-503, as evidenced by a ~70-fold increase in the number of peaks (**Extended**
176 **Data Fig. 7A**). UTX canonically resides in complexes that regulate enhancers[37,41] yet, contrary to
177 expectation, more than 70% of UTX binding peaks in MI-503 treated cells were localized at
178 promoters and proximal regions (**Fig. 2B, Extended Data Fig. 7A**)[56]. Importantly, the enhanced
179 enrichment of UTX on chromatin was not merely the result of increased expression and/or protein
180 stability (**Fig. 2C-D**). These data show that disruption of the Menin-MLL1/2 interaction leads to
181 dynamic and robust recruitment of UTX to promoter regions (**Fig. 2B**), suggesting a previously

182 unrecognized role for the canonical MLL3/4-UTX complex in promoter regulation and gene
183 transcription[37].

184 Not only did Menin depletion lead to recruitment of UTX to promoter regions, the loci that
185 accumulated UTX significantly overlapped with those where Menin was lost (**Fig. 2E-F**, **Extended**
186 **Data Fig. 7B**). Specifically, correlation analysis suggested that reduction of Menin binding by MI-
187 503 coincided with increased UTX chromatin occupancy at the same genomic loci (*Pearson*
188 *coefficient (r)* = -0.49) (**Fig. 2G**). This molecular switch was specific to Menin-dependent cells, as
189 MI-503 treatment of Menin-independent mouse fibroblasts did not lead to UTX redistribution or
190 increased binding to promoters (**Extended Data Fig. 8A-E**). Therefore, Menin excludes UTX from
191 binding to promoters in Menin-dependent cell types, and this antagonism can be reversed by MI-
192 503-mediated displacement of MLL1-Menin complexes from chromatin.

193 Inhibition of Menin-MLL1 leads to displacement of this complex from gene promoters, allowing
194 UTX to bind and potentially regulate target gene expression (**Fig. 2**). To further understand the
195 molecular switch between Menin and UTX at promoters, we examined the chromatin-binding
196 profiles of their cognate H3K4 methyltransferases and their enzymatic histone modifications
197 (MLL1 and H3K4me3 for Menin, and MLL3/4 and H3K4me1 for UTX) (**Extended Data Fig. 9A-**
198 **B**). Disruption of the Menin-MLL1 interaction led to a substantial decrease in MLL1 chromatin
199 binding and a concomitant decrease of its enzymatic product, H3K4me3, (**Extended Data Fig.**
200 **9C-E**). In contrast, Menin-MLL1 inhibition led to increased binding of the MLL3/4 enzymes at
201 promoter regions co-occupied by UTX and a concomitant increase in H3K4me1 signal at these
202 same loci (**Extended Data Fig. 9C, 9F-G**). These data suggest that disruption of the MLL1-Menin
203 complex induces targeting of the enzymatic subunits of the MLL3/4-UTX complex to non-
204 canonical sites that are normally bound by the MLL1-Menin complex and are distinct from those
205 bound by the MLL-FP (**Extended Data Fig. 10A-C**). These results provide additional evidence

206 for the existence of a molecular switch between the MLL complexes that is induced by Menin-
207 MLL inhibition.

208 The above results are provocative, as promoter-associated H3K4me1 facilitates transcriptional
209 repression in other cellular settings[57], suggesting that deposition of H3K4me1 at gene promoters
210 could depend on context[58]. Nevertheless, our finding that *Utx*^{KO}, *Mll3*^{KO}, and *Mll4*^{KO} cells are
211 resistant to Menin-MLL inhibition (**Fig. 1**, **Extended Data Fig. 3E-G**) – combined with the
212 colocalization of UTX, MLL3, MLL4, and H3K4me1 at the promoters of target genes – led us to
213 hypothesize that the MLL3/4-UTX complex co-regulates gene expression in the context of Menin-
214 MLL inhibition in leukemia. To test this hypothesis, we leveraged H3 lysine-4-to-methionine (K4M)
215 'oncohistone' mutants as orthogonal molecular tools to destabilize the MLL3/4-UTX complex[59]
216 (**Extended Data Fig. 11A**). Supporting our model, expression of H3.1K4M in MLL-AF9 leukemia
217 cells led to a substantial proliferative advantage only in the context of Menin-MLL inhibition
218 (**Extended Data Fig. 11B-D**), demonstrating that destabilization of the MLL3/4-UTX complex
219 (**Extended Data Fig. 13E**) can phenocopy the intrinsic resistance of *Utx*-, *Mll3*-, and *Mll4*-deficient
220 cells to Menin-MLL1 inhibition (**Fig. 1E-F, Extended Data Fig. 3E-G**). These results further
221 support a model whereby the MLL3/4-UTX complex serves as a central modulator of therapy
222 response to Menin-MLL inhibition.

223 Given that Menin lacks a defined DNA binding domain[60], we hypothesized that a sequence-
224 specific DNA binding factor regulates the switch between MLL1-Menin and MLL3/4-UTX
225 occupancy at specific promoters. To test this hypothesis, we performed motif analysis on genomic
226 regions bound by Menin and UTX, uncovering NF-Y sequence motifs[61] as the most significantly
227 enriched (P=1e^{-130}) (**Extended Data Fig. 12A**). These motifs were specific to leukemia cells, as
228 motif enrichment analysis identified a different subset of sequences in mouse fibroblasts
229 (**Extended Data Fig. 12B-C**). ChIP-Seq of NF-YA (the DNA binding and transactivation subunit
230 of the NF-Y complex[61]) confirmed these observations, showing that NF-YA co-occupies sites

231 bound by Menin and UTX (**Extended Data Fig. 12D-E**). Consistent with our hypothesis, sites
232 bound by UTX in the context of Menin-MLL inhibition also had lower NF-YA occupancy (**Extended**
233 **Data Fig. 12D-E**), which was not due to decreased protein levels (**Extended Data Fig. 12F**).
234 Moreover, CRISPR-mediated disruption of *Nfya* in MLL-AF9 leukemia cells significantly
235 decreased the viability of MI-503-treated leukemia cells relative to control cells (**Extended Data**
236 **Fig. 13A-C**). This observation led us to hypothesize that NF-YA depletion could lead to a
237 concomitant decrease of Menin and increase of UTX occupancy at target genomic regions.
238 Supporting this model, treatment of *Nfya*^{KO} cells with MI-503 led to a substantial increase in UTX
239 occupancy at genomic regions normally bound by Menin and NF-Y at steady-state (**Extended**
240 **Data Fig. 10D-F**). These results are also consistent with co-essentiality analyses in human cells[59]
241 showing that a subset of *MEN1*-dependent cells are codependent on members of the NF-Y
242 complex for survival (**Extended Data Fig. 13G-J)**. Collectively, these results implicate NF-Y in
243 restricting the occupancy of UTX at promoter regions and further suggest that Menin binding to
244 these sites is mediated by the sequence-specific DNA binding activity of the NF-Y transcription
245 factor.

246 **Transcriptional co-regulation of tumor suppressive pathways by Menin and UTX**

247 The above results support a model whereby a molecular switch between the MLL1-Menin and
248 MLL3/4-UTX complexes at gene promoters dictates responses to Menin-MLL inhibition. We
249 hypothesized that this switch acts through transcriptional regulation of genes involved in pathways
250 that control cellular proliferation and survival. To test this, we performed transcriptional profiling
251 of MLL-AF9 leukemia cells treated with MI-503 and identified pathways that are reciprocally
252 regulated by Menin and UTX (**Extended Data Fig. 14A-B**). Although the catalytic activity of the
253 MLL1/2-Menin histone methyltransferase complex is canonically associated with actively
254 transcribed developmental genes[2,13], disruption of the complex by MI-503 resulted in both up- and
255 down-regulation of gene expression, with slight skewing towards gene activation (**Fig. 4A**).

256 Remarkably, the majority of significantly upregulated genes were reciprocally bound by Menin
257 and UTX, suggesting that their expression is tightly co-regulated by these chromatin factors and
258 gene repression mechanisms might be operative in this context (**Fig. 4B**). Consistent with this
259 observation, ChIP-Seq against acetylated H4K16 and H3K27 (histone marks associated with
260 gene activation;[62]) showed that levels of these marks increased at sites where the MLL3/4-UTX
261 complex is recruited to upon Menin-MLL inhibition (**Extended Data Fig. 15A-C**). Importantly, we
262 also observed increased levels of MOF, a histone H4K16 acetyltransferase[63-65], at the same loci
263 bound by UTX in the context of Menin-MLL inhibition (**Extended Data Fig. 15B**). These results
264 support a model whereby Menin-MLL inhibition leads to dynamic changes in gene expression due
265 to loss of MLL-dependent repressive activity and a concomitant increase in histone marks
266 associated with gene activation (including H4K16ac and H3K27ac)[66,67].

267 To determine if UTX was necessary for gene activation, we generated *Utx*-deficient (*Utx*^{KO}) MLL-
268 AF9 leukemia cells (**Extended Data Fig. 16A**), treated these with MI-503, and profiled by RNA-
269 Seq (**Extended Data Fig. 16B**). Genes bound by UTX and induced by MI-503 failed to get
270 activated in *Utx*^{KO} cells, suggesting that UTX function is necessary for their transcriptional
271 activation when Menin is displaced from chromatin (we refer to these genes as 'Menin-UTX
272 targets') (**Fig. 4C**, **Supplementary Table 4**). Importantly, *Utx*^{KO} cells treated with MI-503 exhibited
273 downregulation of canonical MLL-AF9 targets and induction of myeloid differentiation programs
274 (**Extended Data Fig. 17A-C**), as observed by others in *Utx* proficient cells[22,25,27]. As shown earlier,
275 *Utx*^{KO} leukemia cells treated with MI-503 were able to proliferate without re-expression of *Meis1*,
276 a critical Menin-MLL-FP target[25,27,52,53] (**Fig. 1E**, **Extended Data Fig. 6B, Extended Data Fig.**
277 **17D**). These data suggest a new paradigm whereby the effects of Menin-MLL inhibition on MLL-
278 FP target genes are independent of its effects on Menin-UTX transcriptional targets, and that
279 induction of a tumor suppressive gene expression program alongside repression of canonical
280 MLL-FP targets is required for the anti-leukemic activity of Menin-MLL1 inhibitors.

281 To gain insight into pathways directly regulated by Menin and UTX, we performed gene ontology
282 (GO) analysis[68,69] of Menin-UTX targets (**Supplementary Table 4**) and found significant evidence
283 for their association with transcriptional programs related to proliferation, differentiation, and
284 survival (**Extended Data Fig. 14B**). To further evaluate the relevance of these GO terms, we
285 performed Gene Set Enrichment Analysis (GSEA)[70] on transcriptional data from *Utx*^{WT} and *Utx*^{KO}
286 cells treated with MI-503 and observed a significant correlation between the presence of UTX and
287 the expression of senescence-associated genes following MI-503 treatment[71] (**Fig. 4D**, **Extended**
288 **Data Fig. 18A-F**, **Supplementary Table 4**). This correlation was independently confirmed using
289 a curated list of genes involved in cell cycle arrest and therapy-induced senescence[72] (**Fig. 4E**)
290 and is consistent with the fact that Menin-MLL inhibition induces a combination of cell cycle arrest,
291 apoptosis, and differentiation (**Extended Data Fig. 1E-G**)[22], as well as our observation that the
292 senescence-associated H4K16ac mark increases with MI-503 treatment[73] (**Extended Data Fig.**
293 **15A-B**). We also observed increased occupancy of RNA Polymerase II at the promoters of
294 senescence-associated genes that are up-regulated by MI-503 treatment, lending further support
295 to these findings (**Extended Data Fig. 18G**). These observations suggest that the interplay
296 between Menin and UTX in the context of Menin-MLL inhibition regulates the expression of genes
297 involved in cellular senescence.

298 The cellular senescence program is highly complex and is characterized in part by induction of
299 permanent cell cycle arrest and a senescence-associated secretory phenotype (SASP)[74].
300 Consistent with a direct role for the Menin-UTX switch in regulating cellular senescence, secretion
301 of prototypical SASP cytokines like IL-6, IFNβ-1, IL-3, and IL-15 was induced upon Menin-MLL
302 inhibition in a *Utx*-dependent manner (**Fig. 4F-G, Extended Data Fig. 19**). These results
303 demonstrate that Menin-MLL inhibition engages a potent tumor suppressive network that includes
304 therapy-induced cellular senescence and is transcriptionally regulated in large part by the MLL3/4-
305 UTX complex.

306 **Combinatorial targeting of Menin and CDK4/6 overcomes resistance associated with loss**
307 **of MLL3/4-UTX function**

308 Given that senescence can be regulated at both transcriptional and post-transcriptional levels,
309 and chromatin regulation has been functionally implicated in modulating this program[73,75,76], we
310 hypothesized that the Menin-UTX molecular switch directly regulates the expression of cell cycle
311 arrest- and senescence-associated genes by direct binding to their promoters[56,77]. Consistent with
312 our hypothesis, we found that Menin is bound to the promoters of the cyclin-dependent kinase
313 (CDK) inhibitors *Cdkn2c/Ink4c* and *Cdkn2d/Ink4d* at basal conditions[78], and that binding is
314 abrogated upon Menin-MLL inhibition, leading to induction of their expression (**Fig. 4H**, **Extended**
315 **Data Fig. 20A-B, Extended Data Fig. 21**). Conversely, we found that UTX binds to these
316 promoters only in the context of Menin-MLL inhibition, leading to UTX-dependent upregulation of
317 both CDK inhibitors (**Fig. 4H**, **Extended Data Fig. 20A-B**). These data show that the Menin-UTX
318 molecular switch regulates the expression of these CDK inhibitors by direct chromatin regulation.

319 Since the proteins encoded by these two genes are natural inhibitors of the CDK4 and CDK6
320 kinases[78], we hypothesized that pharmacological inhibition of CDK4/6 would bypass the intrinsic
321 resistance of *Utx*^{KO} cells to MI-503 while retaining the therapeutic effects of Menin-MLL inhibition
322 on MLL-FP targets (**Fig. 4I**). We therefore combined MI-503 with the FDA-approved CDK4/6
323 inhibitor Palbociclib[79], which has been shown to trigger durable cell cycle arrest and
324 senescence[72,80,81]. *Utx*^{KO} cells were more resistant to either MI-503 or Palbociclib alone when
325 compared to *Utx*^{WT} cells, likely due to higher basal levels of *Cdk6* transcripts (**Fig. 4J, Extended**
326 **Data Fig. 20C-D**) [77,82]. However, combined inhibition of Menin-MLL and CDK4/6 resulted in a
327 synergistic effect (CD=0.4) (ref. 83) on inhibiting cell proliferation to similar levels achieved by MI-
328 503 treatment of *Utx*^{WT} cells (**Fig. 4J**). These proof-of-concept data demonstrate that targeting
329 pathways regulated by Menin and UTX can produce combinatorial therapeutic effects and further
330 suggest that the anti-leukemic effects of MI-503[22] are primarily through reactivation of tumor

331 suppressor pathways and not solely through dampening transcription of MLL-FP targets like
332 *Meis1* (refs. 22,25,27,52). Thus, the combination of Palbociclib with Menin-MLL inhibitors may
333 represent a novel and more effective therapeutic strategy for Menin-dependent cancers[23,24,26,84,85].

334 **Catalytic activity of UTX is not required to elicit UTX-dependent cellular and transcriptional**
335 **functions**

336 The UTX protein contains several functional domains, including a JmjC demethylase domain that
337 catalyzes the removal of the H3K27me3 histone mark[86-89]. To determine the regions of UTX that
338 are necessary for UTX-dependent cellular and transcriptional phenotypes observed upon Menin-
339 MLL inhibition, we performed a series of structure-function-rescue experiments (**Fig. 4A**). We
340 generated lentiviral constructs encoding dual N-terminal HA- and C-terminal Flag-tagged
341 truncations of UTX spanning the full-length of the mouse protein and used them to stably
342 transduce and phenotype *Utx*-null leukemia cells treated with MI-503 (**Fig. 4A, Extended Data**
343 **Fig. 22A-C)**. We found that full-length UTX or a UTX truncation harboring the first 500 amino
344 acids (1-500 aa) and lacking the JmjC demethylase domain[86-89], were sufficient to re-sensitize
345 cells to MI-503 treatment while truncations proximal to the C-terminus were unable to do so (**Fig.**
346 **4B**). Consistent with these cellular phenotypes, RNA-Seq of FACS-sorted *Utx* cDNA expressing
347 cells treated with MI-503 showed that full-length UTX and the 1-500 aa UTX truncation were
348 sufficient to rescue UTX-dependent transcriptional phenotypes associated with Menin-MLL
349 inhibition (**Fig. 4C**), including induction of Menin-UTX target genes like *Cdkn2c* (**Fig. 4D,**
350 **Extended Data Fig. 23**). These results demonstrate that an N-terminal truncation of UTX lacking
351 the JmjC demethylase domain[86-89] and a recently reported intrinsically disordered region[90] is both
352 necessary and sufficient to drive tumor suppressive responses in this context.

353 To further confirm that UTX employs non-catalytic mechanisms to regulate gene expression in
354 the context of Menin-MLL inhibition, we performed ChIP-Seq for H3K27me3, a modification

355 catalyzed by PRC2 (ref. 91) and removed by UTX[86-89]. We found that the genomic redistribution
356 of UTX induced upon treatment with MI-503 (**Fig. 2B, 2E**) did not affect global levels of H3K27me3
357 (**Extended Data Fig. 24A-B**), which led us to hypothesize that this histone mark does not play a
358 critical role in these phenotypes. To functionally test this hypothesis, we generated *Ezh2*^{KO} and
359 *Ezh2*^{KO};*Utx*^{KO} MLL-AF9 leukemia cells and confirmed by immunoblotting that these have no
360 detectable levels of H3K27me3 (**Extended Data Fig. 24C**). Remarkably, while *Ezh2*-null
361 leukemia cells remained exquisitely sensitive to MI-503, double *Ezh2*^{KO};*Utx*^{KO} cells were fully
362 resistant to Menin-MLL inhibition (**Extended Data Fig. 24D**). These results demonstrate that the
363 catalytic function of UTX is dispensable for UTX-dependent transcriptional phenotypes and
364 therapeutic responses to Menin-MLL inhibitors.

365 **Response to Menin-MLL inhibitors in primary human AML is accompanied by**
366 **transcriptional induction of MLL3/4-UTX-dependent tumor suppressive programs**

367 Small molecule inhibitors of the Menin-MLL interaction have shown promise in preclinical models
368 of acute lymphoid and myeloid leukemia[25,27,92] and are currently in Phase I/II clinical trials for
369 treatment of patients with acute leukemia (SNDX-5613 (NCT04067336), KO-539
370 (NCT04065399), and JNJ-75276617 (NCT04811560)). Notably, SNDX-5613 was recently
371 granted fast track designation by the FDA for treatment of relapsed/refractory acute leukemias.
372 We hypothesized that the Menin-UTX molecular switch described above would be operative in
373 leukemia patients treated with these Menin-MLL inhibitors. Consistent with our hypothesis,
374 longitudinal RNA-Seq analysis of AML cells derived from two patients with *NPM1c*-mutated
375 (Patient 1) and *MLL*-rearranged (Patient 2) leukemia treated with SNDX-5613 as part of the
376 AUGMENT-101 clinical trial (NCT04065399) showed concomitant suppression of canonical MLL-
377 FP target genes (e.g., *MEIS1*) and induction of CDK inhibitors (e.g., *CDKN2C*) (**Fig. 5A-E,**
378 **Extended Data Fig. 25**).

379 As an orthogonal approach, we analyzed a panel of genetically-annotated patient-derived
380 xenografts (PDXs) of *MLL*-rearranged acute leukemia for response and resistance to VTP-50469
381 (a close analog of SNDX-5613) *in vivo*[25] (**Fig. 5F, Extended Data Fig. 26A**). Mice transplanted
382 with an *MLL3* wild type PDX showed a potent response to VTP-50469 and significant induction
383 of Menin-UTX targets (**Fig. 5G-H, Extended Data Fig. 27A-B**), reflecting the activation of the
384 UTX-dependent tumor suppressive gene expression program defined in mouse models of AML
385 (**Fig. 3**). Conversely, an *MLL3* mutant PDX exhibited primary resistance to VTP-50469 and failed
386 to induce this gene expression program (**Fig. 5I-J, Extended Data Fig. 27A and 27C**), thereby
387 functionally linking the induction of Menin-UTX-targets to preclinical drug response. Targeted
388 DNA sequencing confirmed that the resistant PDX harbored a missense mutation in the *MLL3*
389 gene (**Extended Data Fig. 26B**). Thus, the gene expression programs regulated by the epistatic
390 relationship between the MLL1-Menin and MLL3/4-UTX complexes are at play in patients and
391 PDXs treated with orally bioavailable Menin-MLL inhibitors that are currently under clinical
392 investigation. Somatic mutations in members of the MLL3/4-UTX complex that impact catalytic
393 activity or protein complex composition may impact the induction of tumor suppressive gene
394 expression programs induced by Menin-MLL-inhibitors, thereby blunting clinical responses.

395 To test whether CDK4/6 inhibition can bypass the blunted induction of endogenous CDK inhibitors
396 in Menin inhibitor-resistant contexts, we treated mice harboring the *MLL3*-mutant AML PDX with
397 VTP-50469 (0.1% rodent diet) and Palbociclib (35mg/kg) (**Fig. 5I**). As predicted by our findings
398 (**Fig. 3I-J**), single treatment with Menin- or CDK4/6-inhibitors only led to a minor decrease in
399 leukemia burden in the bone marrow of recipient mice after 10 days of treatment (**Fig. 5K-L**).
400 However, combination treatment with VTP-50469 and Palbociclib induced significant regression
401 in the abundance of human leukemia cells (**Fig. 5K-L**). To determine whether treatment
402 responses were associated with transcriptional induction of UTX-dependent tumor suppressive
403 programs, we performed RNA-Seq from FACS-sorted human leukemia cells isolated from these

404 animals. Consistent with our findings, we observed significant induction of cell cycle arrest and
405 senescence-associated gene expression signatures in mice treated with both VTP-50469 and
406 Palbociclib (**Fig. 5M, Extended Data Fig. 27D**). Altogether, this data provides pre-clinical
407 evidence for the feasibility and efficacy of combined Menin- and CDK4/6-inhibition to overcome
408 the blunted induction of senescence-associated programs in patient-derived leukemias resistant
409 to Menin-inhibitor monotherapy.

410 Discussion

411 The Menin chromatin adaptor protein exhibits profound context-specific functions in different
412 tissues, acting as a tumor suppressor gene in neuroendocrine[14,15], lung[17,93], skin[16], and CNS
413 malignancies[18], and as an oncogenic cofactor in hepatocellular[19] and hematologic cancers[4,20].
414 Given that Menin can interact with similar cofactors in disparate settings, the basis for these
415 apparently paradoxical findings has remained largely unclear. For example, Menin functionally
416 cooperates with MLL proteins to activate transcription of the *Cdkn1b/p27^{Kip1}* and *Cdkn2d/Ink4d*
417 CDK inhibitors as a tumor suppressive mechanism in neuroendocrine tumors and lung
418 cancer[3,17,94,95], yet the same protein-protein interaction is critical for leukemia maintenance[4,10,20].
419 These contrasting observations suggest that Menin employs unique molecular mechanisms to
420 regulate chromatin and gene expression depending on the biological context.

421 Our study sheds light on these paradoxical observations by providing the first evidence for a
422 functional interaction between the mammalian histone methyltransferase complexes MLL1-Menin
423 and MLL3/4-UTX and challenges the paradigm that these complexes are restricted to certain
424 genomic compartments (**Fig. 6**). We show that the Menin-MLL and NF-Y complexes coordinately
425 co-repress the expression of a tumor suppressive network that involves the *Cdkn2c/Ink4c* and
426 *Cdkn2d/Ink4d* tumor suppressor genes in leukemia by direct binding to gene promoters.
427 Disruption of Menin-MLL or NF-Y complexes using genetic or pharmacological approaches

428 triggers a molecular switch that leads to recruitment of the MLL3/4-UTX complex to the promoters
429 of tumor suppressive genes, including the *Cdkn2c/Ink4c and Cdkn2d/Ink4d* CDK inhibitors[78]. This
430 molecular switch leads to UTX-dependent activation of gene expression and is associated with a
431 concomitant increase in the levels of the gene activation-associated histone marks H4K16ac and
432 H3K27ac, leading to robust induction of tumor suppressive programs like cellular senescence[73,75].
433 Thus, the molecular choreography between the MLL1-Menin and MLL3/4-UTX complexes
434 dictates cellular survival in leukemia.

435 Our study also shows that the first 500 amino acids of UTX (lacking the demethylase domain) are
436 sufficient to induce full length UTX-dependent cellular and transcriptional phenotypes. This finding
437 is particularly interesting given a recent study suggesting that UTX requires a much bigger protein
438 fragment to drive tumor suppressive activity and transcriptional regulation via phase separation
439 mechanisms[90]. Instead, our study decisively demonstrates that the first 500 amino acids of UTX
440 (lacking the core intrinsically disordered region defined by Shi *et al.*[90]) are necessary and sufficient
441 to drive tumor suppressive responses in the context of Menin-MLL inhibition. These results
442 establish a new paradigm by which UTX employs non-catalytic mechanisms to regulate gene
443 expression and cellular phenotypes that impact response to epigenetic therapies.

444 Based on our observation that UTX directly binds to and activates the expression of *Cdkn2c/Ink4c*
445 *and Cdkn2d/Ink4d* (which are natural inhibitors of the CDK4/6 kinases)[78], we combined Menin-
446 MLL inhibition with the FDA-approved CDK4/6 kinase inhibitor Palbociclib[79] and showed that this
447 combinatorial approach leads to a strong synergistic effect on inhibiting leukemia cell proliferation
448 *in vitro* and *in vivo*. As Palbociclib and other CDK4/6 inhibitors are already FDA-approved[81], our
449 proof-of-concept and pre-clinical studies suggest that this combinatorial approach could be a
450 viable therapeutic option to both boost the effectiveness of Menin inhibitors as monotherapies
451 while potentially overcoming the intrinsic resistance to Menin-MLL inhibition conferred by loss-of-
452 function of the MLL3/4-UTX complex.

453 Our study demonstrates — in murine and human systems — that the functional interplay between
454 MLL1-Menin and MLL3/4-UTX is critical for Menin-inhibitor responses due to induction of Menin-
455 UTX target genes. Notably, we were able to show that the induction of this gene expression
456 program is at play upon oral delivery of VTP-50469 to leukemia PDX models and SDNX5613 to
457 human AML subjects in the context of the AUGMENT-101 clinical trial (NCT04065399).
458 Importantly, the Menin-UTX signature was absent in a non-responsive PDX harboring a missense
459 mutation in *MLL3*, but could be re-engaged by additional treatment with an FDA-approved
460 CDK4/6 inhibitor, providing the first pre-clinical rationale to consider such combination therapy
461 approaches in clinical settings to induce cell cycle arrest and senescence programs in leukemia
462 cells when Menin-MLL inhibitor monotherapy fails to do so.

463 **FIGURE LEGENDS**

464 **Figure 1. CRISPR screens uncover functional interplay between the mammalian**
465 **MLL1/2 and MLL3/4 chromatin modifying complexes. (A)** CRISPR-Cas9-based
466 screening strategy to identify chromatin regulators that modulate response to Menin
467 inhibition. CPD, cell population doublings; sgRNA, single guide RNA; TF, final timepoint;
468 T0, initial timepoint. **(B)** Top 20 most significantly enriching (red) and depleting (blue)
469 genes in the MI-503-treated CRISPR screen. Gene scores are shown as the mean $\log_2$
470 fold-change in abundance of the 6 sgRNAs targeting each gene in each condition. **(C)**
471 Genome-wide screening data showing gene-level ranking based on differential
472 enrichment of sgRNAs under Menin-MLL inhibitor treatment (VTP-50469) relative to
473 vehicle (DMSO). Differential (Δ) beta-score between VTP-50469 and DMSO conditions
474 was calculated using MaGeCK. A positive Δ beta-score denotes enrichment of specific
475 gene-targeting sgRNAs. A negative Δ beta-score denotes depletion of specific gene-

476 targeting sgRNAs. Red circles denote MLL3/4-UTX complex subunits. Yellow circles
477 denote PRC1.1 complex subunits. **(D)** Schematic representation of the top scoring
478 chromatin regulators in the chromatin-focused MI-503 screen and their corresponding
479 protein complexes. Red denotes enriching subunits. Blue denotes depleting subunits.
480 Color scale represents the $\log_2$ fold-change in MI-503. **(E)** Cell viability assay from cells
481 treated with DMSO (vehicle, black) or MI-503 (red) after 96 hours (mean±SEM, n=3
482 infection replicates, *P*-value calculated by Student's t-test). sgCtrl, control sgRNA
483 targeting a non-genic region on chromosome 8. **(F)** Differential fitness is shown as the
484 relative fitness of double positive cells (sgMen1-RFP + sgUtx-BFP or sgMen1-RFP +
485 sgCtrl-BFP) to single positive cells (sgMen1-RFP) 16 days post-infection measured by
486 flow cytometry (mean±SEM, n=3 infection replicates, *P*-value calculated by Student's t-
487 test).

488 **Figure 2. MLL1-Menin complex and NF-Y restrict chromatin occupancy of MLL3/4-**
489 **UTX at promoter regions. (A)** Average chromatin occupancy of Menin at transcription
490 start sites (TSS), and 2kb upstream and downstream of the TSS are also included.
491 Signals corresponding to cells treated with MI-503 (solid) compared to cells treated with
492 DMSO (dotted) after 96 hours are shown. RPM, reads per million. **(B)** Average chromatin
493 occupancy of UTX at transcription start sites (TSS), and 2kb upstream and downstream
494 of the TSS are also included. Signals corresponding to cells treated with MI-503 (solid)
495 after 96 hours compared to cells treated with DMSO (dotted) after 96 hours are shown.
496 RPM, reads per million. **(C)** Relative *Utx* mRNA levels determined by qPCR in MLL-AF9
497 cells treated with MI-503 (red) versus DMSO (black) after 96 hours (mean ± SEM, n=3
498 replicates, *P*-value calculated by Student's t-test). **(D)** Immunoblot analysis of Menin,

499 UTX, and HSP90 proteins (loading control) upon MI-503 treatment of MLL-AF9 cells after
500 96 hours. **(E)** Heatmaps displaying Menin (black) and UTX (purple) ChIP-Seq signals
501 mapping to a 4kb window around TSSs. Data is shown for DMSO and MI-503-treated
502 cells after 96 hours. Metaplot represents the average ChIP-Seq signal for Menin or UTX
503 at promoters that are UTX+ (green) or UTX- (black) post MI-503 treatment. **(F)** Genome
504 browser representation of ChIP-Seq normalized reads for Menin (black) and UTX (purple)
505 in MLL-AF9 leukemia cells treated with either vehicle or MI-503 after 96 hours. **(G)** ChIP-
506 Seq normalized reads per 10-kb bin for Menin (MI-503 vs DMSO, y-axis) and UTX (MI-
507 503 vs DMSO, x-axis). Pearson's correlation coefficient is indicated.

508 **Figure 3. Transcriptional co-regulation of tumor suppressive pathways by Menin**
509 **and UTX. (A)** Volcano plot of differentially expressed genes in mouse MLL-AF9 cells
510 treated with Menin inhibitor (MI-503) or vehicle (DMSO) after 96 hours. Significantly
511 (P<0.05) downregulated (DN) genes are shown on the left (n=921 genes). Significantly
512 (P<0.05) upregulated (UP) genes are shown on the right (n=1030). **(B)** Upset plot
513 showing significant overlap (red) between genes that undergo replacement of Menin by
514 UTX at their respective promoters and MI-503-induced genes. P-value for overlap is
515 shown. **(C)** Boxplot showing expression levels of genes that are induced by MI-503
516 treatment and are bound by UTX at their promoters in this condition and by Menin at
517 steady-state. Expression levels are shown for Utx^{WT} and Utx^{KO} leukemia cells. **(D)** Gene
518 set enrichment analysis (GSEA) showing that Menin-UTX target genes induced by MI-
519 503 are significantly enriched for genes and pathways regulating cellular senescence.
520 FDR, false discovery rate; NES, normalized enrichment score. **(E)** Heatmap denoting
521 relative gene expression levels of senescence-associated cell cycle and SASP genes

522 measured by RNA-Seq from *Utx*^{WT} and *Utx*^{KO} MLL-AF9 leukemia cells treated with Menin
523 inhibitor (MI-503) or vehicle (DMSO) after 96 hours. Senescence-associated cell cycle
524 and SASP gene list was manually curated[72]. **(F) - (G)** Secreted levels of IL-6 and IFNβ-1
525 in *Utx*^{WT} (black) and *Utx*^{KO} (red) MLL-AF9 leukemia cells treated with Menin inhibitor (MI-
526 503) or vehicle (DMSO) after four or six days. Data are quantified as pg/mL of secreted
527 cytokine per million cells and represent the mean of three biological replicates. *P*-value
528 calculated by Student's t-test. **(H)** Genome browser representation of ChIP-Seq (top) and
529 RNA-Seq (bottom) normalized reads (average RPKM) for *Cdkn2c* and *Cdkn2d* loci from
530 *Utx*^{WT} or *Utx*^{KO} MLL-AF9 leukemia cells treated with DMSO or MI-503 for 96 hours. **(I)**
531 Proposed model and rationale for combination therapies based on Menin-MLL and
532 CDK4/6 inhibitors. Our data support a model whereby **(1)** Menin restricts UTX-mediated
533 transcriptional activation of tumor suppressor genes, including *Cdkn2c* and *Cdkn2d*,
534 which are natural inhibitors of the CDK4 and CDK6 kinases, which in turn inhibit cell cycle
535 arrest and senescence. Our model predicts that CDK4/6 inhibition using Palbociclib
536 should boost the anti-cancer activity of Menin-MLL inhibitors, which we show induces a
537 MLL3/4-UTX tumor suppressive axis, by more potently inhibiting these downstream
538 kinases. On the other hand, Menin is known to be required for activation of MLL-FP
539 targets like *Meis1* and *Cdk6* itself to sustain leukemia **(2)**. Thus, our model predicts that
540 combination therapies based on Menin-MLL and CDK4/6 inhibitors should act
541 synergistically to suppress leukemia proliferation by potently engaging two parallel
542 pathways that converge on regulation of cell cycle progression. **(J)** Relative viability of
543 *Utx*^{WT} and *Utx*^{KO} MLL-AF9 leukemia cells treated with either DMSO, MI-503, Palbociclib,

544 or a combination of both inhibitors for 6 days (mean±SEM, n=3 replicates, *P*-value
545 calculated by Student's t-test).

546 **Figure 4. Catalytic activity of UTX is not required to elicit UTX-dependent cellular**
547 **and transcriptional functions. (A)** Schematic of UTX protein. Highlighted are the 8
548 tetratricopeptide repeats (TPR) (93-385aa) and the histone demethylase (JmjC) domain
549 (1095-1258aa). Three 500 amino acid long truncations are also represented. **(B)** Growth
550 competition assay in mouse *Utx*^{KO} MLL-AF9 leukemia cells expressing different RFP-
551 tagged *Utx* cDNAs and treated with MI-503 for 2 and 6 days. Graph shows the relative
552 growth of cells infected with RFP-tagged *Utx* cDNAs measured by flow cytometry
553 (mean±SEM, n=3 infection replicates, *P*-value calculated by Student's t-test). **(C)**
554 Principal component analysis (PCA) using RNA-Seq gene expression data from *Utx*^{KO}
555 MLL-AF9 leukemia cells expressing different RFP-tagged *Utx* cDNAs and treated with
556 DMSO or MI-503 for 96 hours. **(D)** Mean normalized read counts of the cyclin-dependent
557 kinase inhibitor, *Cdkn2c*, across three RNA-Seq replicate samples from different *Utx*
558 truncations in mouse MLL-AF9 leukemia and treated with DMSO or MI-503 for 96 hours.

559 **Figure 5. *In vivo* response to Menin-MLL inhibition is accompanied by induction of**
560 **MLL3/4-UTX-dependent tumor suppressive programs. (A)** Longitudinal flow
561 cytometry analysis measuring the fraction of CD45lo, cKIT+ leukemia cells in the
562 peripheral blood of an *NPM1c* mutant patient (Patient 1) during treatment cycle 1 of
563 SDNX-5613 as part of the AUGMENT-101 clinical trial (NCT04065399). **(B)** Heatmap
564 denoting temporal gene expression changes among MLL-FP targets in FACS-sorted AML
565 blasts cells from Patient 1. Plotted are all MLL-FP targets that are differentially expressed
566 at day 14 vs. day 0 of treatment cycle 1. **(C)** Temporal expression levels of genes involved

567 in cell cycle arrest and senescence (*CDKN1A*, *CDKN2B*, and *CDKN2C*) and MLL-FP
568 targets (*HOXA9*, *CDK6*, *PBX3*, and *MEIS1*) in AML cells from Patient 1 treated with
569 SDNX-5613. **(D)** Heatmap denoting temporal gene expression level changes among
570 MLL-FP targets in FACS-sorted AML blasts cells from Patient 2 treated with SDNX-5613
571 as part of the AUGMENT-101 clinical trial (NCT04065399). Plotted are all MLL-FP targets
572 that are differentially expressed at day 10 vs. day 0 of treatment cycle 1. **(E)** Temporal
573 expression levels of genes involved in cell cycle arrest and senescence (*CDKN1A*,
574 *CDKN1B*, and *CDKN3*) and MLL-FP targets (*HOXA7*, *CDK6*, *MEF2C*, and *MEIS1*) in AML
575 cells from Patient 2 treated with SDNX-5613. **(F)** Schematic of *in vivo* treatment
576 experiments using genetically-defined AML patient-derived xenografts (PDXs). NSG mice
577 were transplanted with either *MLL3*-WT or *MLL3*-Mutant AML PDXs and, upon disease
578 engraftment, were randomized into VTP-50469 (0.1% in rodent diet) or normal chow for
579 a duration of four weeks. Disease progression was monitored weekly by bleeding and
580 AML cells were sorted at 7 days post initiation of treatment using magnetic mouse cell
581 depletion from the bone marrow of animals to perform RNA-Seq. **(G)** Disease progression
582 as measured by the percentage of human CD45+ cells in the peripheral blood of mice
583 harboring *MLL3*-WT leukemia treated with vehicle (grey) or VTP-50469 (blue). **(H)**
584 Boxplot denoting gene expression levels of Menin-UTX targets in AML cells isolated from
585 mice harboring *MLL3*-WT leukemia treated with vehicle (grey) or VTP-50469 (blue). **(I)**
586 Disease progression as measured by the percentage of human CD45+ cells in the
587 peripheral blood of mice harboring *MLL3*-mutant leukemia treated with vehicle (grey) or
588 VTP-50469 (blue). **(J)** Boxplot denoting gene expression levels of Menin-UTX targets in
589 AML cells isolated from mice harboring *MLL3*-mutant leukemia treated with vehicle (grey)

590 or VTP-50469 (blue). **(K)** Leukemia burden in the bone marrow of recipient mice
591 transplanted with the *MLL3*-mutant PDX and treated with VTP-50469, Palbociclib or the
592 combination of these two inhibitors (measured by % human CD45+ cells). VTP-50469
593 was administered via drug-supplemented rodent chow (0.1%) for 10 days, Palbociclib
594 was given once daily via intraperitoneal injections (35mg/kg) for 7 days. **(L)** FACS plots
595 showing the abundance of human leukemia cells in representative recipient mice from
596 each treatment group. **(M)** Heatmap denoting changes in a cell cycle-associated gene
597 expression signature in FACS-sorted human leukemia cells isolated from recipient mice
598 transplanted with the *MLL3*-mutant PDX and treated with VTP-50469, Palbociclib, or the
599 combination of these two inhibitors.

600 **Figure 6. A molecular switch between mammalian MLL complexes dictates**
601 **response to Menin-MLL inhibition.**

602

603 ## ACKNOWLEDGEMENTS

604 We thank all members of the Allis, Lowe, and Armstrong laboratories for their help and support;
605 Richard Phillips, Robert G. Roeder, Tom W. Muir, Benjamin A. Garcia, and Charles J. Sherr for
606 scientific discussions; David Chen (Chun-Wei Chen) for mouse MLL-AF9 cells, Zhaohui Feng for
607 human leukemia cells, and Laura Whitman (Agilent) for OLS support. C.D.A. was supported by
608 US National Institutes of Health (NIH) grants (P01CA196539 and 5R01CA204639-03), the
609 Leukemia and Lymphoma Society (LLS-SCOR 7006-13), and the Rockefeller University and St.
610 Jude Children's Research Hospital Collaborative on Chromatin Regulation in Pediatric Cancer.
611 S.W.L was supported by a NIH/NCI grant (R01 CA190261) and an Agilent Thought Leader Award,
612 as well as the MSKCC cancer center support grant (P30 CA008748). S.W.L. is the Geoffrey
613 Beene Chair of Cancer Biology and a Howard Hughes Medical Institute Investigator. S.A.A was

614 supported by NIH grants CA176745, CA206963, CA204639 and CA066996. Y.M.S.F was
615 supported by the Damon Runyon-Sohn Pediatric Cancer Fellowship (DRSG-21-17) and NIGMS-
616 MOSAIC K99/R00 Career Development Award (1K99GM140265-01). F.J.S.R. was partially
617 supported by the MSKCC TROT program (5T32CA160001), a MSKCC GMTEC Postdoctoral
618 Researcher Innovation Grant, and is a HHMI Hanna Gray Fellow. F.P. was supported by the
619 German Research Foundation (DFG, PE 3217/1-1) and a Momentum Fellowship award by the
620 Mark Foundation for Cancer Research. D.W.B. was supported by a Ruth L. Kirschstein National
621 Research Service Award (5F32CA217068). E.R.K. was supported by an F31 NRSA predoctoral
622 fellowship from the NIH/NCI (F31CA192835).

623 AUTHOR CONTRIBUTIONS

624 Y.M.S.F., F.J.S.R., F.P, S.A.A, S.W.L., and C.D.A. conceived the study and wrote the manuscript
625 with input from all the authors; Y.M.S.F., F.J.S.R., F.P., Y.X., L.G., M.C.B., and D.C. conducted
626 experiments; D.W.B., T.C., and Y.J.H. analyzed RNA-Seq and ChIP-Seq data; Y.J.H. and E.R.K.
627 analyzed CRISPR-screen data. S.G. and X.S.L. provided genome-wide CRISPR library. A.V.K.,
628 M.M., and E.dS. provided patient-derived xenograft samples. R.M.S. provided primary AML
629 samples from patients in the Syndax trial A.S. provided conceptual advice. S.A.A, S.W.L., and
630 C.D.A. supervised the study and secured funding.

631 DECLARATION OF INTERESTS

632 C.D.A. is a co-founder of Chroma Therapeutics and Constellation Pharmaceuticals and a
633 Scientific Advisory Board member of EpiCypher. S.W.L. is an advisor for and has equity in the
634 following biotechnology companies: ORIC Pharmaceuticals, Faeth Therapeutics, Blueprint
635 Medicines, Geras Bio, Mirimus Inc., and PMV Pharmaceuticals. S.W.L. also acknowledges
636 receiving funding and research support from Agilent Technologies for the purposes of massively

637 parallel oligo synthesis. S.A.A. has been a consultant and/or shareholder for Vitae/Allergan
638 Pharmaceuticals, Epizyme Inc., Imago Biosciences, Cyteir Therapeutics, C4 Therapeutics, Syros
639 Pharmaceuticals, OxStem Oncology, Accent Therapeutics, and Mana Therapeutics. S.A.A. has
640 received research support from Janssen, Novartis, and AstraZeneca. The remaining authors
641 declare no competing interests.

642 **MATERIALS AND METHODS**

643 Plasmids and sgRNA cloning

644 To generate stable Cas9-expressing cell lines, we used lentiCas9-Blast (Addgene, 52962).
645 Human wild-type or mutant (K4M) histone H3.1 were cloned into pCDH-EF1-MCS-IRES-RFP
646 (System Biosciences, CD531A-2). To express sgRNAs, we generated the pUSEPR (U6-sgRNA-
647 EFS-Puro-P2A-TurboRFP) and pUSEPB (U6-sgRNA-EFS-Puro-P2A-TagBFP) lentiviral vectors
648 by Gibson assembly of the following DNA fragments: (i) PCR-amplified U6-sgRNA (improved
649 scaffold)[96] cassette, (ii) PCR-amplified EF1s promoter, (iii) PCR-amplified Puro-P2A-TurboRFP
650 or -TagBFP gene fragment (IDT), and (iv) BsrGI/PmeI-digested pLL3-based lentiviral backbone[97].
651 For sgRNA cloning, pUSEPR and pUSEPB vectors were linearized with BsmBI (NEB) and ligated
652 with BsmBI-compatible annealed and phosphorylated oligos encoding sgRNAs using high
653 concentration T4 DNA ligase (NEB). All sgRNA sequences used are listed in Supplementary
654 Table 1.

655 Cell culture

656 Mouse MLL-AF9 leukemia cells were kindly shared by David Chen (Chun-Wei Chen) and were
657 originally generated by transformation of female mouse bone marrow Lin-Sca1+cKit+ (LSK) cells
658 with an MSCV-IRES-GFP (pMIG) retrovirus expressing the human MLL-AF9 fusion protein and
659 transplanted into sub-lethally irradiated recipient mice as described previously[29,98]. Leukemic

660 blasts were harvested from moribund mice and cultured in vitro in IMDM (Gibco) supplemented
661 with 15% FBS (Gibco), mouse IL-6 (10ng/μL, PeproTech), mouse IL-3 (10ng/μL, PeproTech),
662 mouse SCF (20ng/μL, PeproTech), penicillin (100U/mL, Gibco), streptomycin (100μg/uL, Gibco),
663 L-glutamine (2mM, Gibco), and plasmocin (5μg/mL, InvivoGen). Human leukemia cell lines
664 MV4;11 and OCI-AML3 were kindly shared by Zhaohui Feng and were cultured in RPMI 1640
665 (Corning) supplemented with 10% FBS (Gibco), penicillin (100U/mL, Gibco), streptomycin
666 (100μg/uL, Gibco), L-glutamine (2mM, Gibco), and plasmocin (5μg/mL, InvivoGen). Mouse NIH-
667 3T3 cells were maintained in DMEM (Corning) supplemented with 10% FCS (ATCC), penicillin
668 (100U/mL, Gibco), streptomycin (100μg/uL, Gibco), and plasmocin (5μg/mL, InvivoGen). Human
669 HEK293 cells were maintained in DMEM (Corning) supplemented with 10% FBS (Gibco),
670 penicillin (100U/mL, Gibco), streptomycin (100μg/uL, Gibco), and plasmocin (5μg/mL,
671 InvivoGen). Cas9-expressing cells were generated by lentiviral transduction of lentiCas9-Blast
672 followed by Blasticidin (InvivoGen) selection and validation of Cas9 expression and activity. All
673 cells were confirmed to be free of Mycoplasma contamination and cultured at 37°C and 5% CO_2.

674 Virus production

675 Lentiviruses were produced by co-transfection of HEK293T (ATCC) cells with pUSEPR-EpiV2.0
676 sgRNA library, individual sgRNA plasmids, or lentiCas9-Blast, and packaging vectors psPax2
677 (Addgene, 12260) and pMD2.G (Addgene, 12259) using Lipofectamine 2000 (Invitrogen). Viral
678 supernatants were collected at 48 and 72 hours post transfection and stored at -80°C.

679 Transduction of cell lines

680 Leukemia cells were seeded at a density of 2.5 x 10^5 cells/well of a non-TC-treated 12-well plate
681 in complete medium containing polybrene (10μg/mL, EMD Millipore), and then transduced with
682 lentivirus by centrifugation at 2,500rpm for 90 minutes at 37°C. After a 24-hour incubation, cells

683 were transferred to a new plate containing fresh culture medium. Antibiotic selection or cell sorting
684 was done 48 hours post transduction.

685 Drug treatments

686 For MI-503 (Active Biochem) treatments, leukemia cells were seeded at a density of 4 x 10^5
687 cells/mL, treated with limiting dilutions of the inhibitor as indicated or 0.25% DMSO (vehicle). Cells
688 were re-plated every 4 days to the initial density and re-treated. Viability was assessed at various
689 time points by using the CellTiter-Glo Luminescent Cell Viability assay (Promega) following the
690 manufacturer's guidelines. Ratio of luminescence signal from metabolically active cells in MI-503
691 versus DMSO were plotted to calculate IC50 values (Prism 8, GraphPad). For MI-503 (Active
692 Biochem) and Palbociclib HCl (Selleckchem) combination treatments, 25,000 leukemia cells in
693 250µL of drug-containing medium were seeded in a 48-well plate and viability was assessed every
694 4 days by using the CellTiter-Glo Luminescent Cell Viability assay (Promega). For RNA-Seq and
695 ChIP-Seq experiments, cells were cultured at 4 x 10^5 cells/mL, treated with MI-503
696 (concentrations as indicated in figure legends) or 0.25% DMSO for 4 days. Cells were collected,
697 washed with PBS, pelleted, and flash-frozen before RNA or chromatin isolation. For *in vivo* VTP-
698 50649 treatment, mice were randomly assigned to either normal or 0.1% VTP-50469 rodent
699 special diet[26]. Mice were bled weekly to monitor leukemia burden and euthanized when showing
700 clinical signs of disease (experimental endpoint).

701 Flow cytometric analyses

702 Immunophenotyping of leukemia cells treated with MI-503 (or vehicle), was done by collecting
703 cells post treatment and staining using the indicated conjugated primary antibodies. Stained
704 samples were analyzed on an LSRFortessa (BD Biosciences) flow cytometer. Data analysis was
705 performed using FlowJo (BD Biosciences) software. Intracellular antigens detection was done by
706 using the Foxp3/Transcription Factor Staining Buffer Set (eBioscience) following the

707 manufacturer's guidelines. Conjugated primary antibodies used were: Pacific Blue anti-CD11b
708 (Biolegend, 101224), Alexa Fluor 647 anti-Cas9 (CST, 48796).

709 Xenograft models of AML

710 All animal experiments were performed with the approval of Dana-Farber Cancer Institute's
711 Institutional Animal Care and Use Committee (IACUC). NOD.Cg-*Prkdc*^{scid} *Il2rg*^{tm1Sug}/JicTac (NOG)
712 mice were obtained from Taconic Biosciences (Rensselaer, NY, USA). Non-irradiated 8-12 weeks
713 old adult mice were transplanted with previously established patient-derived xenografts
714 (PDXs)[25,99] via tail vein injection (250,000 cells/mouse). Engraftment of human cells (hCD45^{+})
715 was analyzed and monitored longitudinally by weekly bleeding to quantify hCD45^{+} cells in the
716 peripheral blood by flow cytometry with human CD45-PE and anti-mouse CD45-APC-Cy7
717 antibodies (Biolegend, San Diego, CA, USA). Mice were monitored closely to detect disease
718 onset and treatment started when hCD45^{+} cells were detectable in the peripheral blood. Mice
719 were randomly assigned to either normal or 0.1% VTP-50469 rodent special diet[25]. Mice were
720 bled weekly to monitor leukemia burden as described above and euthanized when showing
721 clinical signs of disease (experimental endpoint). Leukemia cells from a subset of these animals
722 were harvested after seven days of treatment to perform RNA-Seq.

723 Longitudinal analysis of AML patient treated with SNDX-5613

724 Peripheral blood of patients was taken under informed consent according to the Declaration of
725 Helsinki during routine blood draws at screening and different timepoints during the first cycle of
726 treatment with SDNX-5613 within the AUGMENT-101 clinical trial (NCT04065399). Peripheral
727 blood mononuclear cells (PBMCs) were subsequently isolated using Ficoll (BD Bioscience,
728 Franklin Lakes, NJ, USA) gradient centrifugation, viably frozen, and banked at the Dana-Farber
729 Cancer Institute, Boston, MA (approved institutional protocol, IRB: #01-206). For longitudinal
730 analysis, samples were thawed, washed twice in PBS, and stained with anti-human CD45 (PE)

731 and anti-human CD117 (APC) (Biolegend, San Diego, CA, USA). CD45-low/CD117+ leukemia
732 cells were FACS sorted (MA900 sorter, Sony Biotechnology, San Jose, CA, USA) and
733 subsequently processed for RNA-Seq (see methods section on RNA-Seq).

734 Immunoblotting

735 Whole cell lysates were separated by SDS-PAGE, transferred to a PVDF membrane (EMD
736 Millipore), blocked in 5% non-fat milk in TBS plus 0.5% Tween-20 (Sigma-Aldrich), probed with
737 primary antibodies, and detected with HRP-conjugated anti-rabbit or anti-mouse secondary
738 antibodies (GE Healthcare). Primary antibodies used included: anti-Cas9 (CST, 14697), anti-UTX
739 (CST, 33510), anti-Menin (Bethyl, A300-105A), anti-NF-YA (Santa Cruz Biotechnology, sc-
740 17753), anti-Actin (abcam, ab8224), anti-HSP90 (BD Biosciences, 610418), anti-HA (Biolegend,
741 901501), anti-H3K4me1 (abcam, ab8895), anti-H3K4me3 (CST, 9751), anti-H3 (abcam, ab1791).

742 Locus-specific DNA sequencing

743 To determine the mutational status of the *Men1* and *Utx* loci in cells targeted by CRISPR-Cas9,
744 we performed next generation sequencing of PCR-amplified target regions. Genomic DNA
745 (gDNA) was isolated using the DNeasy Blood & Tissue Kit (Qiagen) following the manufacturer's
746 guidelines. Amplification of target regions was performed from 500ng of gDNA using Q5 High-
747 Fidelity 2X Master Mix (NEB) and primers listed in Supplementary Table 1. PCR products were
748 purified using the QIAquick PCR Purification Kit (Qiagen) and sequenced on Illumina instruments
749 at GENEWIZ (Amplicon-EZ service).

750 RNA isolation, qRT-PCR analyses, and RNA sequencing

751 Total RNA was isolated from cells using the RNeasy kit (Qiagen, Hilden, Germany). RNA was
752 reverse transcribed with High-Capacity cDNA Reverse Transcription kits (Applied Biosystems)
753 following the manufacturer’s instructions. Quantitative PCRs (qRT-PCRs) were performed using

754 the TaqMan Gene Expression Master Mix (Applied Biosystems) with the StepOne Real-Time
755 System (Applied Biosystems). TaqMan gene expression assays were used. ActB was used as
756 the endogenous control for normalization and relative gene expression was calculated by using
757 the comparative CT method. The mouse gene probes used were: *ActB* (Mm02619580_g1),
758 *Hoxa9* (Mm00439364_m1), *Meis1* (Mm00487664_m1), *Utx* (*Kdm6a*) (Mm00801998_m1), *Men1*
759 (Mm00484957_m1). Quality of extracted RNA for sequencing was assessed by RIN using a
760 Bioanalyzer (Agilent) and quantified by TapeStation (Agilent). Poly(A) mRNA enrichment and
761 library preparation was performed using the NEBNext Poly(A) mRNA Magnetic Isolation Module
762 and NEBNext Ultra II RNA Library Prep kit (NEB). Sequencing was done using the Illumina
763 NextSeq500 to obtain >20 million 75bp single-end or 37bp paired-end reads per sample or at
764 Genewiz (HiSeq, 150bp, paired end) (Illumina, South Plainfield, NJ, USA).

765 Cloning of sgRNA library targeting mouse chromatin regulators

766 sgRNA sequences (six per gene) targeting 616 mouse chromatin regulators (for a total of 3,696
767 sgRNAs) (Supplementary Table 1) were designed using the Broad Institute sgRNA Designer
768 tool[100]. We also included 36 non-targeting control sgRNAs obtained from the GeCKOv2 Mouse
769 CRISPR library[101] (for a total of 3,732 sgRNAs). This library was divided into 6 pools (each
770 composed of 616 targeting and 6 non-targeting sgRNAs), synthesized by Agilent Technologies,
771 and cloned into the pUSEPR lentiviral vector[102] using a modified version of the protocol published
772 by Doench et al[100] to ensure a library representation of >10,000X. Briefly, each sub-pool was
773 selectively amplified using barcoded forward and reverse primers that append cloning adapters
774 at the 5' and 3' ends of the sgRNA insert (Supplementary Table 1), purified using the QIAquick
775 PCR Purification Kit (Qiagen), and ligated into BsmBI-digested and dephosphorylated pUSEPR
776 vector using high-concentration T4 DNA ligase (NEB). A minimum of 1.2 ug of ligated pUSEPR
777 plasmid DNA per sub-pool was electroporated into Endura electrocompetent cells (Lucigen),
778 recovered for one hour at 37°C, plated across four 15cm LB-Carbenicillin plates (Teknova), and

779 incubated at 37°C for 16 hours. The total number of bacterial colonies per sub-pool was quantified
780 using serial dilution plates to ensure a library representation of >10,000X (>6.2 million colonies
781 per sub-pool). The next morning, bacterial colonies were scraped and briefly expanded for 4 hours
782 at 37°C in 500mL of LB-Carbenicillin. Plasmid DNA was isolated using the Plasmid Plus Maxi Kit
783 (Qiagen).

784 To assess sgRNA distribution in each of the sub-pools, as well as the master pool (composed of
785 equimolar amounts of plasmid DNA from each individual sub-pool), we amplified the sgRNA target
786 region using primers that append Illumina sequencing adapters on the 5' and 3' ends of the
787 amplicon, as well as a random nucleotide stagger and unique demultiplexing barcode on the 5'
788 end (Supplementary Table 1). Library amplicons were size-selected on a 2.5% agarose gel,
789 purified using the QIAquick Gel Extraction Kit (Qiagen), and sequenced on an Illumina NextSeq
790 instrument (75nt single end reads).

791 Chromatin-focused CRISPR-Cas9 genetic screening

792 To ensure that most cells harbor a single sgRNA integration event, we determined the volume of
793 viral supernatant that would achieve an MOI of ~0.3 upon spinfection of a population of Cas9-
794 expressing leukemia cells. Briefly, cells were plated at a concentration of $2.5x10^5$ per well in 12-
795 well plates along with increasing volumes of master pool viral supernatant (0, 25, 100, 200, 500,
796 1000, and 2000μL) and polybrene (10 μg/mL, EMD Millipore). Cells were then centrifuged at
797 1,500rpm for 2 hours at 37°C and incubated at 37°C overnight. Viral infection efficiency was
798 determined by the percentage of tRFP+ cells assessed by flow cytometry on an LSRFortessa (BD
799 Biosciences) instrument 72 hours post infection.

800 Each step of the screen - from infection to sequencing - was optimized to achieve a minimum
801 representation of 1000X. To ensure a representation of 1000X at the transduction step, we
802 spinfected a total of 20 million cells across seven 12-well plates in triplicate (for a total of twenty

803 one 12-well plates) using the volume of viral supernatant that would achieve a 30% infection rate
804 (6 million transduced cells per technical replicate).

805 24 hours after infection, cells were pooled into 2 x T225 flasks (Corning) per infection replicate
806 and selected with 2.5μg/mL puromycin (Gibco) for 4 days. Subsequently, 6 million puromycin-
807 selected cells were pelleted and stored at -20°C (T0/Input population) while the rest were plated
808 into either DMSO- or MI-503-containing media (at an IC50 concentration) and cultured until the
809 population reached 12 cumulative population doublings (TF/Final). At least 6 million cells were
810 harvested and pelleted for this final time point. Genomic DNA from MLL-AF9 cells was isolated
811 using the DNeasy Blood & Tissue Kit (Qiagen) following the manufacturer's guidelines.

812 As previously published[103], we assumed that each cell contains approximately 6.6 pg of genomic
813 DNA (gDNA). Therefore, deconvolution of the screen at 1000X required sampling ~4 million x 6.6
814 pg of gDNA, or ~26.4 ug. We employed a modified 2-step PCR version of the protocol published
815 by Doench et al[100]. Briefly, we perform an initial “enrichment” PCR, whereby the integrated sgRNA
816 cassettes are amplified from gDNA, followed by a second PCR to append Illumina sequencing
817 adapters on the 5’ and 3’ ends of the amplicon, as well as a random nucleotide stagger and unique
818 demultiplexing barcode on the 5’ end. Each “PCR1” reaction contains 25μL of Q5 High-Fidelity
819 2X Master Mix (NEB), 2.5μL of Nuc PCR#1 Fwd Primer (10μM), 2.5μL of Nuc PCR#1 Rev Primer
820 (10μM), and 5μg of gDNA in 20μL of water (for a total volume of 50μL per reaction). The number
821 of PCR1 reactions were scaled accordingly; therefore, we performed six PCR1 reactions per
822 technical replicate, per time point (T0 or TF), and per condition (DMSO or MI-503). PCR1
823 amplicons were purified using the QIAquick PCR Purification Kit (Qiagen) and used as template
824 for “PCR2” reactions. Each PCR2 reaction contains 25μL of Q5 High-Fidelity 2X Master Mix
825 (NEB), 2.5μL of a unique Nuc PCR#2 Fwd Primer (10μM), 2.5μL of Nuc PCR#2 Rev Primer
826 (10μM), and 300ng of PCR1 product in 20μL of water (for a total volume of 50μL per reaction).
827 We performed two PCR2 reactions per PCR1 product. Library amplicons were size-selected on

828 a 2.5% agarose gel, purified using the QIAquick Gel Extraction Kit (Qiagen), and sequenced on
829 an Illumina NextSeq500 instrument (75nt single end reads). All primer sequences are available
830 in Supplementary Table 1. PCR Program for PCR1 and PCR2: 1) 98°C x 30s; 2) 98°C x 10s; 3)
831 65°C x 30s; 4) 72°C x 30s; 5) Go to step 2 x 24 cycles; 6) 72°C x 2 min; 7) 4°C forever.

832 Genome-wide CRISPR-Cas9 genetic screening

833 Paired mouse genome-scale CRISPR-Cas9 screening libraries (M1/M2) were provided by
834 Shengqing Gu and Xiaole Shirley Liu (Addgene Pooled Library #1000000173). The M1 and M2
835 libraries cover protein coding genes of the genome with a total of 10 guide RNAs per gene.
836 Lentivirus was produced using each separate library pool and used to transduce each $5x10^8$ MLL-
837 AF9 cells at low MOI. 48 hours after library transduction, cells were selected with blasticidin
838 (5ug/ml). After 5 days of antibiotic selection, a baseline (T0) sample was collected, and cells were
839 cultured in duplicate before harvest of terminal samples after 12 days (TF). Subsequently,
840 genomic DNA was isolated using phenol-chloroform extraction and sgRNA libraries were
841 deconvoluted using next-generation sequencing essentially as described above.

842 Analysis of CRISPR-Cas9 genetic screen data

843 FASTQ files were processed and trimmed to retrieve sgRNA target sequences followed by
844 alignment to the reference sgRNA library file. Sequencing read counts were summarized at gene
845 level per sample and used as input to run differential analysis using DESeq2 package. The log2
846 fold change values were used as 'Gene Score' for the final visualization. Genome-wide screening
847 data was analyzed using MAGeCK MLE essentially as described in the original publication[104].
848 See Supplementary Table 2 for all raw screening data.

849 Growth competition assays

850 Cas9-expressing cells were virally transduced with the designated constructs (pUSEPR-sgRNA,
851 pUSEPB-sgRNA, pCDH-cDNA) in 12-well plates at 30-40% infection rate (three infection
852 replicates). Cells were monitored by flow cytometry over time using an LSRFortessa (BD
853 Biosciences) flow cytometer and relative growth of sgRNA-containing cells was assesed. Flow
854 cytometry data was analyzed with FlowJo software (BD Biosciences). The percentage of single
855 positive (SP) (tRFP+ or BFP+) or double positive (DP) (tRFP+/BFP+) cells was normalized to
856 their respective "T0" time-point values (assessed on day 2 or 3 post transduction, as indicated in
857 the figure legend). Normalized values were log2-transformed, and the differential fitness of cells
858 was calculated as follow:

859 Differential Fitness = log2(Normalized DP) - log2(Normalized SP)

860 Chromatin immunoprecipitation (ChIP)

861 Cross-linking ChIP in mouse leukemia and NIH-3T3 cells was performed with 10-20x10^7 cells per
862 immunoprecipitation. After drug (or vehicle) treatment, cells were collected, washed once with
863 ice-cold PBS, and flash-frozen. Cells were resuspended in ice-cold PBS and cross-linked using
864 1% paraformaldehyde (PFA) (Electron Microscopy Sciences) for 5 minutes at room temperature
865 with gentle rotation. Unreacted PFA was quenched with glycine (final concentration 125mM) for
866 5 minutes at room temperature with gentle rotation. Cells were washed once with ice-cold PBS
867 and pelleted by centrifugation (800g for 5 minutes). To obtain a soluble chromatin extract, cells
868 were resuspended in 1mL of LB1 (50mM HEPES pH 7.5, 140mM NaCl, 1mM EDTA, 10%
869 glycerol, 0.5% NP-40, 0.25% Triton X-100, 1X complete protease inhibitor cocktail) and incubated
870 at 4°C for 10 minutes while rotating. Samples were centrifuged (1400g for 5 minutes),
871 resuspended in 1mL of LB2 (10mM Tris-HCl pH 8.0, 200mM NaCl, 1mM EDTA, 0.5mM EGTA,
872 1X complete protease inhibitor cocktail), and incubated at 4°C for 10 minutes while rotating.
873 Finally, samples were centrifuged (1400g for 5 minutes) and resuspended in 1mL of LB3 (10mM

874 Tris-HCl pH 8.0, 100mM NaCl, 1mM EDTA, 0.5mM EGTA, 0.1% sodium deoxycholate, 0.5% N-
875 Lauroylsarcosine, 1X complete protease inhibitor cocktail). Samples were homogenized by
876 passing 7-8 times through a 28-gauge needle and Triton X-100 was added to a final concentration
877 of 1%. Chromatin extracts were sonicated for 14 minutes using a Covaris E220 focused
878 ultrasonicator. Lysates were centrifuged at maximum speed for 10 minutes at 4°C and 5% of
879 supernatant was saved as input DNA. Beads were prepared by incubating in 0.5% BSA in PBS
880 and antibodies overnight (100µL of Dynabeads Protein A or Protein G (Invitrogen) plus 20µL of
881 antibody). Antibodies used were: anti-Menin (Bethyl, A300-105A), anti-UTX (Bethyl, A302-374A),
882 anti-MLL1 (N-term-specific, Bethyl, A300-086A), anti-MLL3/4 (kindly provided by the Wysocka
883 laboratory[41], anti-NF-YA (Santa Cruz Biotechnology, sc-17753), anti-H3K4me1 (abcam, ab8895),
884 anti-H3K4me3 (Active Motif, 39159), and anti-H4K16ac (Active Motif, 39167). Antibody-Beads
885 mixes were washed with 0.5% BSA in PBS and then added to the lysates overnight while rotating
886 at 4°C. Beads were then washed six times with RIPA buffer (50mM HEPES pH 7.5, 500mM LiCl,
887 1mM EDTA, 0.7% sodium-deoxycholate, 1% NP-40) and once with TE-NaCl Buffer (10mM Tris-
888 HCl pH 8.0, 50mM NaCl, 1mM EDTA). Chromatin was eluted from beads in Elution buffer (50mM
889 Tris-HCl pH 8.0, 10mM EDTA, 1% SDS) by incubating at 65°C for 30 minutes while shaking,
890 supernatant was removed by centrifugation, and crosslinking was reversed by further incubating
891 chromatin overnight at 65°C. The eluted chromatin was then treated with RNase A (10mg/mL) for
892 1 hour at 37°C and with Proteinase K (Roche) for 2 hours at 55°C. DNA was purified by using
893 phenol-chloroform extraction followed with ethanol precipitation. The NEBNext Ultra II DNA
894 Library Prep kit was used to prepare samples for sequencing on an Illumina NextSeq500 (75bp
895 read length, single-end, or 37bp read length, paired-end).

896 <u>ChIP-Seq analysis</u>

897 ChIP-sequencing samples were sequenced using the Illumina NextSeq500. ChIP-seq reads were
898 aligned using Rsubread's align method and predicted fragment lengths calculated by the ChIPQC

899 R Bioconductor package[105,106]. Normalized, fragment extended signal bigWigs were created using
900 the rtracklayer R Bioconductor package. Peak calls were made in MACS2 software[107]. Read
901 counts in peaks were calculated using the featureCounts method in the Rsubread library[106].
902 Differential ChIP-seq signal were identified using the binomTest from the edgeR R Bioconductor
903 package[108]. Annotation of genomic regions to genes, biological functions, and pathways were
904 performed using the ChIPseeker R Bioconductor package[109]. Meta-peak plots were produced
905 using the soGGi package and ChIP-seq signal heatmaps generated using the Deeptools and
906 profileplyr software[110]. Plots showing ChIP-Seq read signal over transcription start sites (TSSs)
907 were made with the ngs.plot software package (v2.61) (ref. 111). Overlaps between peak sets
908 were determined using the ChIPpeakAnno R Bioconductor package with a maximum gap
909 between peaks set to 1kb (ref. 112). Peaks were annotated with both genes and the various types
910 of genomic regions using the ChIPseeker R Bioconductor package[109]. Range-based heatmaps
911 showing signal over genomic regions were generated using the soGGi and profileplyr R
912 Bioconductor package to quantify read signal and group the peak ranges and the deepTools
913 software package (v3.3.1) to generate the heatmaps[110]. Any regions included in the ENCODE
914 blacklisted regions of the genome were excluded from all region-specific analyses[113]. For some
915 ChIP-seq experiments, raw Illumina NextSeq BCL files were converted to FASTQs using Illumina
916 bcl2fastq v02.14.01.07 and reads trimmed using Trimmomatic v0.36 (phred quality threshold 33)
917 and uploaded to the to the Basepair-server (basepairtech.com). Alignment and ChIP-seq QC was
918 performed on the basepair platform (Bowtie2). Peak calling was performed using MACS (v.1.4)
919 within the basepair platform utilizing the default parameters.

920 RNA-Seq analysis

921 RNA-Seq samples were sequenced using the Illumina NextSeq500. Transcript abundance was
922 computed from FASTQ files using Salmon and the GENCODE reference transcript sequences,
923 transcript counts were imported into R with the tximport R Bioconductor package, and differential

924 gene expression was determined with the DESeq2 R Bioconductor package[114-116]. The data was
925 visualized using the ggplot2 R package. Normalized counts were extracted from the DESeq2
926 results and z-scores for the indicated gene sets were visualized using both heatmaps and
927 boxplots. Heatmaps showing gene expression changes across samples were generated using
928 the pheatmap R package and boxplots were made with the ggplot2 R package. Gene ontology
929 analysis using the KEGG 2019 database was performed using the Enrichr tool[56,68].

930 Statistical analyses

931 Statistical tests were used as indicated in Figure legends. Generation of plots and statistical
932 analyses were performed using Prism 8 (GraphPad). Error bars represent standard deviation,
933 unless otherwise noted. We used Student's t-test (unpaired, two-tailed) to assess significance
934 between treatment and control groups, and to calculate P values. $P<0.05$ was considered
935 statistically significant.

936 Source data availability

937 Data supporting the findings of this study are reported in Extended Data Figures 1-27 and
938 Supplementary Tables 1-4. All raw data corresponding to high-throughput approaches (CRISPR
939 screens, RNA-Seq, and ChIP-Seq) is available through NCBI GEO (Accession: GSE186711. Go
940 to https://www.ncbi.nlm.nih.gov/geo/query/acc.cgi?acc=GSE186711 and enter token
941 *wpkrckicxnsvxit* into the box to get access to datasets). All reagents and materials generated in
942 this study will be available to the scientific community through Addgene and/or MTAs. Further
943 information and requests for resources and reagents should be directed to and will be fulfilled by
944 the Lead Contacts: C. David Allis (alliscd@rockefeller.edu), Scott W. Lowe (lowes@mskcc.org),
945 and Scott. A. Armstrong (Scott_Armstrong@dfci.harvard.edu).

946 **REFERENCES**

1 Guru, S. C. *et al.* Menin, the product of the MEN1 gene, is a nuclear protein. *Proceedings of the National Academy of Sciences* **95**, 1630-1634, doi:papers3://publication/doi/10.1073/pnas.95.4.1630 (1998).

2 Hughes, C. M. *et al.* Menin associates with a trithorax family histone methyltransferase complex and with the Hoxc8 locus. *Mol Cell* **13**, 587-597, doi:papers3://publication/doi/10.1016/s1097-2765(04)00081-4 (2004).

3 Milne, T. A. *et al.* Menin and MLL cooperatively regulate expression of cyclin-dependent kinase inhibitors. *Proceedings of the National Academy of Sciences* **102**, 749-754, doi:papers3://publication/doi/10.1073/pnas.0408836102 (2005).

4 Yokoyama, A. *et al.* The menin tumor suppressor protein is an essential oncogenic cofactor for MLL-associated leukemogenesis. *Cell* **123**, 207-218, doi:papers3://publication/doi/10.1016/j.cell.2005.09.025 (2005).

5 Bres, V., Yoshida, T., Pickle, L. & Jones, K. A. SKIP interacts with c-Myc and Menin to promote HIV-1 Tat transactivation. *Mol Cell* **36**, 75-87, doi:papers3://publication/doi/10.1016/j.molcel.2009.08.015 (2009).

6 Agarwal, S. K. & Jothi, R. Genome-wide characterization of menin-dependent H3K4me3 reveals a specific role for menin in the regulation of genes implicated in MEN1-like tumors. *PLoS ONE* **7**, e37952, doi:papers3://publication/doi/10.1371/journal.pone.0037952 (2012).

7 Huang, J. *et al.* The same pocket in menin binds both MLL and JUND but has opposite effects on transcription. *Nature 2018* **482**, 542-546, doi:papers3://publication/doi/10.1038/nature10806 (2012).

8 Kaji, H., Canaff, L., Lebrun, J. J., Goltzman, D. & Hendy, G. N. Inactivation of menin, a Smad3-interacting protein, blocks transforming growth factor type beta signaling. *Proceedings of the National Academy of Sciences* **98**, 3837-3842, doi:papers3://publication/doi/10.1073/pnas.061358098 (2001).

9 Sowa, H. *et al.* Inactivation of menin, the product of the multiple endocrine neoplasia type 1 gene, inhibits the commitment of multipotential mesenchymal stem cells into the osteoblast lineage. *J Biol Chem* **278**, 21058-21069, doi:papers3://publication/doi/10.1074/jbc.M302044200 (2003).

10 Yokoyama, A. & Cleary, M. L. Menin critically links MLL proteins with LEDGF on cancer-associated target genes. *Cancer Cell* **14**, 36-46, doi:papers3://publication/doi/10.1016/j.ccr.2008.05.003 (2008).

11 Balogh, K., Rácz, K., Patócs, A. & Hunyady, L. Menin and its interacting proteins: elucidation of menin function. *Trends Endocrinol. Metab.* **17**, 357-364, doi:papers3://publication/doi/10.1016/j.tem.2006.09.004 (2006).

12 Yokoyama, A. *et al.* Leukemia proto-oncoprotein MLL forms a SET1-like histone methyltransferase complex with menin to regulate Hox gene expression. *Mol Cell Biol* **24**, 5639-5649, doi:papers3://publication/doi/10.1128/MCB.24.13.5639-5649.2004 (2004).

13 Wang, P. *et al.* Global analysis of H3K4 methylation defines MLL family member targets and points to a role for MLL1-mediated H3K4 methylation in the regulation of transcriptional initiation by RNA polymerase II. *Mol Cell Biol* **29**, 6074-6085, doi:papers3://publication/doi/10.1128/MCB.00924-09 (2009).

14 Chandrasekharappa, S. C. *et al.* Positional cloning of the gene for multiple endocrine neoplasia-type 1. *Science* **276**, 404-407, doi:papers3://publication/doi/10.1126/science.276.5311.404 (1997).

15 Jiao, Y. *et al.* DAXX/ATRX, MEN1, and mTOR pathway genes are frequently altered in pancreatic neuroendocrine tumors. *Science* **331**, 1199-1203, doi:papers3://publication/doi/10.1126/science.1200609 (2011).

16 Asgharian, B. *et al.* Cutaneous tumors in patients with multiple endocrine neoplasm type 1 (MEN1) and gastrinomas: prospective study of frequency and development of criteria with high sensitivity and specificity for MEN1. *J. Clin. Endocrinol. Metab.* **89**, 5328-5336, doi:papers3://publication/doi/10.1210/jc.2004-0218 (2004).

17 Pei, X.-H., Bai, F., Smith, M. D. & Xiong, Y. p18Ink4c collaborates with Men1 to constrain lung stem cell expansion and suppress non-small-cell lung cancers. *Cancer Res* **67**, 3162-3170, doi:papers3://publication/doi/10.1158/0008-5472.CAN-06-4517 (2007).

18 Falchetti, A. *et al.* Multiple endocrine neoplasia type 1 (MEN1): not only inherited endocrine tumors. *Genet. Med.* **11**, 825-835, doi:papers3://publication/doi/10.1097/GIM.0b013e3181be5c97 (2009).

19 Xu, B. *et al.* Menin promotes hepatocellular carcinogenesis and epigenetically up-regulates Yap1 transcription. *Proc Natl Acad Sci USA* **110**, 17480-17485, doi:papers3://publication/doi/10.1073/pnas.1312022110 (2013).

20 Krivtsov, A. V. & Armstrong, S. A. MLL translocations, histone modifications and leukaemia stem-cell development. *Nat Rev Cancer* **7**, 823-833, doi:papers3://publication/doi/10.1038/nrc2253 (2007).

21 Lemos, M. C. & Thakker, R. V. Multiple endocrine neoplasia type 1 (MEN1): analysis of 1336 mutations reported in the first decade following identification of the gene. *Hum. Mutat.* **29**, 22-32, doi:papers3://publication/doi/10.1002/humu.20605 (2008).

22 Borkin, D. *et al.* Pharmacologic inhibition of the Menin-MLL interaction blocks progression of MLL leukemia in vivo. *Cancer Cell* **27**, 589-602, doi:papers3://publication/doi/10.1016/j.ccell.2015.02.016 (2015).

23 Dreijerink, K. M. A. *et al.* Enhancer-Mediated Oncogenic Function of the Menin Tumor Suppressor in Breast Cancer. *Cell Rep* **18**, 2359-2372, doi:papers3://publication/doi/10.1016/j.celrep.2017.02.025 (2017).

24 Grembecka, J. *et al.* Menin-MLL inhibitors reverse oncogenic activity of MLL fusion proteins in leukemia. *Nat Meth* **8**, 277-284, doi:papers3://publication/doi/10.1038/nchembio.773 (2012).

25 Krivtsov, A. V. *et al.* A Menin-MLL Inhibitor Induces Specific Chromatin Changes and Eradicates Disease in Models of MLL-Rearranged Leukemia. *Cancer Cell* **36**, 660-673.e611, doi:papers3://publication/doi/10.1016/j.ccell.2019.11.001 (2019).

26 Malik, R. *et al.* Targeting the MLL complex in castration-resistant prostate cancer. *Nature Medicine* **21**, 344-352, doi:papers3://publication/doi/10.1038/nm.3830 (2015).

27 Uckelmann, H. J. *et al.* Therapeutic targeting of preleukemia cells in a mouse model of NPM1 mutant acute myeloid leukemia. *Science* **367**, 586-590, doi:papers3://publication/doi/10.1126/science.aax5863 (2020).
28 Kurmasheva, R. T. *et al.* Evaluation of VTP-50469, a menin-MLL1 inhibitor, against Ewing sarcoma xenograft models by the pediatric preclinical testing consortium. *Pediatr Blood Cancer* **67**, e28284, doi:10.1002/pbc.28284 (2020).
29 Chen, C.-W. *et al.* DOT1L inhibits SIRT1-mediated epigenetic silencing to maintain leukemic gene expression in MLL-rearranged leukemia. *Nature Medicine* **21**, 335-343, doi:papers3://publication/doi/10.1038/nm.3832 (2015).
30 Bernt, K. M. *et al.* MLL-rearranged leukemia is dependent on aberrant H3K79 methylation by DOT1L. *Cancer Cell* **20**, 66-78, doi:papers3://publication/doi/10.1016/j.ccr.2011.06.010 (2011).
31 Chang, M.-J. *et al.* Histone H3 lysine 79 methyltransferase Dot1 is required for immortalization by MLL oncogenes. *Cancer Res* **70**, 10234-10242, doi:papers3://publication/doi/10.1158/0008-5472.CAN-10-3294 (2010).
32 Mueller, D. *et al.* Misguided transcriptional elongation causes mixed lineage leukemia. *PLoS Biol* **7**, e1000249, doi:papers3://publication/doi/10.1371/journal.pbio.1000249 (2009).
33 Zuber, J. *et al.* RNAi screen identifies Brd4 as a therapeutic target in acute myeloid leukaemia. *Nature 2018* **478**, 524-528, doi:papers3://publication/doi/10.1038/nature10334 (2011).
34 Zuber, J. *et al.* An integrated approach to dissecting oncogene addiction implicates a Myb-coordinated self-renewal program as essential for leukemia maintenance. *Genes & Development* **25**, 1628-1640, doi:papers3://publication/doi/10.1101/gad.17269211 (2011).
35 Milne, T. A. *et al.* MLL targets SET domain methyltransferase activity to Hox gene promoters. *Mol Cell* **10**, 1107-1117, doi:papers3://publication/doi/10.1016/s1097-2765(02)00741-4 (2002).
36 Nakamura, T. *et al.* ALL-1 is a histone methyltransferase that assembles a supercomplex of proteins involved in transcriptional regulation. *Mol Cell* **10**, 1119-1128, doi:Doi 10.1016/S1097-2765(02)00740-2 (2002).
37 Dorighi, K. M. *et al.* Mll3 and Mll4 Facilitate Enhancer RNA Synthesis and Transcription from Promoters Independently of H3K4 Monomethylation. *Mol Cell* **66**, 568-576.e564, doi:papers3://publication/doi/10.1016/j.molcel.2017.04.018 (2017).
38 Herz, H.-M. *et al.* Enhancer-associated H3K4 monomethylation by Trithorax-related, the Drosophila homolog of mammalian Mll3/Mll4. *Genes & Development* **26**, 2604-2620, doi:papers3://publication/doi/10.1101/gad.201327.112 (2012).
39 Hu, D. *et al.* The MLL3/MLL4 branches of the COMPASS family function as major histone H3K4 monomethylases at enhancers. *Mol Cell Biol* **33**, 4745-4754, doi:papers3://publication/doi/10.1128/MCB.01181-13 (2013).
40 Lee, J. *et al.* A tumor suppressive coactivator complex of p53 containing ASC-2 and histone H3-lysine-4 methyltransferase MLL3 or its paralogue MLL4. *Proc Natl Acad Sci USA* **106**, 8513-8518, doi:papers3://publication/doi/10.1073/pnas.0902873106 (2009).

41 Wang, S.-P. *et al.* A UTX-MLL4-p300 Transcriptional Regulatory Network Coordinately Shapes Active Enhancer Landscapes for Eliciting Transcription. *Mol Cell* **67**, 308-321.e306, doi:papers3://publication/doi/10.1016/j.molcel.2017.06.028 (2017).
42 Issaeva, I. *et al.* Knockdown of ALR (MLL2) reveals ALR target genes and leads to alterations in cell adhesion and growth. *Mol Cell Biol* **27**, 1889-1903, doi:papers3://publication/doi/10.1128/MCB.01506-06 (2007).
43 Santos, M. A. *et al.* DNA-damage-induced differentiation of leukaemic cells as an anti-cancer barrier. *Nature 2018* **514**, 107-111, doi:papers3://publication/doi/10.1038/nature13483 (2014).
44 Sun, Y. *et al.* HOXA9 Reprograms the Enhancer Landscape to Promote Leukemogenesis. *Cancer Cell* **34**, 643-658.e645, doi:papers3://publication/doi/10.1016/j.ccell.2018.08.018 (2018).
45 Chen, C. *et al.* MLL3 is a haploinsufficient 7q tumor suppressor in acute myeloid leukemia. *Cancer Cell* **25**, 652-665, doi:papers3://publication/doi/10.1016/j.ccr.2014.03.016 (2014).
46 Gažová, I., Lengeling, A. & Summers, K. M. Lysine demethylases KDM6A and UTY: The X and Y of histone demethylation. *Molecular Genetics and Metabolism* **127**, 31-44, doi:papers3://publication/doi/10.1016/j.ymgme.2019.04.012 (2019).
47 Kooistra, S. M. & Helin, K. Molecular mechanisms and potential functions of histone demethylases. *Nat Rev Mol Cell Biol* **13**, 297-311, doi:papers3://publication/doi/10.1038/nrm3327 (2012).
48 Meyer, C. *et al.* The MLL recombinome of acute leukemias in 2017. *Leukemia* **32**, 273-284, doi:papers3://publication/doi/10.1038/leu.2017.213 (2018).
49 Thirman, M. J. *et al.* Rearrangement of the MLL gene in acute lymphoblastic and acute myeloid leukemias with 11q23 chromosomal translocations. *N Engl J Med* **329**, 909-914, doi:10.1056/NEJM199309233291302 (1993).
50 Kuhn, M. W. *et al.* Targeting Chromatin Regulators Inhibits Leukemogenic Gene Expression in NPM1 Mutant Leukemia. *Cancer Discov* **6**, 1166-1181, doi:10.1158/2159-8290.CD-16-0237 (2016).
51 Tiacci, E. *et al.* The NPM1 wild-type OCI-AML2 and the NPM1-mutated OCI-AML3 cell lines carry DNMT3A mutations. *Leukemia* **26**, 554-557, doi:papers3://publication/doi/10.1038/leu.2011.238 (2012).
52 Chen, Y. *et al.* Distinct pathways affected by menin versus MLL1/MLL2 in MLL-rearranged acute myeloid leukemia. *Exp Hematol* **69**, 37-42, doi:10.1016/j.exphem.2018.10.001 (2019).
53 Kumar, A. R. *et al.* A role for MEIS1 in MLL-fusion gene leukemia. *Blood* **113**, 1756-1758, doi:papers3://publication/doi/10.1182/blood-2008-06-163287 (2009).
54 Lange, B. *et al.* Growth-Factor Requirements of Childhood Acute-Leukemia - Establishment of Gm-Csf Dependent Cell-Lines. *Blood* **70**, 192-199, doi:papers3://publication/doi/10.1182/blood.V70.1.192.192 (1987).
55 Scacheri, P. C. *et al.* Genome-wide analysis of menin binding provides insights into MEN1 tumorigenesis. *PLoS Genet* **2**, e51, doi:papers3://publication/doi/10.1371/journal.pgen.0020051 (2006).

56 Wang, J. K. *et al.* The histone demethylase UTX enables RB-dependent cell fate control. *Genes & Development* **24**, 327-332, doi:papers3://publication/doi/10.1101/gad.1882610 (2010).
57 Cheng, J. *et al.* A role for H3K4 monomethylation in gene repression and partitioning of chromatin readers. *Mol Cell* **53**, 979-992, doi:papers3://publication/doi/10.1016/j.molcel.2014.02.032 (2014).
58 Morgan, M. A. J. & Shilatifard, A. Reevaluating the roles of histone-modifying enzymes and their associated chromatin modifications in transcriptional regulation. *Nat Genet* **52**, 1271-1281, doi:10.1038/s41588-020-00736-4 (2020).
59 Jang, Y. *et al.* H3.3K4M destabilizes enhancer H3K4 methyltransferases MLL3/MLL4 and impairs adipose tissue development. *Nucleic Acids Res* **47**, 607-620, doi:papers3://publication/doi/10.1093/nar/gky982 (2019).
60 La, P. *et al.* Direct binding of DNA by tumor suppressor menin. *J Biol Chem* **279**, 49045-49054, doi:10.1074/jbc.M409358200 (2004).
61 Oldfield, A. J. *et al.* NF-Y controls fidelity of transcription initiation at gene promoters through maintenance of the nucleosome-depleted region. *Nat Commun* **10**, 3072, doi:10.1038/s41467-019-10905-7 (2019).
62 Jenuwein, T. & Allis, C. D. Translating the Histone Code. *Science* **293**, 1074-1080, doi:doi:10.1126/science.1063127 (2001).
63 Akhtar, A. & Becker, P. B. Activation of Transcription through Histone H4 Acetylation by MOF, an Acetyltransferase Essential for Dosage Compensation in Drosophila. *Mol Cell* **5**, 367-375, doi:10.1016/S1097-2765(00)80431-1 (2000).
64 Bone, J. R. *et al.* Acetylated histone H4 on the male X chromosome is associated with dosage compensation in Drosophila. *Genes & Development* **8**, 96-104, doi:10.1101/gad.8.1.96 (1994).
65 Smith, E. R. *et al.* The drosophila MSL complex acetylates histone H4 at lysine 16, a chromatin modification linked to dosage compensation. *Mol Cell Biol* **20**, 312-318, doi:10.1128/mcb.20.1.312-318.2000 (2000).
66 Shogren-Knaak, M. *et al.* Histone H4-K16 acetylation controls chromatin structure and protein interactions. *Science* **311**, 844-847, doi:10.1126/science.1124000 (2006).
67 Taylor, G. C., Eskeland, R., Hekimoglu-Balkan, B., Pradeepa, M. M. & Bickmore, W. A. H4K16 acetylation marks active genes and enhancers of embryonic stem cells, but does not alter chromatin compaction. *Genome Res* **23**, 2053-2065, doi:10.1101/gr.155028.113 (2013).
68 Chen, E. Y. *et al.* Enrichr: interactive and collaborative HTML5 gene list enrichment analysis tool. *BMC Bioinformatics* **14**, 128-114, doi:papers3://publication/doi/10.1186/1471-2105-14-128 (2013).
69 Kuleshov, M. V. *et al.* Enrichr: a comprehensive gene set enrichment analysis web server 2016 update. *Nucleic Acids Res* **44**, W90-97, doi:papers3://publication/doi/10.1093/nar/gkw377 (2016).
70 Subramanian, A. *et al.* Gene set enrichment analysis: a knowledge-based approach for interpreting genome-wide expression profiles. *Proceedings of the National Academy of Sciences* **102**, 15545-15550, doi:papers3://publication/doi/10.1073/pnas.0506580102 (2005).

71 Fridman, A. L. & Tainsky, M. A. Critical pathways in cellular senescence and immortalization revealed by gene expression profiling. *Oncogene* **27**, 5975-5987, doi:papers3://publication/doi/10.1038/onc.2008.213 (2008).
72 Ruscetti, M. *et al.* NK cell-mediated cytotoxicity contributes to tumor control by a cytostatic drug combination. *Science* **362**, 1416-1422, doi:papers3://publication/doi/10.1126/science.aas9090 (2018).
73 Dang, W. *et al.* Histone H4 lysine 16 acetylation regulates cellular lifespan. *Nature 2018* **459**, 802-807, doi:10.1038/nature08085 (2009).
74 Faget, D. V., Ren, Q. & Stewart, S. A. Unmasking senescence: context-dependent effects of SASP in cancer. *Nat Rev Cancer* **19**, 439-453, doi:papers3://publication/doi/10.1038/s41568-019-0156-2 (2019).
75 Kuilman, T., Michaloglou, C., Mooi, W. J. & Peeper, D. S. The essence of senescence. *Genes & Development* **24**, 2463-2479, doi:papers3://publication/doi/10.1101/gad.1971610 (2010).
76 Tasdemir, N. *et al.* BRD4 Connects Enhancer Remodeling to Senescence Immune Surveillance. *Cancer Discov* **6**, 612-629, doi:10.1158/2159-8290.CD-16-0217 (2016).
77 Placke, T. *et al.* Requirement for CDK6 in MLL-rearranged acute myeloid leukemia. *Blood* **124**, 13-23, doi:papers3://publication/doi/10.1182/blood-2014-02-558114 (2014).
78 Hirai, H., Roussel, M. F., Kato, J. Y., Ashmun, R. A. & Sherr, C. J. Novel INK4 proteins, p19 and p18, are specific inhibitors of the cyclin D-dependent kinases CDK4 and CDK6. *Mol Cell Biol* **15**, 2672-2681, doi:papers3://publication/doi/10.1128/mcb.15.5.2672 (1995).
79 Fry, D. W. *et al.* Specific inhibition of cyclin-dependent kinase 4/6 by PD 0332991 and associated antitumor activity in human tumor xenografts. *Molecular Cancer Therapeutics* **3**, 1427-1437, doi:papers3://publication/uuid/E8D6C4BF-0FC6-4134-969C-C9812E9A7B32 (2004).
80 Ruscetti, M. *et al.* Senescence-Induced Vascular Remodeling Creates Therapeutic Vulnerabilities in Pancreas Cancer. *Cell* **181**, 424-441.e421, doi:papers3://publication/doi/10.1016/j.cell.2020.03.008 (2020).
81 Sherr, C. J., Beach, D. & Shapiro, G. I. Targeting CDK4 and CDK6: From Discovery to Therapy. *Cancer Discovery* **6**, 353-367, doi:papers3://publication/doi/10.1158/2159-8290.CD-15-0894 (2016).
82 Yang, C. *et al.* Acquired CDK6 amplification promotes breast cancer resistance to CDK4/6 inhibitors and loss of ER signaling and dependence. *Oncogene* **36**, 2255-2264, doi:10.1038/onc.2016.379 (2017).
83 Chen, L. *et al.* Autophagy inhibition contributes to the synergistic interaction between EGCG and doxorubicin to kill the hepatoma Hep3B cells. *PLoS ONE* **9**, e85771, doi:papers3://publication/doi/10.1371/journal.pone.0085771 (2014).
84 Kempinska, K. *et al.* Pharmacologic Inhibition of the Menin-MLL Interaction Leads to Transcriptional Repression of PEG10 and Blocks Hepatocellular Carcinoma. *Molecular Cancer Therapeutics* **17**, 26-38, doi:papers3://publication/doi/10.1158/1535-7163.MCT-17-0580 (2018).

85 Svoboda, L. K. *et al.* Menin regulates the serine biosynthetic pathway in Ewing sarcoma. *The Journal of pathology* **245**, 324-336, doi:papers3://publication/doi/10.1002/path.5085 (2018).
86 Agger, K. *et al.* UTX and JMJD3 are histone H3K27 demethylases involved in HOX gene regulation and development. *Nature 2018* **449**, 731-734, doi:10.1038/nature06145 (2007).
87 Lan, F. *et al.* A histone H3 lysine 27 demethylase regulates animal posterior development. *Nature 2018* **449**, 689-694, doi:10.1038/nature06192 (2007).
88 Lee, M. G. *et al.* Demethylation of H3K27 Regulates Polycomb Recruitment and H2A Ubiquitination. *Science* **318**, 447-450, doi:doi:10.1126/science.1149042 (2007).
89 Hong, S. *et al.* Identification of JmjC domain-containing UTX and JMJD3 as histone H3 lysine 27 demethylases. *Proceedings of the National Academy of Sciences* **104**, 18439-18444, doi:10.1073/pnas.0707292104 (2007).
90 Shi, B. *et al.* UTX condensation underlies its tumour-suppressive activity. *Nature 2018* **597**, 726-731, doi:10.1038/s41586-021-03903-7 (2021).
91 Cao, R. *et al.* Role of Histone H3 Lysine 27 Methylation in Polycomb-Group Silencing. *Science* **298**, 1039-1043, doi:doi:10.1126/science.1076997 (2002).
92 Klossowski, S. *et al.* Menin inhibitor MI-3454 induces remission in MLL1-rearranged and NPM1-mutated models of leukemia. *J Clin Invest* **130**, 981-997, doi:papers3://publication/doi/10.1172/JCI129126 (2020).
93 Qiu, H. *et al.* MEN1 deficiency leads to neuroendocrine differentiation of lung cancer and disrupts the DNA damage response. *Nat Commun* **11**, 1009, doi:10.1038/s41467-020-14614-4 (2020).
94 Karnik, S. K. *et al.* Menin regulates pancreatic islet growth by promoting histone methylation and expression of genes encoding p27Kip1 and p18INK4c. *Proceedings of the National Academy of Sciences* **102**, 14659-14664, doi:papers3://publication/doi/10.1073/pnas.0503484102 (2005).
95 Schnepp, R. W. *et al.* Menin induces apoptosis in murine embryonic fibroblasts. *J Biol Chem* **279**, 10685-10691, doi:papers3://publication/doi/10.1074/jbc.M308073200 (2004).
96 Chen, B. *et al.* Dynamic imaging of genomic loci in living human cells by an optimized CRISPR/Cas system. *Cell* **155**, 1479-1491, doi:10.1016/j.cell.2013.12.001 (2013).
97 Akama-Garren, E. H. *et al.* A Modular Assembly Platform for Rapid Generation of DNA Constructs. *Sci. Rep.* **6**, 16836-16839, doi:papers3://publication/doi/10.1038/srep16836 (2016).
98 Krivtsov, A. V. *et al.* Transformation from committed progenitor to leukaemia stem cell initiated by MLL-AF9. *Nature 2018* **442**, 818-822, doi:10.1038/nature04980 (2006).
99 Krivtsov, A. V. *et al.* Patient Derived Xenograft (PDX) Models Faithfully Recapitulate The Genetic Composition Of Primary AML. *Blood* **122**, 1328-1328, doi:10.1182/blood.V122.21.1328.1328 (2013).
100 Doench, J. G. *et al.* Optimized sgRNA design to maximize activity and minimize off-target effects of CRISPR-Cas9. *Nat Biotechnol* **34**, 184-191, doi:papers3://publication/doi/10.1038/nbt.3437 (2016).

101 Sanjana, N. E., Shalem, O. & Zhang, F. Improved vectors and genome-wide libraries for CRISPR screening. *Nat Meth* **11**, 783-784, doi:papers3://publication/doi/10.1038/nmeth.3047 (2014).
102 Phillips, R. E. *et al.* Target identification reveals lanosterol synthase as a vulnerability in glioma. *Proc Natl Acad Sci USA* **116**, 7957-7962, doi:papers3://publication/doi/10.1073/pnas.1820989116 (2019).
103 Strezoska, Ž. *et al.* Optimized PCR conditions and increased shRNA fold representation improve reproducibility of pooled shRNA screens. *PLoS ONE* **7**, e42341, doi:papers3://publication/doi/10.1371/journal.pone.0042341 (2012).
104 Li, W. *et al.* Quality control, modeling, and visualization of CRISPR screens with MAGeCK-VISPR. *Genome Biol* **16**, 281, doi:10.1186/s13059-015-0843-6 (2015).
105 Carroll, T. S., Liang, Z., Salama, R., Stark, R. & de Santiago, I. Impact of artifact removal on ChIP quality metrics in ChIP-seq and ChIP-exo data. *Front. Genet.* **5**, doi:papers3://publication/doi/10.3389/fgene.2014.00075 (2014).
106 Liao, Y., Smyth, G. K. & Shi, W. The R package Rsubread is easier, faster, cheaper and better for alignment and quantification of RNA sequencing reads. *Nucleic Acids Res* **47**, e47, doi:papers3://publication/doi/10.1093/nar/gkz114 (2019).
107 Zhang, Y. *et al.* Model-based analysis of ChIP-Seq (MACS). *Genome Biol* **9**, R137-139, doi:papers3://publication/doi/10.1186/gb-2008-9-9-r137 (2008).
108 Nikolayeva, O. & Robinson, M. D. edgeR for differential RNA-seq and ChIP-seq analysis: an application to stem cell biology. *Methods Mol. Biol.* **1150**, 45-79, doi:papers3://publication/doi/10.1007/978-1-4939-0512-6_3 (2014).
109 Yu, G., Wang, L.-G. & He, Q.-Y. ChIPseeker: an R/Bioconductor package for ChIP peak annotation, comparison and visualization. *Bioinformatics* **31**, 2382-2383, doi:papers3://publication/doi/10.1093/bioinformatics/btv145 (2015).
110 Ramírez, F., Dündar, F., Diehl, S., Grüning, B. A. & Manke, T. deepTools: a flexible platform for exploring deep-sequencing data. *Nucleic Acids Res* **42**, W187-191, doi:papers3://publication/doi/10.1093/nar/gku365 (2014).
111 Shen, L., Shao, N., Liu, X. & Nestler, E. ngs.plot: Quick mining and visualization of next-generation sequencing data by integrating genomic databases. *BMC Genomics* **15**, 284-214, doi:papers3://publication/doi/10.1186/1471-2164-15-284 (2014).
112 Zhu, L. J. *et al.* ChIPpeakAnno: a Bioconductor package to annotate ChIP-seq and ChIP-chip data. *BMC Bioinformatics* **11**, 10, doi:papers3://publication/doi/10.1186/1471-2105-11-237 (2010).
113 Amemiya, H. M., Kundaje, A. & Boyle, A. P. The ENCODE Blacklist: Identification of Problematic Regions of the Genome. *Sci. Rep.* **9**, 9354-9355, doi:papers3://publication/doi/10.1038/s41598-019-45839-z (2019).
114 Love, M. I., Huber, W. & Anders, S. Moderated estimation of fold change and dispersion for RNA-seq data with DESeq2. *Genome Biol* **15**, 550, doi:papers3://publication/doi/10.1186/s13059-014-0550-8 (2014).
115 Patro, R., Duggal, G., Love, M. I., Irizarry, R. A. & Kingsford, C. Salmon provides fast and bias-aware quantification of transcript expression. *Nat Meth* **14**, 417-419, doi:papers3://publication/doi/10.1038/nmeth.4197 (2017).

116 Soneson, C., Love, M. I. & Robinson, M. D. Differential analyses for RNA-seq: transcript-level estimates improve gene-level inferences. *F1000Research* **4**, 1521, doi:papers3://publication/doi/10.12688/f1000research.7563.2 (2015).

FIGURE 1 - CRISPR screens uncover functional interplay between the mammalian MLL1/2 and MLL3/4 chromatin modifying complexes

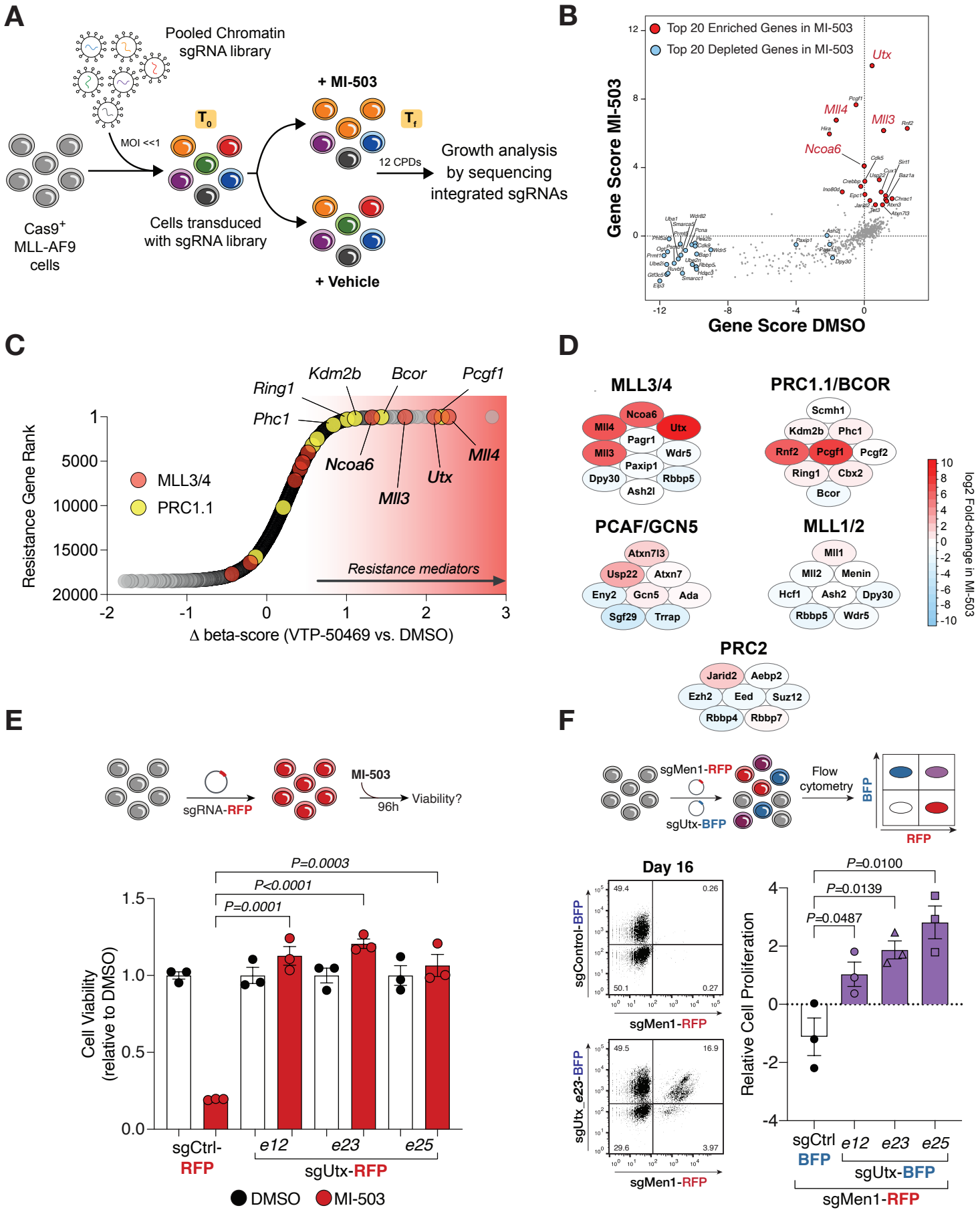

FIGURE 2 - MLL1-Menin complex and NF-Y restrict chromatin occupancy of MLL3/4-UTX at promoter regions

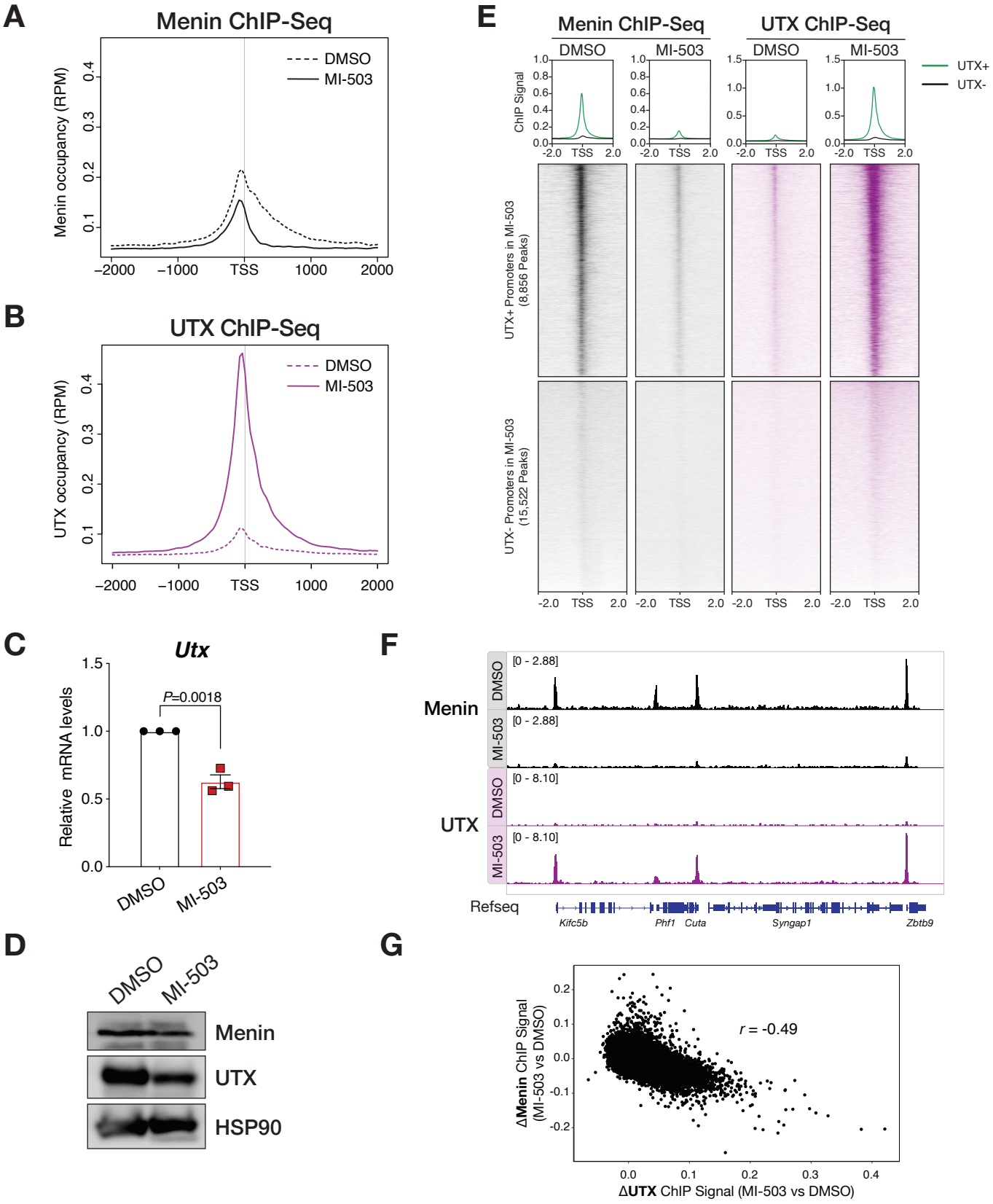

FIGURE 3 - Transcriptional co-regulation of tumor suppressive pathways by Menin and UTX

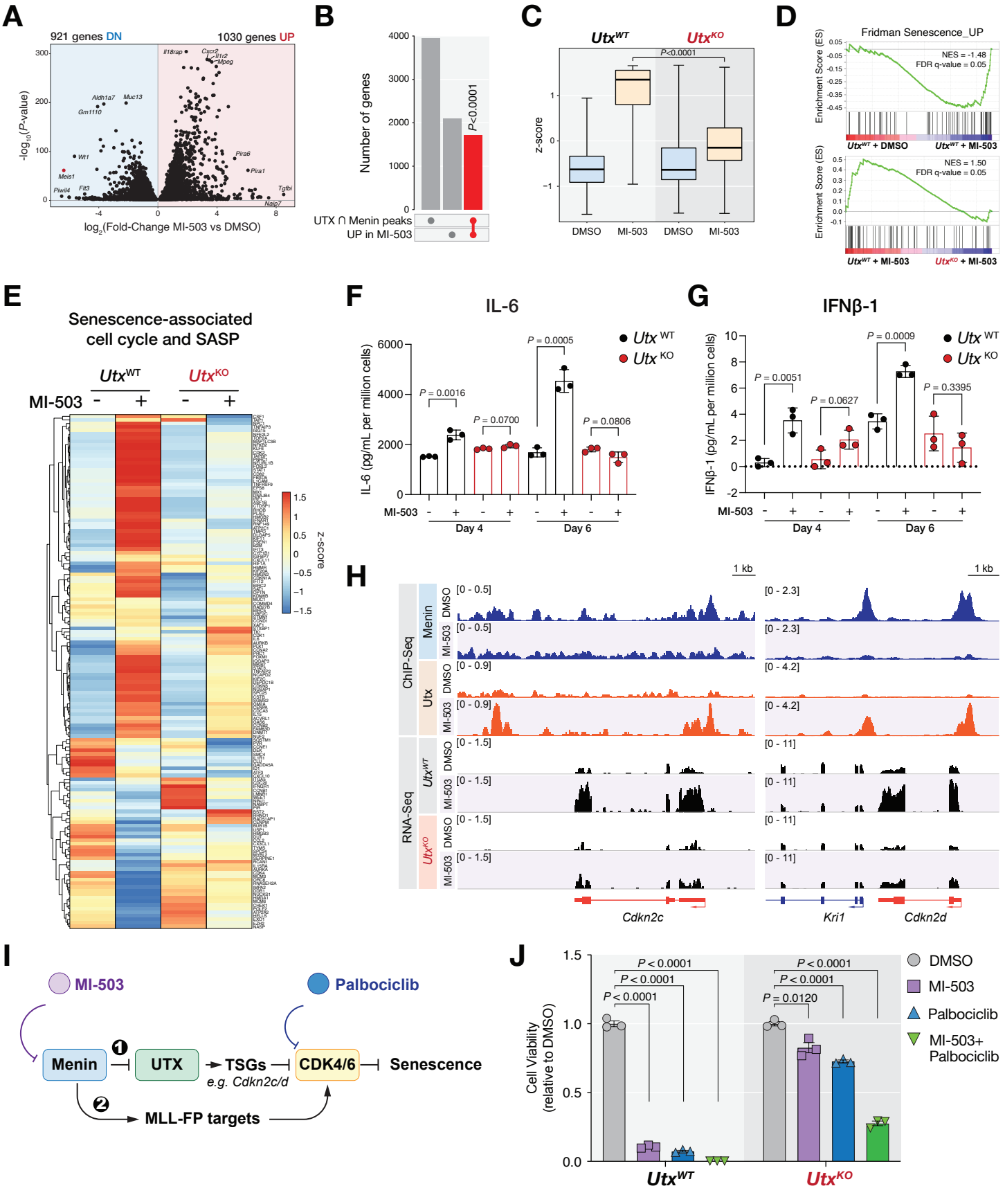

FIGURE 4 - Catalytic activity of UTX is not required to elicit UTX-dependent cellular and transcriptional functions

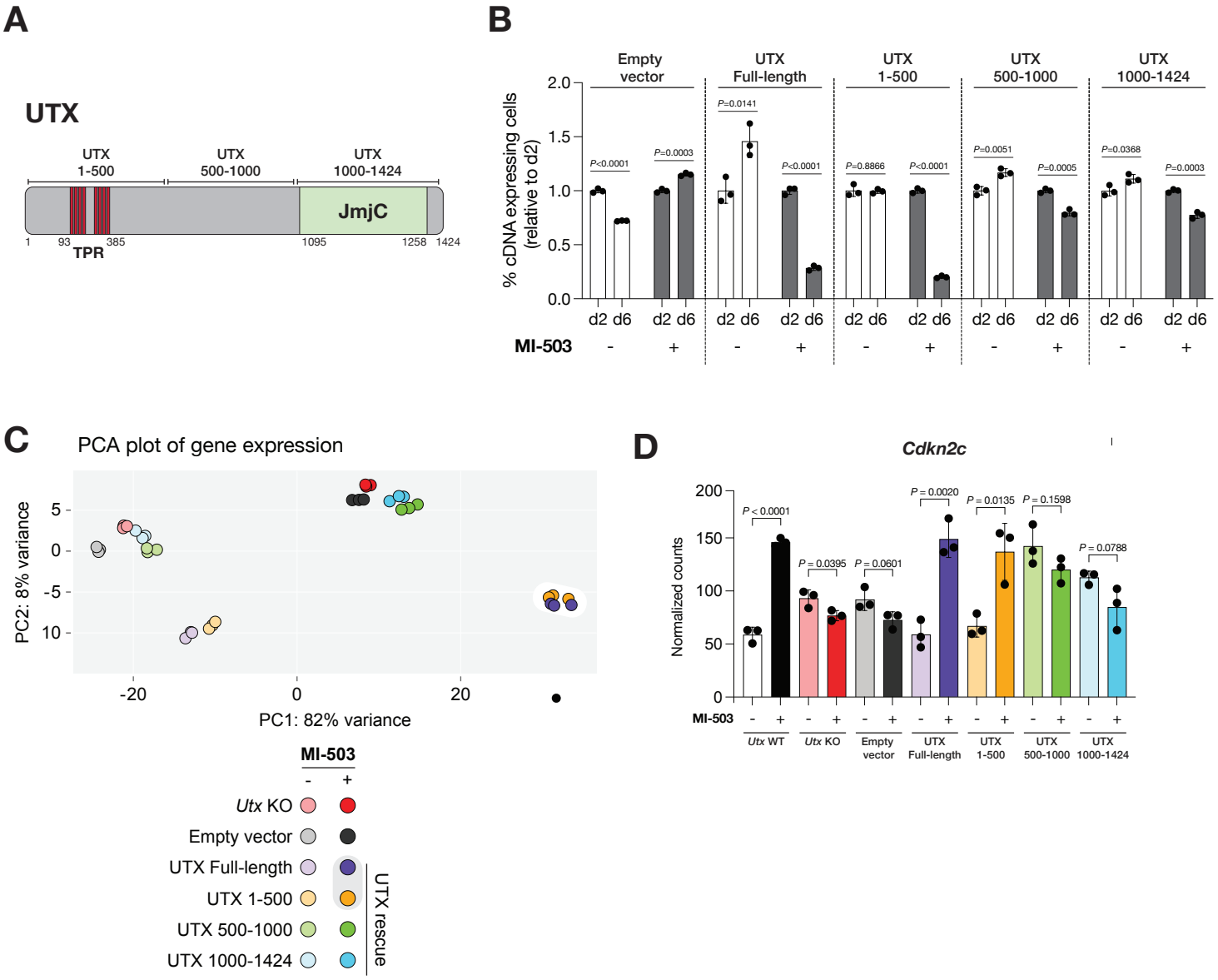

FIGURE 5 - *In vivo* response to Menin-MLL inhibition is accompanied by induction of MLL3/4-UTX-dependent tumor suppressive programs

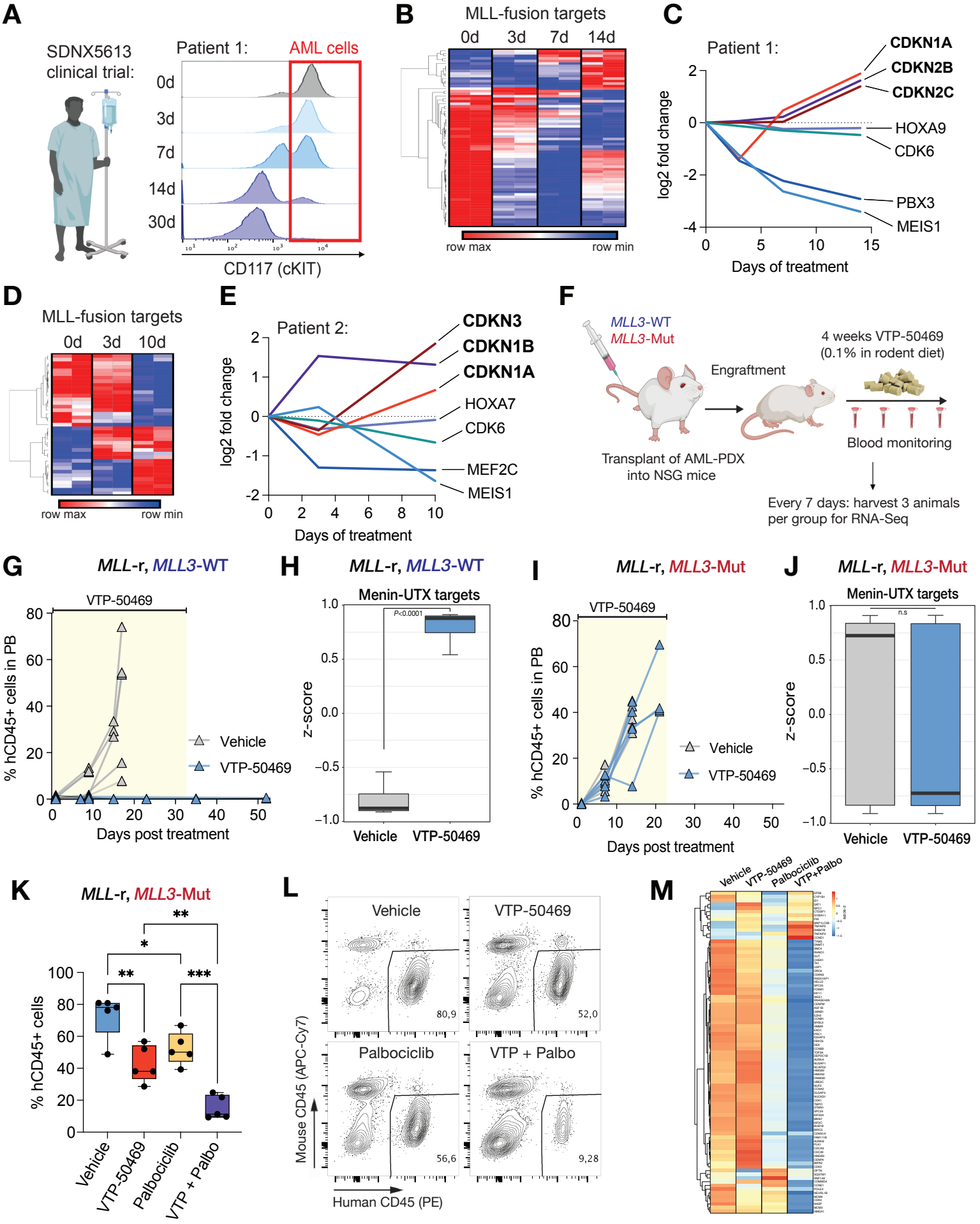

FIGURE 6 - Molecular switch between the mammalian MLL complexes dictates cellular response to Menin-MLL inhibition

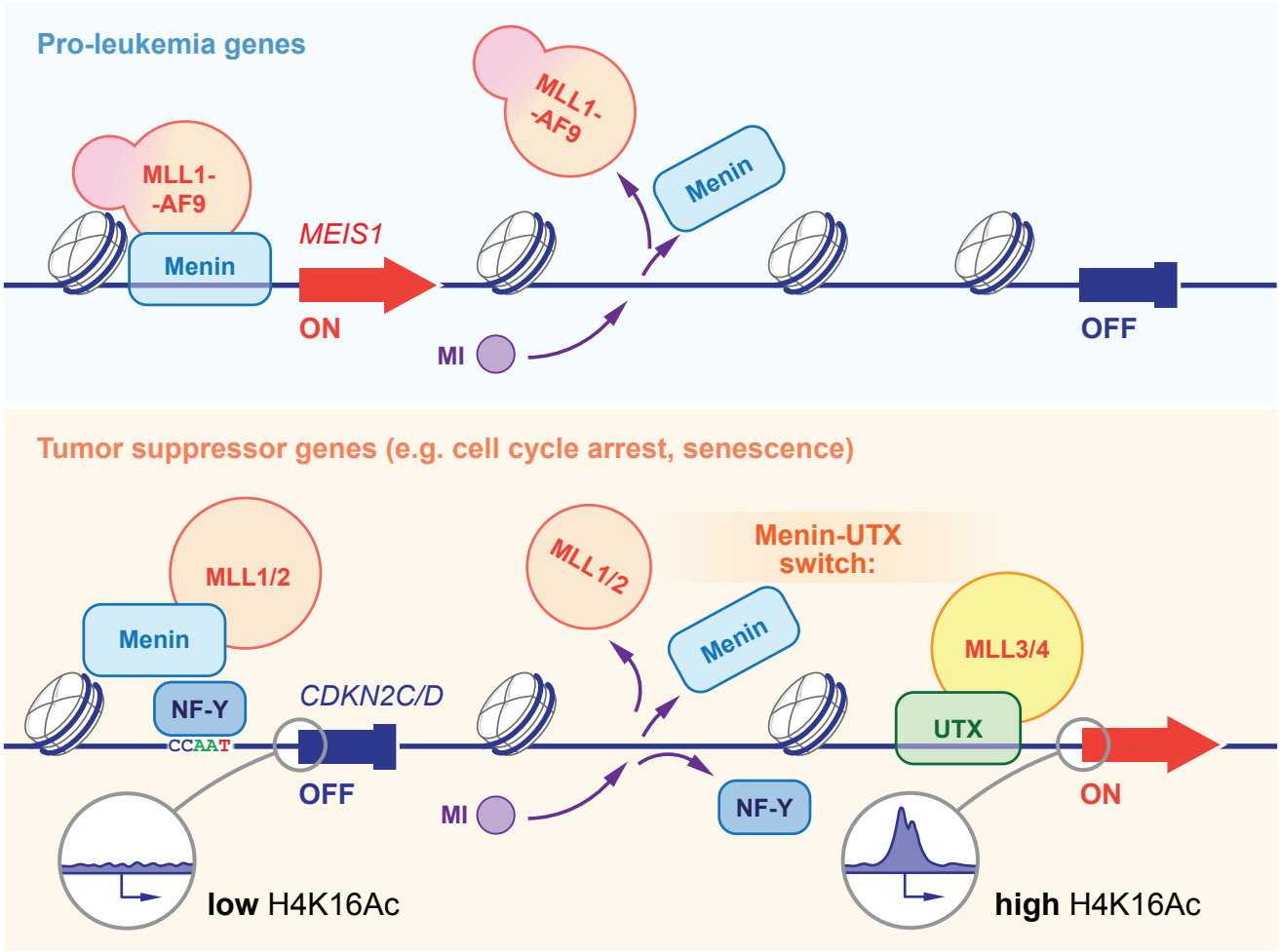

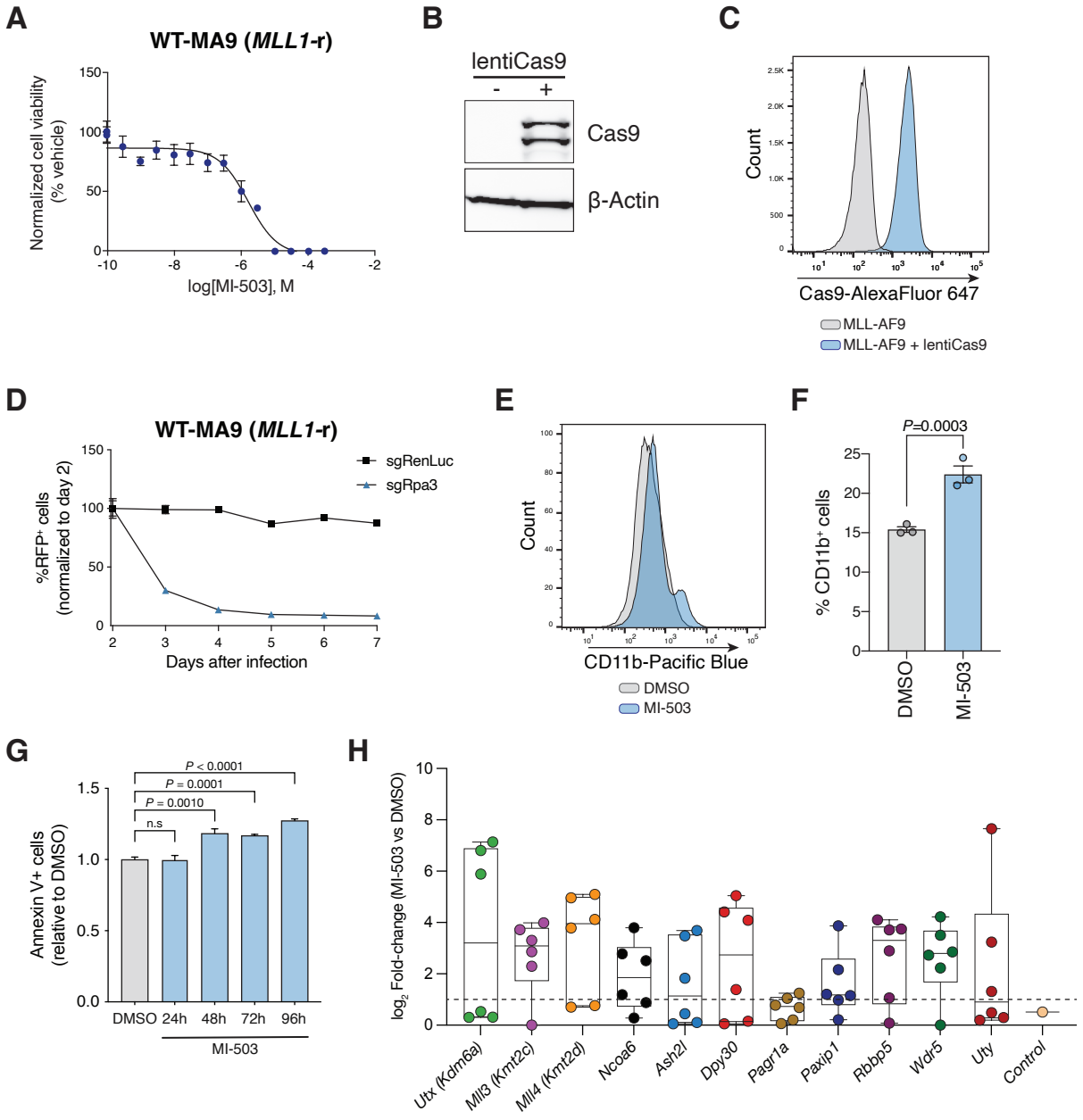

Extended Data Figure 1. Generation and characterization of Cas9-expressing mouse MLL-AF9 leukemia cells. (A) Dose response curve analysis of mouse MLL-AF9 leukemia (WT-MA9) cells treated with DMSO (vehicle) or MI-503 (Menin inhibitor) for 96 hours (mean±SEM, n=3 replicates). **(B)** Immunoblot analysis of Cas9-expressing mouse MLL-AF9 leukemia cells. **(C)** Distribution of Cas9-expressing MLL-AF9 leukemia cells determined by intracellular staining of Cas9 and flow cytometry. **(D)** Growth competition assay to determine enzymatic activity of Cas9 in mouse MLL-AF9 leukemia cells (mean±SEM, n=3 replicates). **(E)** CD11b cell surface expression measured by flow cytometry after DMSO (grey) or MI-503 (blue) treatment of MLL-AF9 leukemia cells for 96 hours. **(F)** Quantification of %CD11b positive cells after DMSO or MI-503 treatment for 96 hours (mean±SEM, n=3 replicates, P-value calculated by Student's t-test). **(G)** Quantification of %Annexin V positive cells after DMSO or MI-503 treatment at different time points (mean±SEM, n=3 replicates, *P*-value calculated by Student's t-test). **(H)** $\log_2$-fold change of individual sgRNAs from MI-503-treated vs DMSO-treated CRISPR screens in mouse MLL-AF9 leukemia cells.

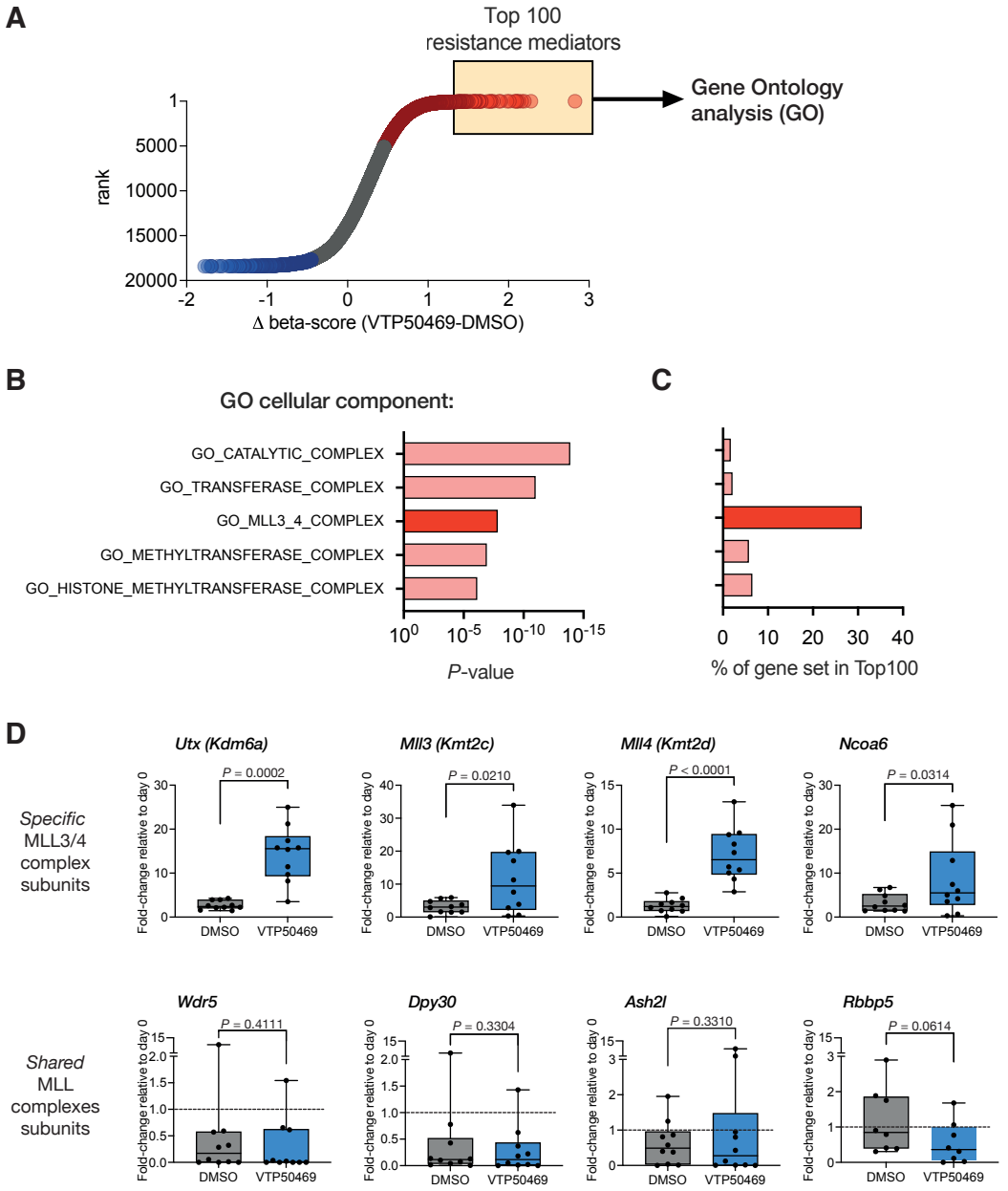

Extended Data Figure 2. Genome-wide CRISPR screening identifies the MLL3/4-UTX complex as a determinant of response to Menin-MLL inhibition. (A) Genome-wide screening data showing gene-level ranking based on differential enrichment of sgRNAs under Menin-MLL inhibitor treatment (VTP-50469) relative to vehicle (DMSO). Differential (Δ) beta-score between VTP-50469 and DMSO conditions was calculated using MaGeCK. A positive Δ beta-score denotes enrichment of specific gene-targeting sgRNAs. A negative Δ beta-score denotes depletion of specific gene-targeting sgRNAs. Red circles denote genes represented by enriched sgRNAs (genes whose inactivation promotes resistance to Menin-MLL inhibition). Blue circles denote genes represented by depleted sgRNAs (genes whose inactivation promotes sensitivity to Menin-MLL inhibition). The top 100 candidate mediators of resistance were selected for gene ontology (GO) analysis. **(B)** Top-scoring GO categories based on *P*-values obtained from GO analysis. **(C)** Percentage of genes within a given gene set that scored among the top 100 candidate mediators of resistance. **(D)** Fold-change of individual sgRNAs relative to T0 from either VTP-50469-treated or DMSO-treated cells (*P*-value calculated by Student's t-test).

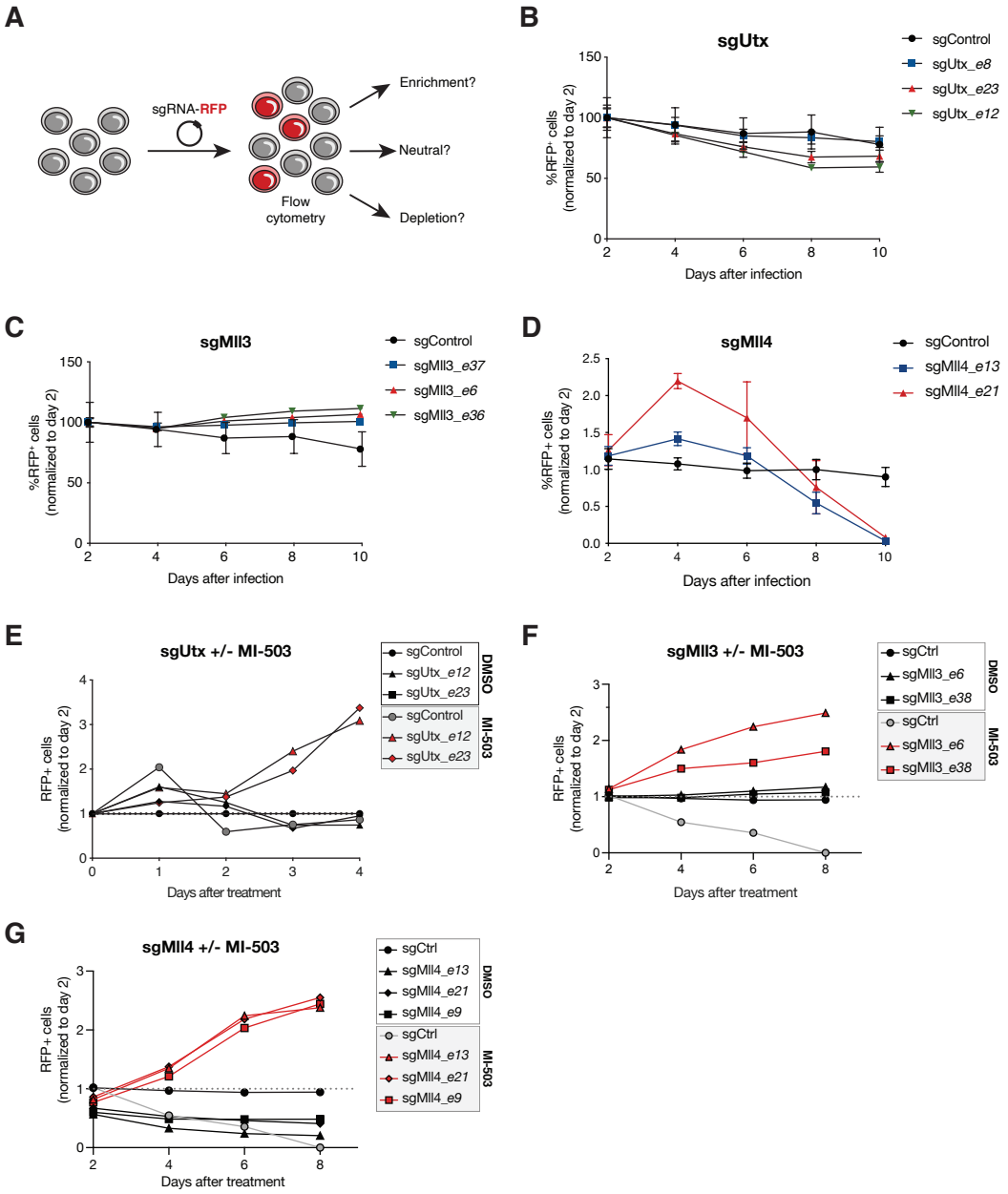

Extended Data Figure 3. MLL3/4-UTX complex dictates therapeutic outcome of Menin-MLL inhibition. (A) Layout of growth competition assay to assess the effect of genetic loss of *Utx*, *Mll3*, or *Mll4* in MLL-AF9 leukemia cells in response to Menin-MLL inhibition. **(B)** Growth competition assay in mouse MLL-AF9 (WT-MA9) cells. Graph shows the relative growth of cells infected with RFP-tagged *Utx* (*Kdm6a*) sgRNAs measured by flow cytometry (mean±SEM, n=3 infection replicates). sgControl targets a non-genic region in chromosome 8 as negative control. **(C)** Growth competition assay in mouse MLL-AF9 (WT-MA9) cells. Graph shows the relative growth of cells infected with RFP-tagged *Mll3* (*Kmt2c*) sgRNAs measured by flow cytometry (mean±SEM, n=3 infection replicates). **(D)** Growth competition assay in mouse MLL-AF9 (WT-MA9) cells. Graph shows the relative growth of cells infected with RFP-tagged *Mll4* (*Kmt2d*) sgRNAs measured by flow cytometry (mean±SEM, n=3 infection replicates). **(E)** Relative percentage of sgUtx-expressing (RFP+) cells over time after transduction of MLL-AF9 cells treated with MI-503 or DMSO. **(F)** Relative percentage of sgMll3-expressing (RFP+) cells over time after transduction of MLL-AF9 cells treated with MI-503 or DMSO. **(G)** Relative percentage of sgMll4-expressing (RFP+) cells over time after transduction of MLL-AF9 cells treated with MI-503 or DMSO.

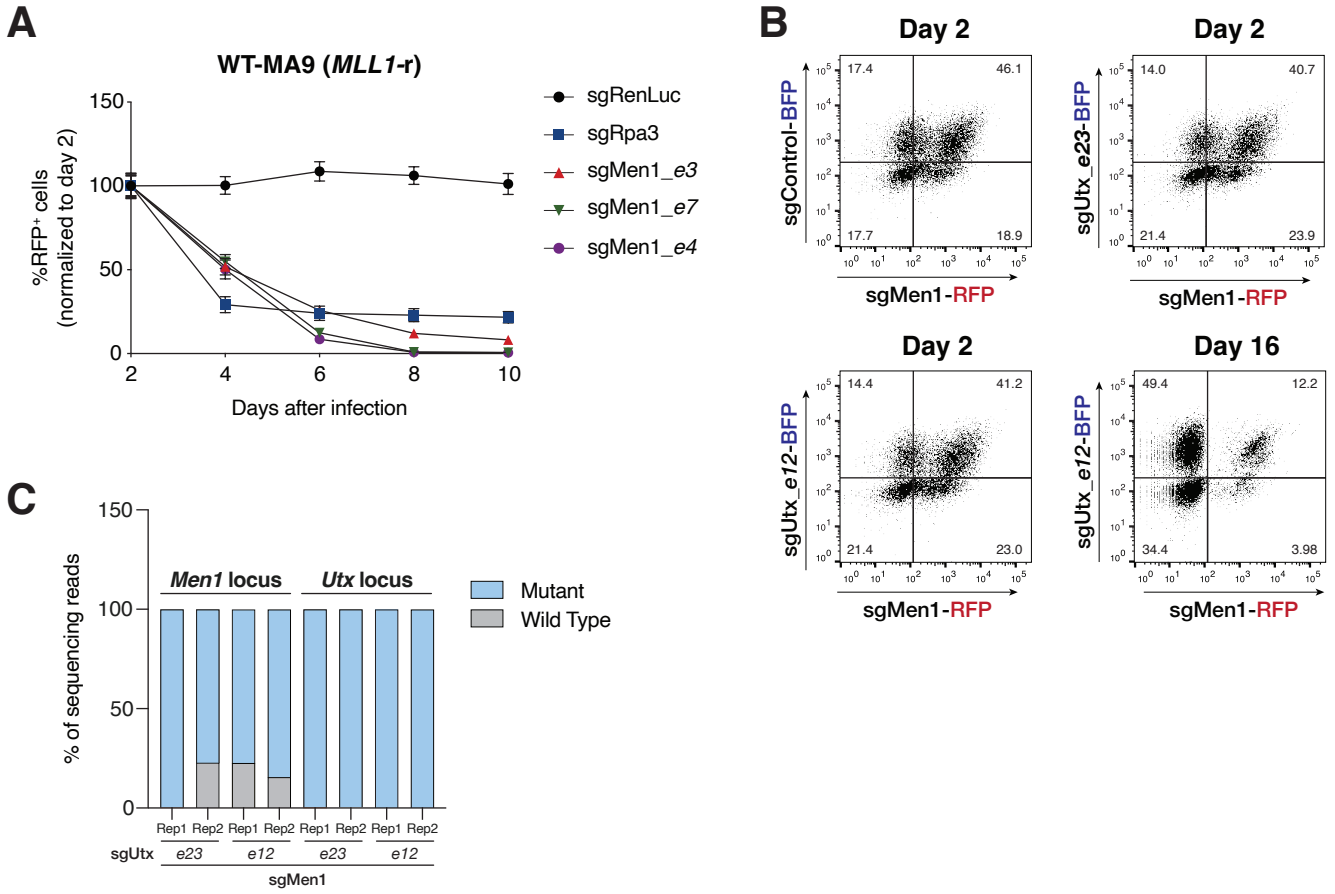

Extended Data Figure 4. *Utx* deletion rescues the lethality associated with *Men1* deletion. (A) Growth competition assay in mouse MLL-AF9 (WT-MA9) cells. Graph shows the relative growth of cells infected with RFP-tagged *Men1* sgRNAs measured by flow cytometry (mean±SEM, n=3 infection replicates). sgRenilla Luciferase (RenLuc) and sgRpa3 were negative and positive controls, respectively. **(B)** Plots from flow cytometry analysis of leukemia cells co-expressing sgMen1-RFP and sgUtx-BFP (*e12* and *e23*) 2 and 16 days post-infection. **(C)** Amplicon sequencing results of the mouse *Men1* and *Utx* loci from leukemia cells co-expressing sgMen1 and sgUtx (*e12* and *e23*). R1 and R2 represent two infection replicates for each genotype.

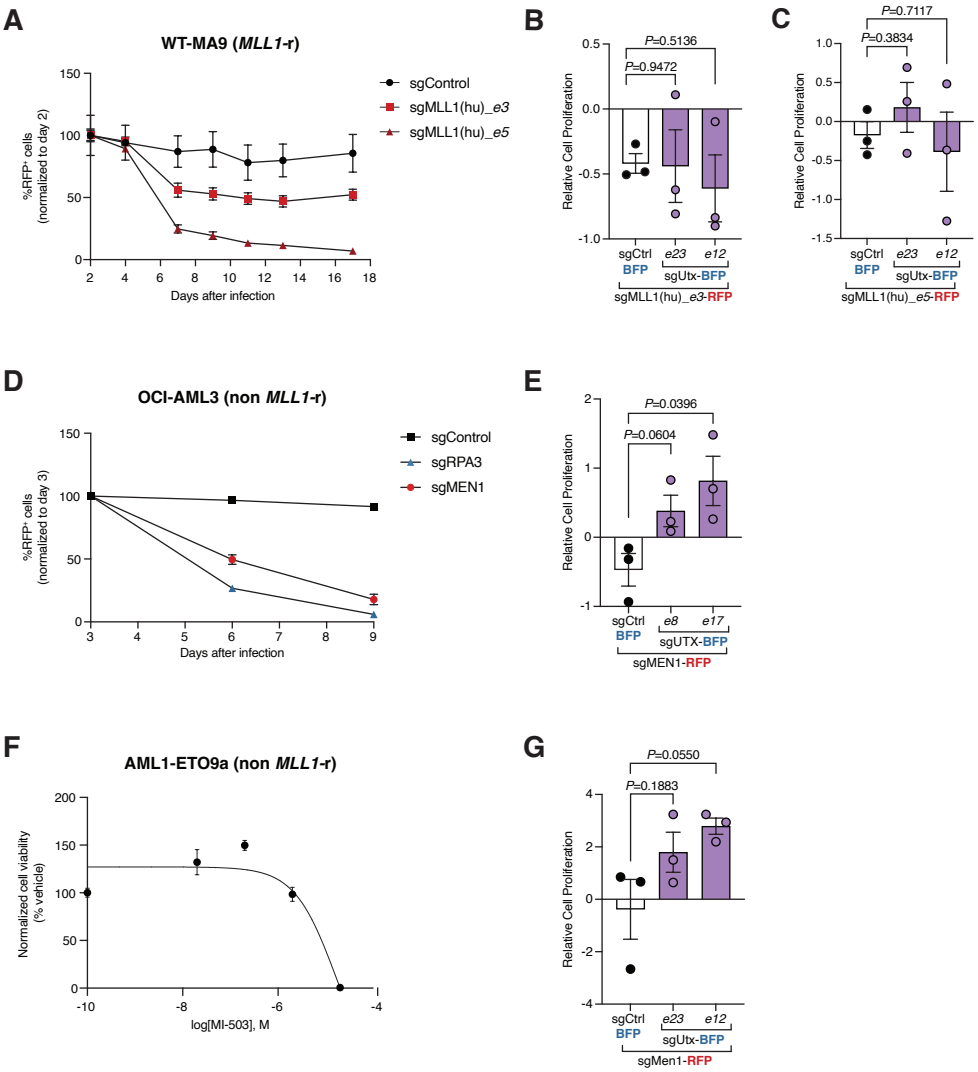

Extended Data Figure 5. Men1 and Utx epistasis is independent of the MLL-fusion. (A) Growth competition assay in mouse MLL-AF9 (WT-MA9) cells. Graph shows the relative growth of cells infected with RFP-tagged human (hu) *MLL1* (*e3* = exon 3, *e5* = exon 5) sgRNAs measured by flow cytometry (mean±SEM, n=3 infection replicates). **(B)** Differential fitness of mouse WT-MA9 cells is shown as the relative fitness of double positive cells (sgMLL1(hu)_*e3*-RFP + sgUtx-BFP or sgMLL1(hu)_*e3*-RFP + sgControl-BFP) to single positive cells (sgMLL1(hu)_*e3*-RFP) 16 days post-infection measured by flow cytometry (mean±SEM, n=3 infection replicates, *P*-value calculated by Student's t-test). **(C)** Differential fitness of mouse WT-MA9 cells is shown as the relative fitness of double positive cells (sgMLL1(hu)_*e5*-RFP + sgUtx-BFP or sgMLL1(hu)_*e5*-RFP + sgControl-BFP) to single positive cells (sgMLL1(hu)_e5-RFP) 16 days post-infection measured by flow cytometry (mean±SEM, n=3 infection replicates, *P*-value calculated by Student's t-test). **(D)** Growth competition assay in human non *MLL1*-r (OCI-AML3) cells. Graph shows the relative growth of cells infected with RFP-tagged sgRNAs measured by flow cytometry (mean±SEM, n=3 infection replicates). **(E)** Differential fitness of human OCI-AML3 cells is shown as the relative fitness of double positive cells to single positive cells 20 days post-infection measured by flow cytometry (mean±SEM, n=3 infection replicates, *P*-value calculated by Student's t-test). **(F)** Viability of mouse AML1-ETO9a leukemia cells treated with MI-503 for 96 hours. **(G)** Differential fitness of mouse AML1-ETO9a leukemia cells is shown as the relative fitness of double positive cells to single positive cells 15 days post-infection measured by flow cytometry (mean±SEM, n=3 infection replicates, *P*-value calculated by Student's t-test).

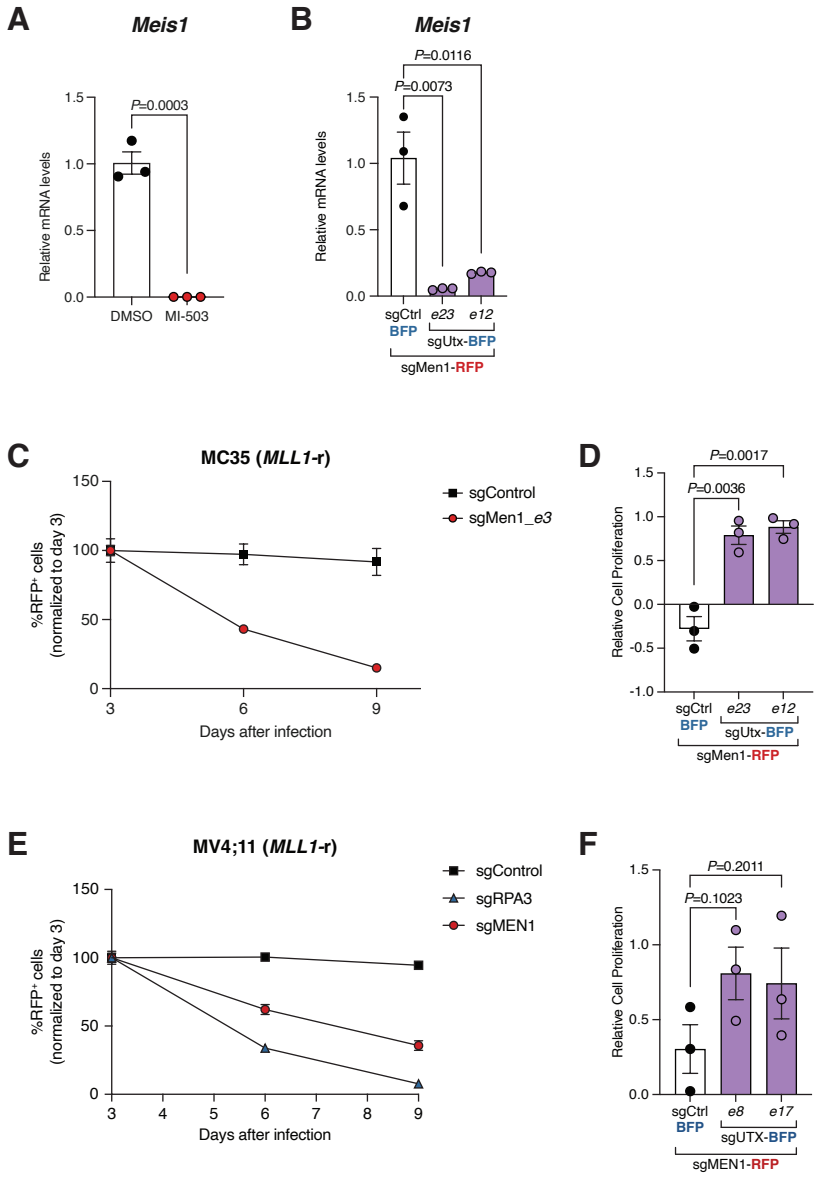

Extended Data Figure 6. *Meis1* expression is dispensable for proliferation of *Men1*^{KO};*Utx*^{KO} double-knockout MLL-AF9 leukemia cells. (A) qPCR analysis for *Meis1* expression in mouse MLL-AF9 leukemia cells treated with DMSO (vehicle) or MI-503 for 96 hours (mean±SEM, n=3 replicates, *P*-value calculated by Student's t-test). **(B)** qPCR analysis for *Meis1* expression in mouse MLL-AF9 leukemia cells co-expressing sgMen1-RFP and sgUtx-BFP, or a control sgRNA (mean±SEM, n=3 replicates, *P*-value calculated by Student's t-test). **(C)** Growth competition assay in mouse MLL-AF9 (MC35) cells. Graph shows the relative growth of cells infected with RFP-tagged sgRNAs (sgControl and sgMen1_*e3*) measured by flow cytometry (mean±SEM, n=3 infection replicates). **(D)** Differential fitness of mouse MC35 cells is shown as the relative fitness of double positive cells (sgMen1-RFP + sgUtx-BFP or sgMen1-RFP + sgControl-BFP) to single positive cells (sgMen1-RFP) 9 days post-infection measured by flow cytometry (mean±SEM, n=3 infection replicates, *P*-value calculated by Student's t-test). **(E)** Growth competition assay in human MLL-AF4 (MV4;11) leukemia cells. Graph shows the relative growth of cells infected with RFP-tagged sgRNAs measured by flow cytometry (mean±SEM, n=3 infection replicates). **(F)** Differential fitness of human MV4;11 leukemia cells is shown as the relative fitness of double positive cells to single positive cells 20 days post-infection measured by flow cytometry (mean±SEM, n=3 infection replicates, *P*-value calculated by Student's t-test).

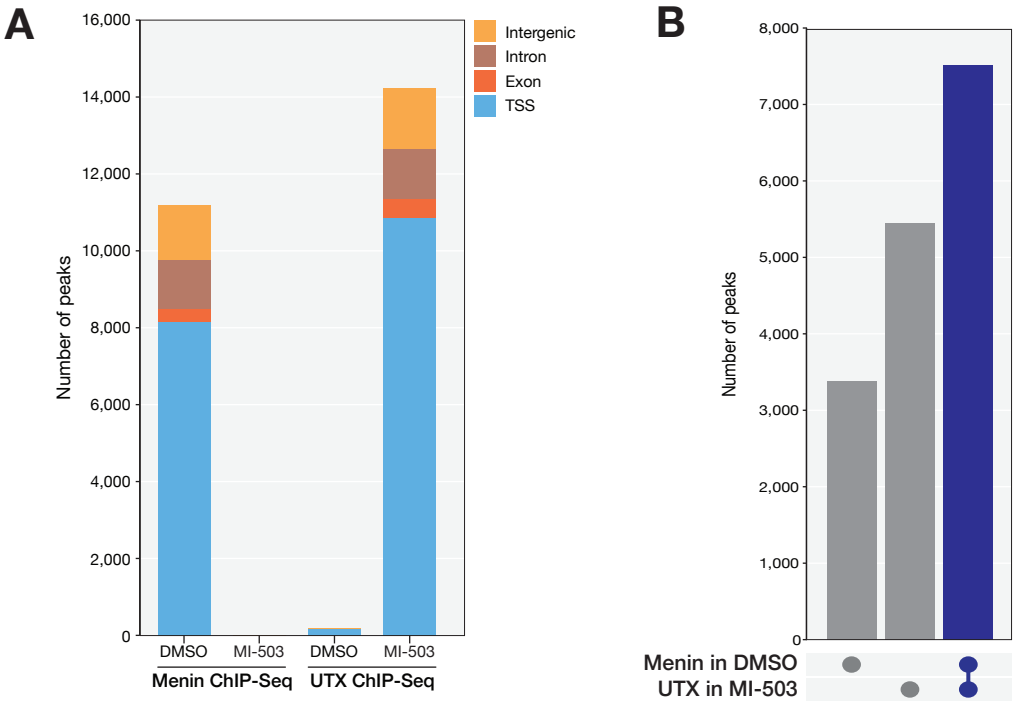

Extended Data Figure 7. Genomic distribution of Menin and UTX is different in the context of MI-503 treatment. (A) Genomic distribution of Menin and UTX ChIP-Seq peaks from mouse leukemia cells treated with DMSO or MI-503 for 96 hours. **(B)** Upset plot showing a comparison between the genomic distribution of Menin ChIP-Seq peaks in DMSO (grey), genomic distribution of UTX ChIP-Seq peaks in MI-503 (grey), and the overlap between UTX ChIP-Seq peaks in MI-503 and Menin ChIP-Seq peaks in DMSO (blue).

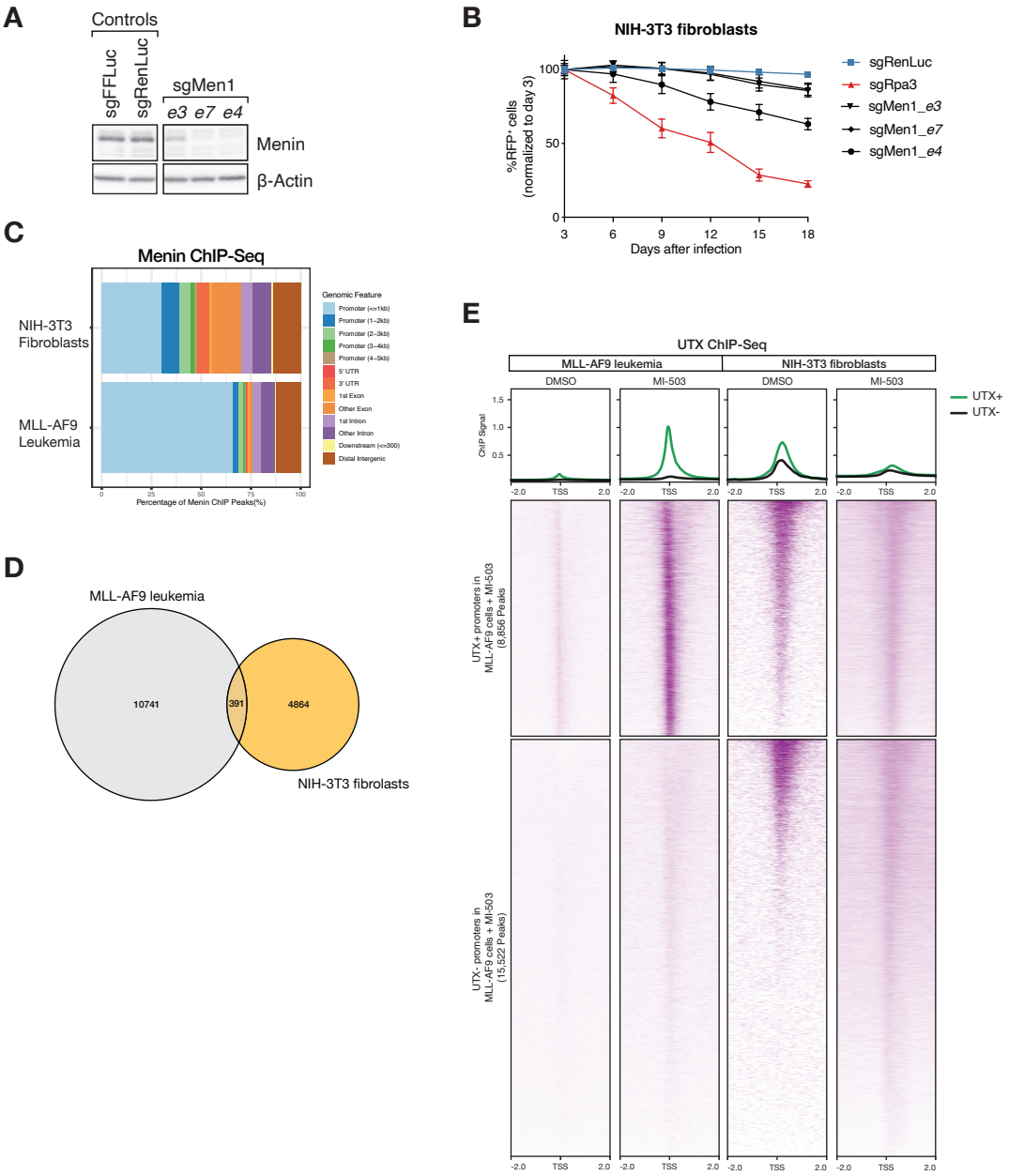

Extended Data Figure 8. Menin-independent mammalian cells do not exhibit chromatin changes associated with the Menin-UTX molecular switch. (A) Immunoblot analysis of Cas9-expressing mouse fibroblast (NIH-3T3) cells expressing different controls and *Men1* sgRNAs. **(B)** Growth competition assay in mouse fibroblast cells. Graph shows the relative growth of cells infected with RFP-tagged sgRNAs measured by flow cytometry (mean±SEM, n=3 infection replicates). **(C)** Genomic distribution of Menin ChIP-Seq peaks from mouse fibroblasts (top) or mouse MLL-AF9 leukemia cells (bottom). **(D)** Venn diagram comparing the number of Menin peaks detected in mouse MLL-AF9 leukemia cells (grey) versus NIH-3T3 fibroblasts (yellow). **(E)** Heatmaps displaying UTX ChIP-Seq signals mapping to a 4-kb window around TSSs. Data is shown for mouse MLL-AF9 cells (left) and NIH-3T3 mouse fibroblasts (right) treated with DMSO or MI-503 for 96 hours. Metaplot represents the average ChIP-Seq signal for UTX at promoters that are bound by UTX (green) or not (black) in MLL-AF9 cells treated with MI-503.

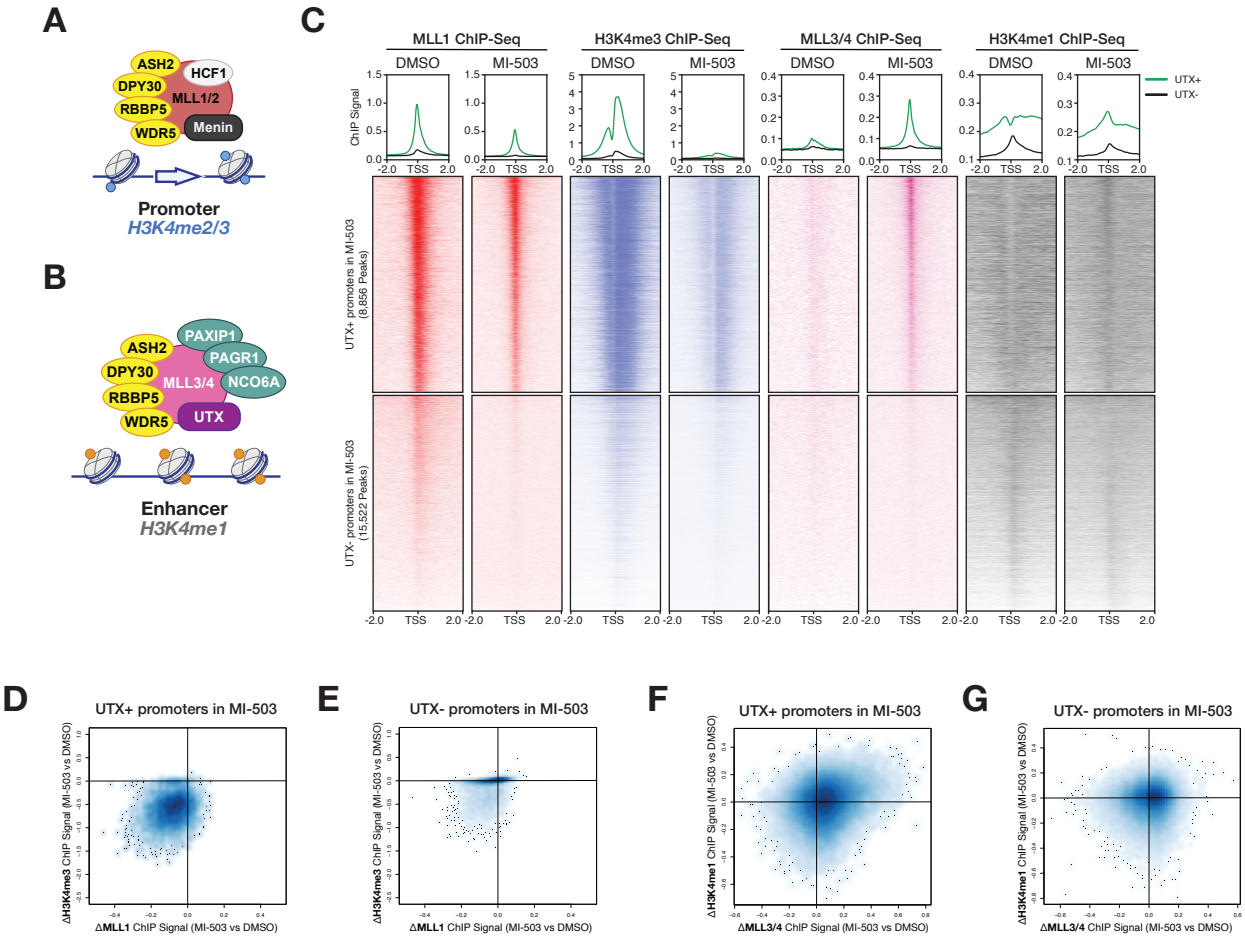

Extended Data Figure 9. Disruption of Menin-MLL1 leads to targeting of MLL3/4-UTX to sites normally bound by the MLL1-Menin complex. (A) Schematic representation of the mammalian MLL1 and MLL2 histone methyltransferase complexes. Highlighted in red is the enzymatic subunit of the complex (MLL1 and MLL2 are mutually exclusive). Yellow denotes shared subunits with the MLL3/4 complex. **(B)** Schematic representation of the mammalian MLL3 and MLL4 histone methyltransferase complexes. Highlighted in pink and purple are the enzymatic subunits of the complex (MLL3 and MLL4 are mutually exclusive). Yellow denotes shared subunits with the MLL1/2 complex. Green denotes non-enzymatic subunits of the MLL3/4 complex. **(C)** Heatmaps displaying MLL1 (red) and H3K4me3 (blue) ChIP-Seq signals mapping to a 4-kb window around TSSs. Data is shown for DMSO and MI-503-treated cells for 96 hours. Metaplot represents the average ChIP-Seq signal for each protein at promoters that are UTX+ (green) or UTX- (black). Heatmaps displaying MLL3/4 (pink) and H3K4me1 (grey) ChIP-Seq signals mapping to a 4-kb window around TSSs. Data is shown for DMSO and MI-503-treated cells for 96 hours. Metaplot represents the average ChIP-Seq signal for each protein at promoters that are UTX+ (green) or UTX- (black). **(D)** Density plot showing correlation between H3K4me3 and MLL1 ChIP-Seq signals (MI-503 vs DMSO). Signals correspond to summed signal ±2kb around TSSs that overlap with UTX peaks in MI-503 condition. **(E)** Density plot showing correlation between H3K4me3 and MLL1 ChIP-Seq signals (MI-503 vs DMSO). Signals correspond to summed signal ±2kb around TSSs that do not overlap with UTX peaks in MI-503 condition. **(F)** Density plot showing correlation between H3K4me1 and MLL3/4 ChIP-Seq signals (MI-503 vs DMSO). Signals correspond to summed signal ±2kb around TSSs that overlap with UTX peaks in MI-503 condition. **(G)** Density plot showing correlation between H3K4me1 and MLL3/4 ChIP-Seq signals (MI-503 vs DMSO). Signals correspond to summed signal ±2kb around TSSs that do not overlap with UTX peaks in MI-503 condition.

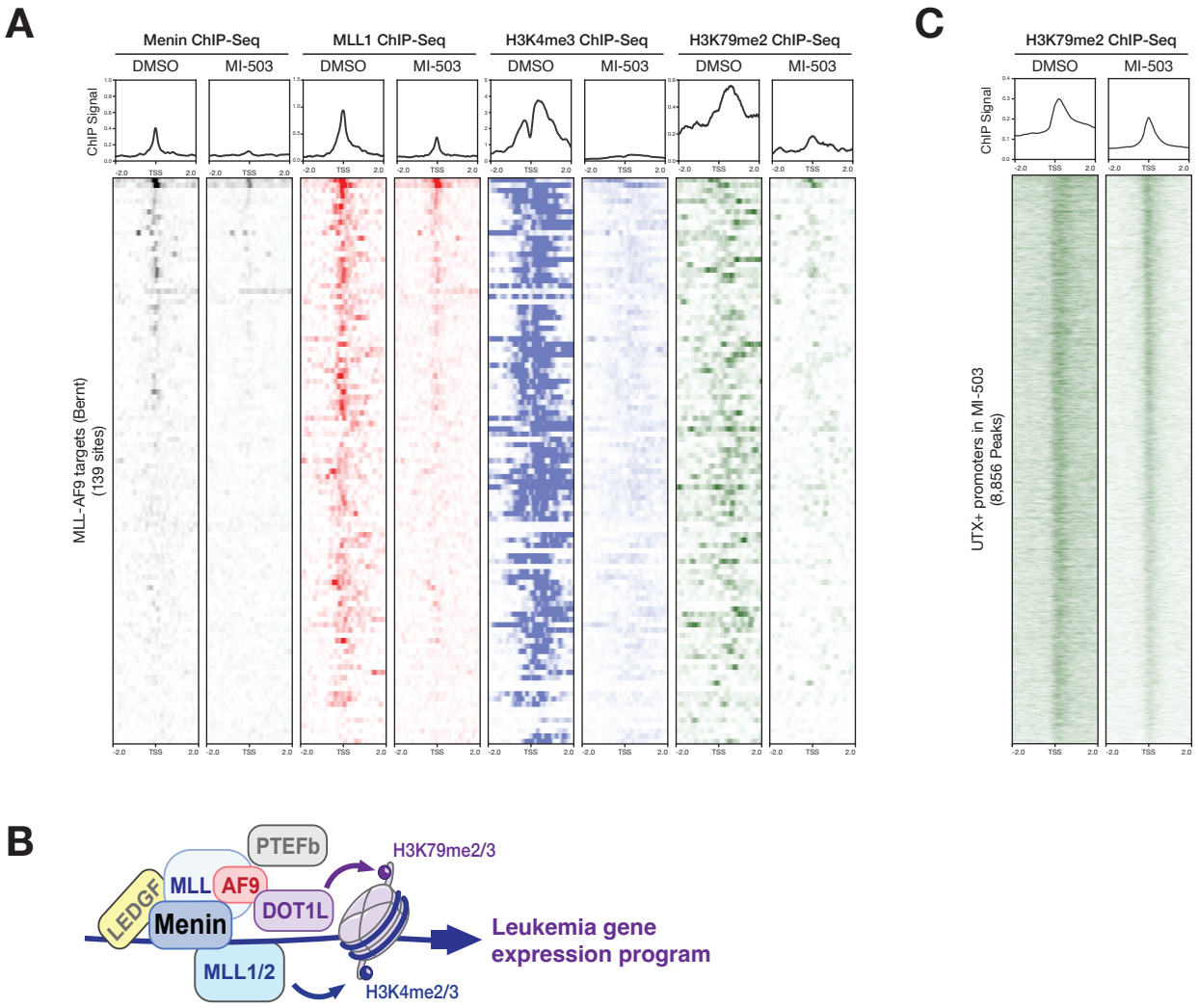

Extended Data Figure 10. MLL1-Menin targets are distinct genomic loci from MLL-FP targets. **(A)** Heatmaps displaying Menin (black), MLL1 (red), H3K4me3 (blue), and H3K79me2 (green) ChIP-Seq signals mapping to MLL-AF9 target loci (139 sites) from MLL-AF9 leukemia cells treated with DMSO or MI-503 for 96 hours. Metaplot represents the average ChIP-Seq signal for each protein at promoters. **(B)** Schematic representation of ectopic chromatin complexes that are formed by MLL-FPs. **(C)** Heatmaps displaying H3K79me2 ChIP-Seq signals mapping to a 4-kb window around TSSs in MLL-AF9 leukemia cells treated with DMSO or MI-503 for 96 hours. Metaplot represents the average ChIP-Seq signal for H3K79me2 at promoters that are bound by UTX in MLL-AF9 cells treated with MI-503.

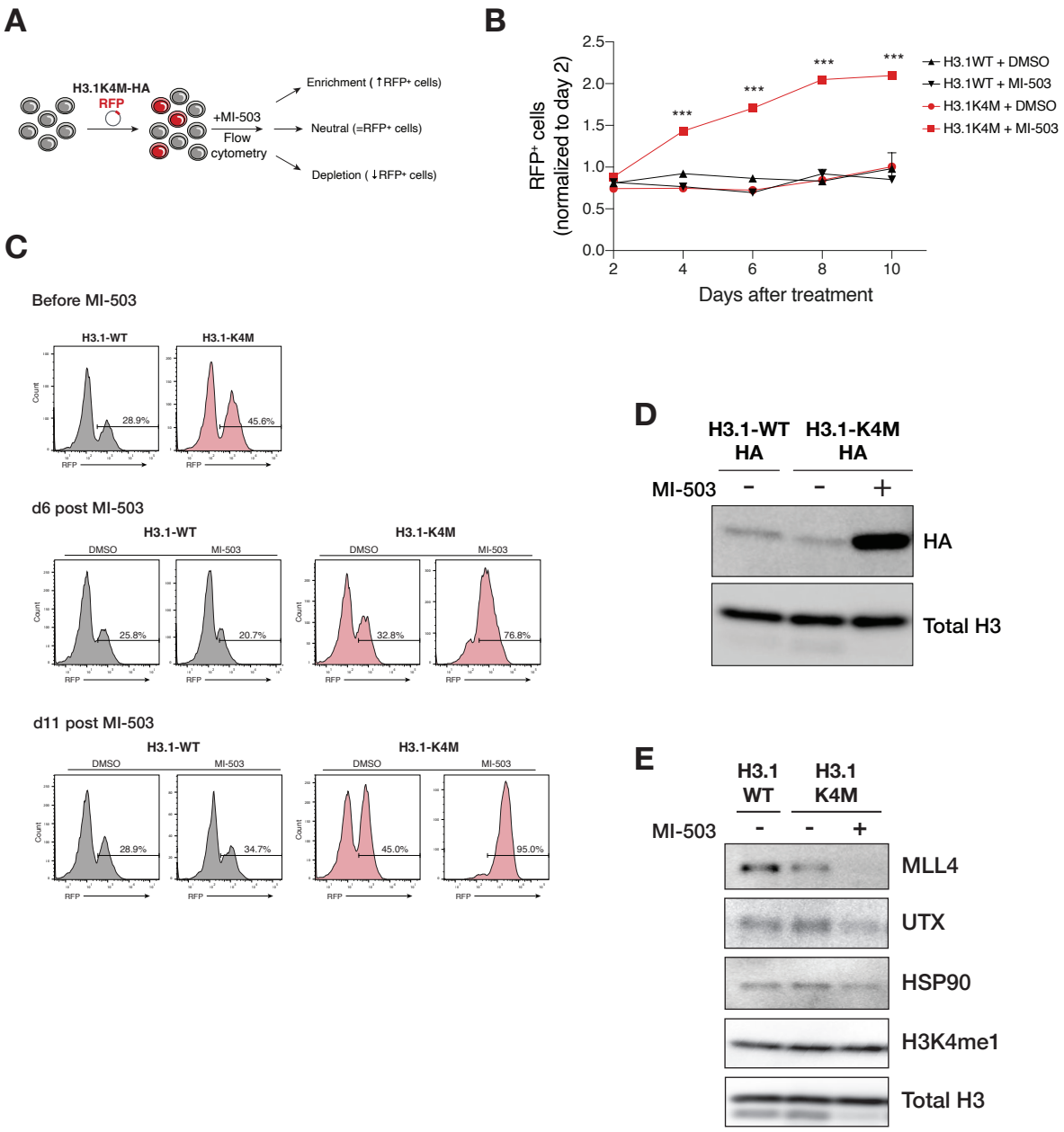

Extended Data Figure 11. Destabilization of the MLL3/4-UTX complex is sufficient to blunt cellular responses to Menin-MLL inhibition. (A) Layout of growth competition assay to assess the effects of expressing a H3.1K4M mutation in MLL-AF9 leukemia cells in response to Menin-MLL inhibition. **(B)** Relative percentage of RFP+ transgene (H3.1WT or H3.1K4M) cells over time after transduction of MLL-AF9 cells treated with MI-503 or DMSO (mean±SEM, n=3 replicates, *P*-value calculated by Student's t-test, P < 0.001 = ***). **(C)** Expression of H3.1WT-RFP or H3.1K4M-RFP in mouse MLL-AF9 leukemia cells treated with DMSO or MI-503 was monitored by flow cytometry over time. **(D)** Immunoblot analysis of HA-tag from MLL-AF9 leukemia cells expressing H3.1WT-HA or H3.1K4M-HA and treated with DMSO or MI-503 for 6 days. **(E)** Immunoblot analysis of MLL4, UTX, HSP90 (loading control), H3K4me1, and total H3 (loading control) from MLL-AF9 leukemia cells expressing H3.1WT or H3.1K4M and treated with DMSO or MI-503 for 6 days.

A

Overlap Menin (DMSO) and UTX (MI-503) in MLL-AF9 leukemia

Rank	Motif	Name	*P*-value	% of Target	% of Background
1		**NFY**	$1e^{-130}$	44.97%	9.13%
2		Sp5	$1e^{-63}$	54.14%	23.85%
3		Sp1	$1e^{-50}$	32.69%	11.10%
4		KLF5	$1e^{-45}$	50.74%	25.05%
5		KLF14	$1e^{-41}$	59.47%	33.75%

B

Menin ChIP in NIH-3T3 fibroblasts

Rank	Motif	Name	*P*-value	% of Target	% of Background
1		CBF1	$1e^{-69}$	41.25%	1.86%
2		ARG80	$1e^{-69}$	40.62%	1.76%
3		TBX5	$1e^{-67}$	43.12%	2.35%
4		TEIL	$1e^{-64}$	42.50%	2.45%
5		HLH-2	$1e^{-62}$	40.00%	2.12%

C

UTX ChIP in NIH-3T3 fibroblasts

Rank	Motif	Name	*P*-value	% of Target	% of Background
1		VND	$1e^{-19}$	0.48%	0.00%
2		GFI1	$1e^{-16}$	0.43%	0.00%
3		RLR1	$1e^{-16}$	0.43%	0.00%
4		HOX2A	$1e^{-16}$	0.43%	0.00%
5		ARID5A	$1e^{-16}$	0.48%	0.00%

D

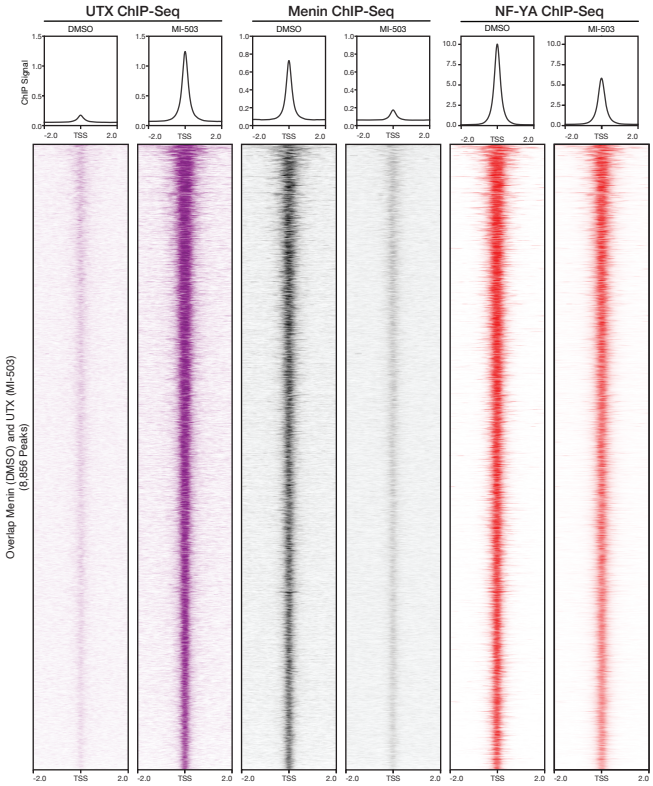

E

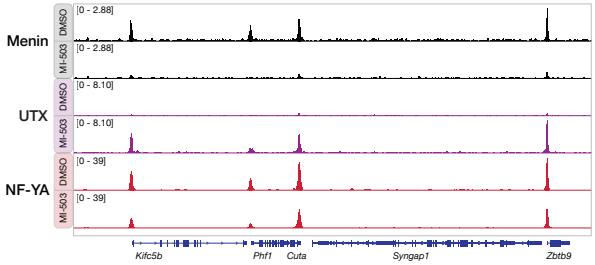

F

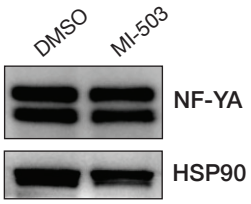

Extended Data Figure 12. NF-Y restricts chromatin occupancy of UTX at promoter regions. (A) Motif analysis of overlapping ChIP-Seq peaks between Menin (in DMSO) and UTX (in MI-503) in mouse MLL-AF9 leukemia cells. **(B)** Motif analysis of Menin ChIP-Seq peaks detected in NIH-3T3 mouse fibroblasts. **(C)** Motif analysis of UTX ChIP-Seq peaks detected in NIH-3T3 mouse fibroblasts. **(D)** Heatmaps displaying UTX (purple), Menin (black), and NF-YA (red) ChIP-Seq signals mapping to a 4-kb window around TSSs. Data is shown for DMSO and MI-503-treated cells for 96 hours. Metaplot represents the average ChIP-Seq signal for each protein at promoters. **(E)** Genome browser representation of ChIP-Seq normalized reads (average RPKM) for representative loci bound by Menin (black), UTX (purple), and NF-YA (red) in cells treated with DMSO or MI-503 for 96 hours. **(F)** Immunoblot analysis of NF-YA and HSP90 proteins (loading control) upon MI-503 treatment of mouse MLL-AF9 leukemia cells after 96 hours.

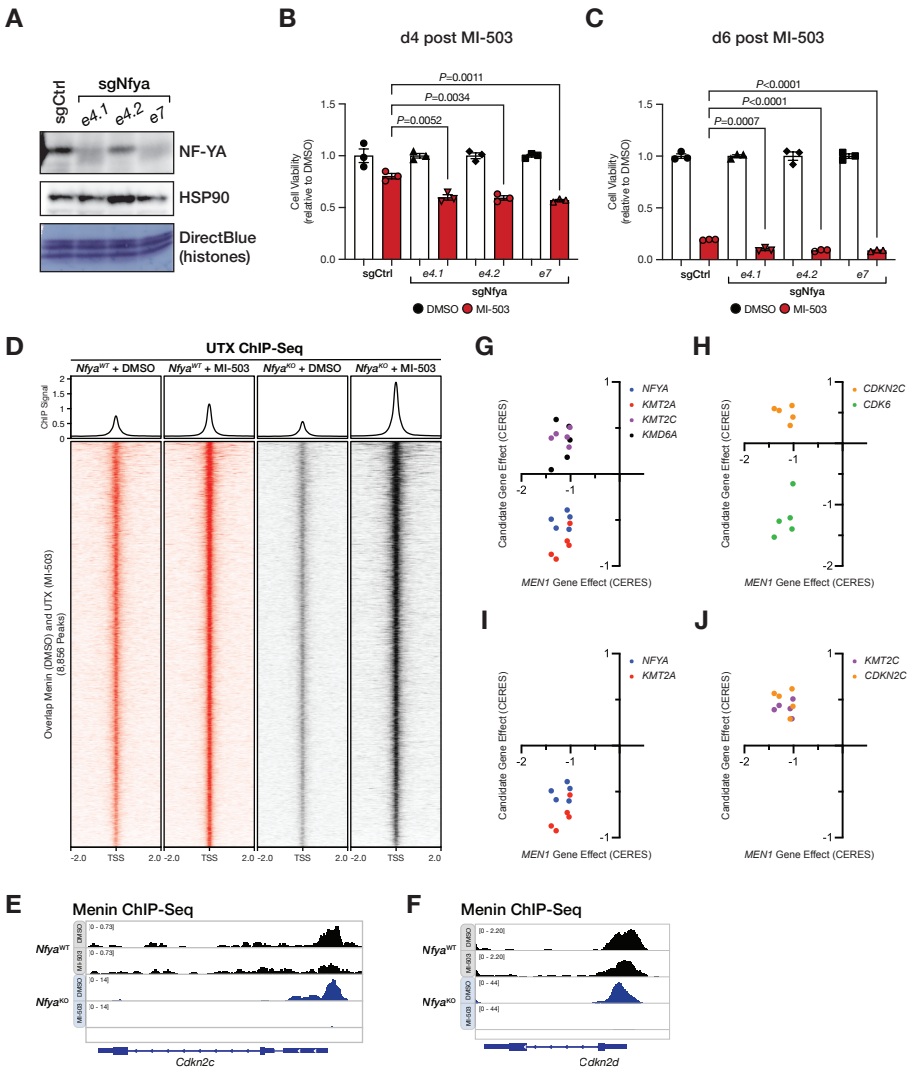

Extended Data Figure 13. NF-Y facilitates promoter regulation by Menin. (A) Immunoblot analysis of NF-YA and HSP90 proteins (loading control) in mouse MLL-AF9 leukemia cells transduced with a control sgRNA (sgCtrl) or three independent *Nfya*-targeting sgRNAs. Direct blue staining of histones (bottom) serves as an additional loading control. **(B)** Cell viability assay from cells treated with DMSO (vehicle, black) or MI-503 (red) after 4 days (mean±SEM, n=3 infection replicates, *P*-value calculated by Student's t-test). sgCtrl, control sgRNA targeting a non-genic region on chromosome 8. **(C)** Cell viability assay from cells treated with DMSO (vehicle, black) or MI-503 (red) after 6 days (mean±SEM, n=3 infection replicates, *P*-value calculated by Student's t-test). **(D)** Heatmaps displaying UTX ChIP-Seq signals mapping to a 4-kb window around TSSs in *Nfya*^{WT} (red) or *Nfya*^{KO} (black) MLL-AF9 leukemia cells treated with DMSO or MI-503 for 96 hours. Metaplot represents the average ChIP-Seq signal for each protein at promoters. **(E) - (F)** Genome browser representation of Menin ChIP-Seq normalized reads (average RPKM) for representative loci bound by Menin in *Nfya*^{WT} (black) or *Nfya*^{KO} (blue) MLL-AF9 leukemia cells treated with DMSO or MI-503 for 96 hours. **(G)** Co-essentiality scatter plot showing relationship between *MEN1* loss-of-function and dependency to *NFYA*, *MLL1* (*KMT2A*), *MLL3* (*KMT2C*), and *UTX* (*KDM6A*). **(H)** Co-essentiality scatter plot showing relationship between *MEN1* loss-of-function and dependency to *CDKN2C* and *CDK6*. **(I)** Co-essentiality scatter plot showing relationship between MEN1 loss-of-function and dependency to *NFYA* and *MLL1* (*KMT2A*) **(J)** Co-essentiality scatter plot showing relationship between MEN1 loss-of-function and dependency to *MLL3* (*KMT2C*) and *CDKN2C*.

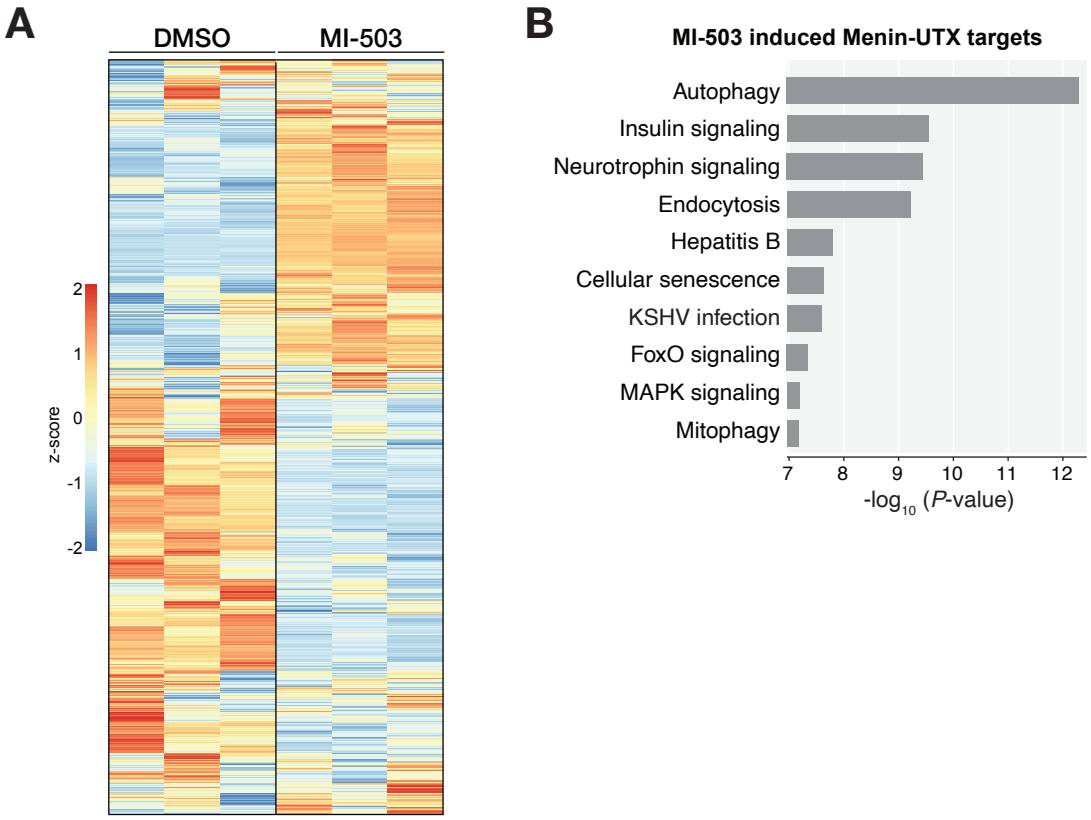

Extended Data Figure 14. Transcriptional assessment of MLL-AF9 leukemia cells treated with MI-503. (A) Heatmap showing differential gene expression in mouse MLL-AF9 leukemia cells treated with DMSO or MI-503 for 96 hours, as measured by RNA-Seq. **(B)** Gene ontology (GO) analysis of Menin-UTX targets using RNA-Seq data from MLL-AF9 leukemia cells treated with DMSO or MI-503 for 96 hours. Top 10 GO categories based on statistical significance are shown.

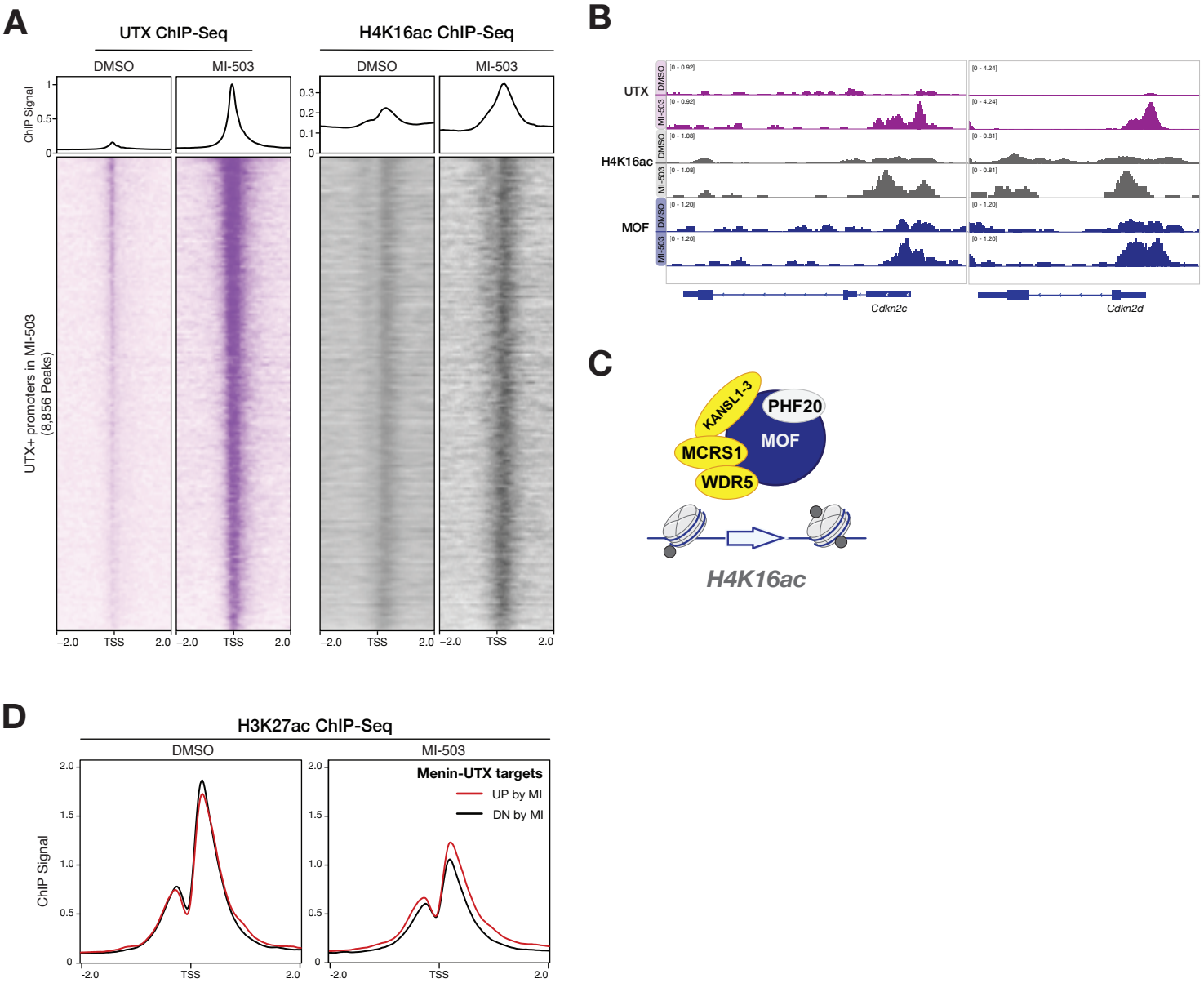

Extended Data Figure 15. Changes in histone acetylation accompany the Menin-UTX molecular switch upon Menin-MLL1 inhibition in human leukemia cells. (A) Heatmaps displaying UTX (purple) or H4K16ac (black) ChIP-Seq signals mapping to a 4-kb window around TSSs in MLL-AF9 leukemia cells treated with DMSO or MI-503 for 96 hours. Metaplot represents the average ChIP-Seq signal for each protein at promoters that are bound by UTX in mouse MLL-AF9 leukemia cells treated with MI-503 for 96 hours. **(B)** Genome browser representation of ChIP-Seq normalized reads (average RPKM) for UTX (purple), H4K16ac (grey), and MOF (blue) at Cdkn2c and Cdkn2d loci from MLL-AF9 cells treated with DMSO or MI-503 for 96 hours. **(C)** Schematic representation of the mammalian NSL histone acetyltransferase complex. Highlighted in blue is the enzymatic subunit of the complex, MOF. Yellow denotes other non-enzymatic subunits within the complex. **(D)** Average chromatin occupancy of H3K27ac at transcription start sites (TSS) +/-2kb of the Menin-UTX target genes. Signals corresponding to genes that are upregulated (red) or down-regulated (black) when cells are treated with MI-503 after 96 hours. RPM, reads per million.

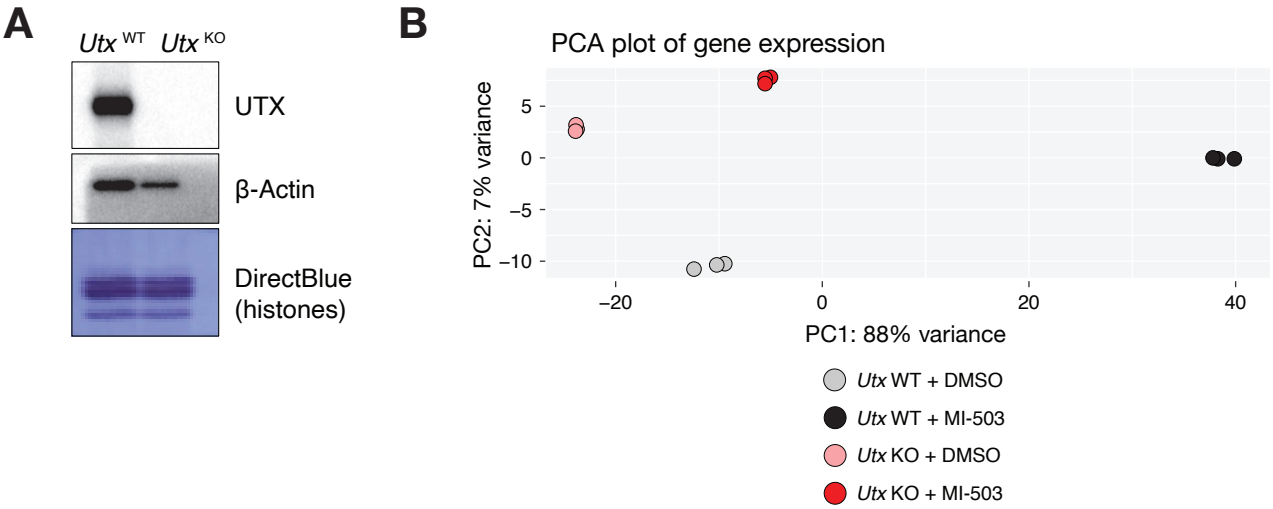

Extended Data Figure 16. Transcriptional assessment of Utx-deficient MLL-AF9 leukemia cells. (A) Immunoblot analysis of UTX and β-actin (loading control) from *Utx*^{WT} and *Utx*^{KO} mouse MLL-AF9 leukemia cells. **(B)** Principal component analysis (PCA) using RNA-Seq gene expression data from *Utx*^{WT} and *Utx*^{KO} cells treated with DMSO or MI-503 for 96 hours.

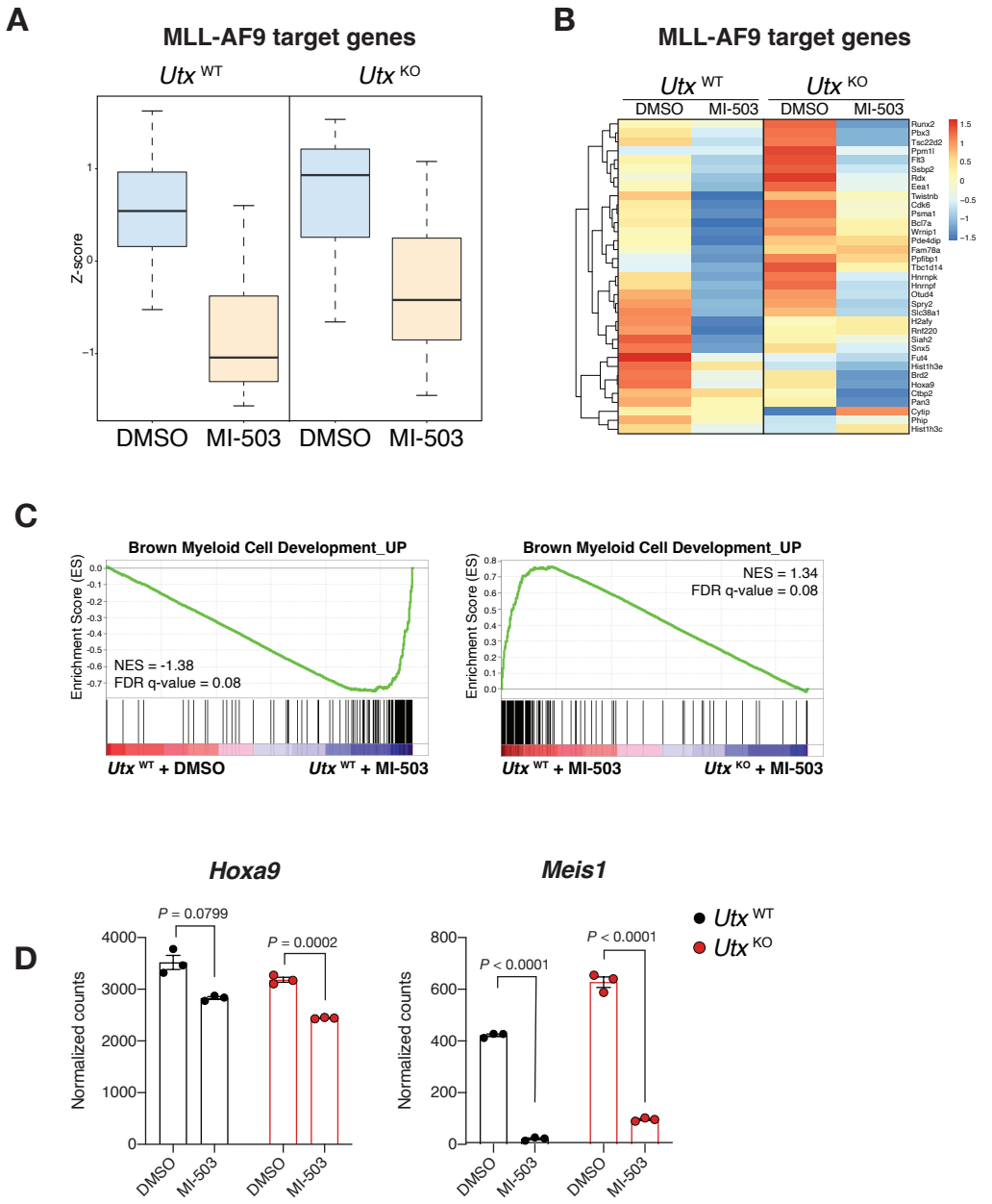

Extended Data Figure 17. MLL-AF9 target genes are not regulated by the Menin-UTX molecular switch. (A) Boxplot showing expression levels of MLL-AF9 target genes, which are suppressed by the MI-503 treatment after 96 hours. Expression levels are shown for *Utx*^{WT} (left panel) and *Utx*^{KO} (right panel) mouse leukemia cells. **(B)** Heatmap of Z-scores for expression of MLL-AF9 target genes from *Utx*^{WT} and *Utx*^{KO} leukemia cells treated with DMSO or MI-503 for 96 hours. **(C)** GSEA plots showing changes in regulation of myeloid cell differentiation in genes induced by MI-503 after 96 hours. FDR, false discovery rate; NES, normalized enrichment score. **(D)** Mean normalized read counts for MLL-AF9 target genes *Hoxa9* (left) and *Meis1* (right) across three RNA-Seq replicate samples from *Utx*^{WT} and *Utx*^{KO} leukemia cells treated with DMSO or MI-503 for 96 hours (mean±SEM, n=3 replicates, *P*-value calculated by Student's t-test).

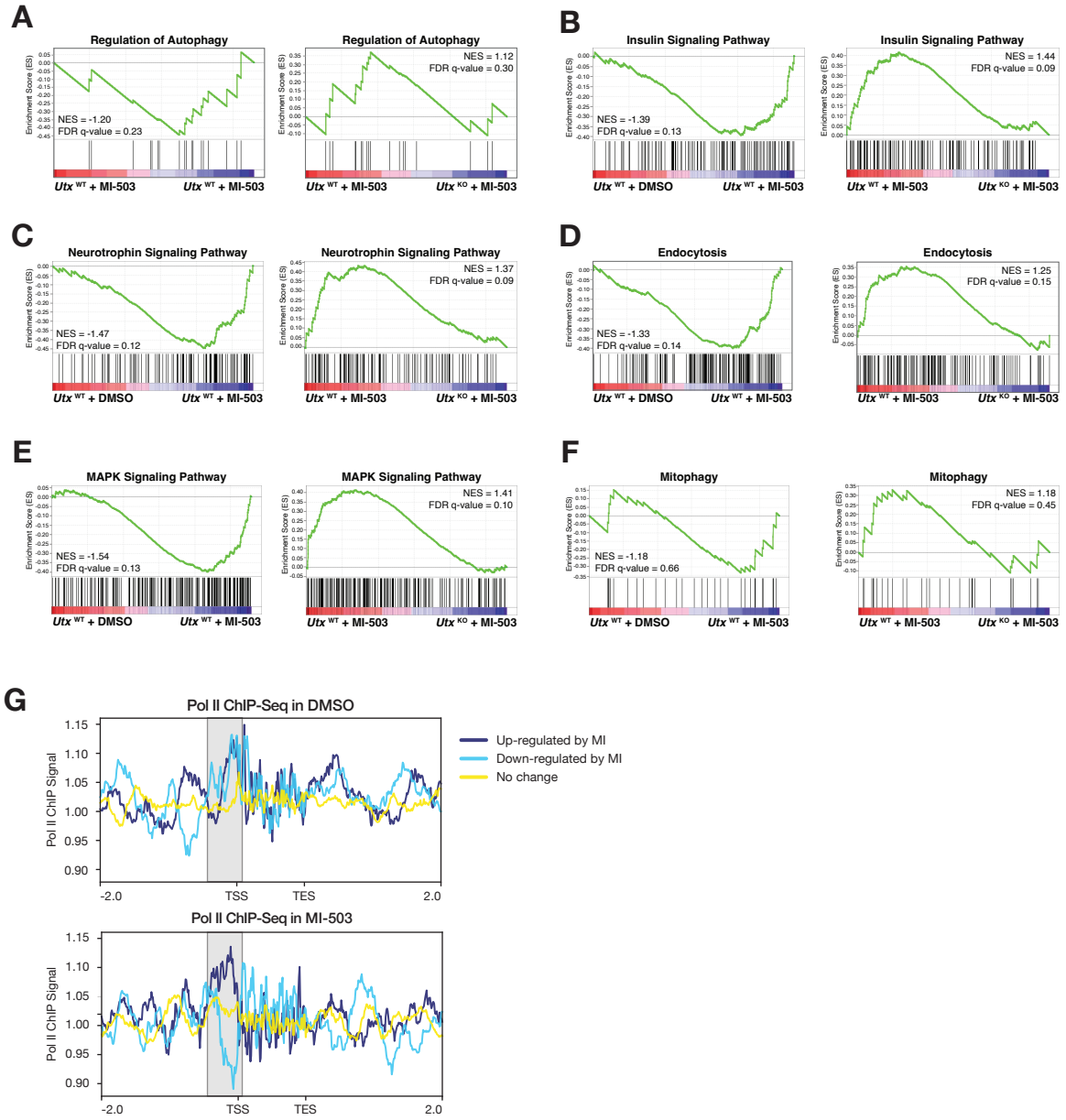

Extended Data Figure 18. Gene set enrichment analysis of Menin-UTX target genes. (A) GSEA plots showing changes in regulation of autophagy genes induced by MI-503 treatment after 96 hours. FDR, false discovery rate; NES, normalized enrichment score. **(B)** GSEA plots showing changes in insulin signaling pathway genes induced by MI-503 treatment after 96 hours. **(C)** GSEA plots showing changes in neurotrophin signaling pathway genes induced by MI-503 treatment after 96 hours. **(D)** GSEA plots showing changes in endocytosis genes induced by MI-503 treatment after 96 hours. **(E)** GSEA plots showing changes in MAPK signaling pathway genes induced by MI-503 treatment after 96 hours. **(F)** GSEA plots showing changes in mitophagy genes induced by MI-503 treatment after 96 hours. **(G)** RNA Pol II ChIP-Seq signal determined for senescence and cell-cycle arrest-associated genes that are Menin-UTX targets.

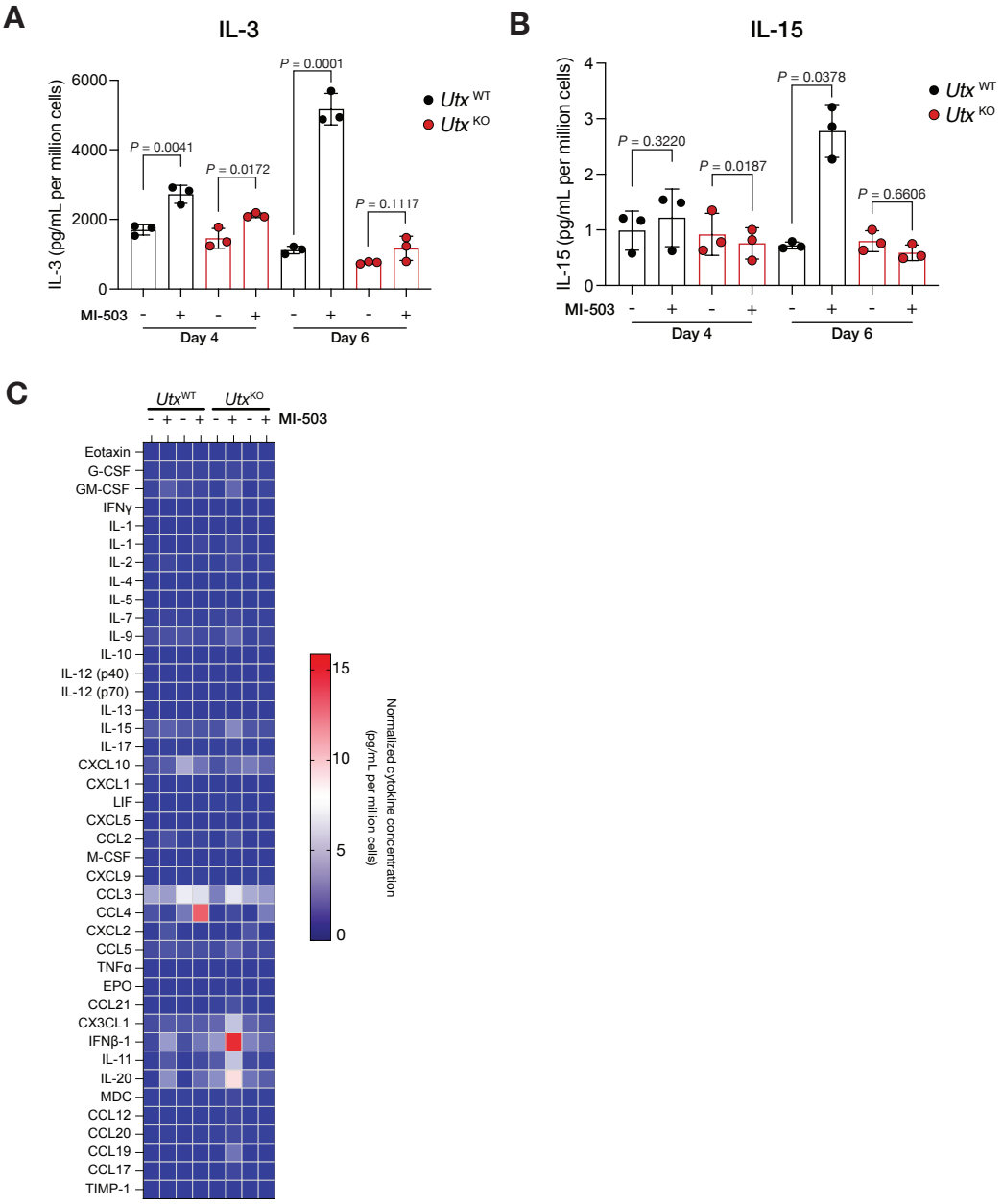

Extended Data Figure 19. MLL3/4-UTX-dependent induction of SASP cytokines upon Menin-MLL inhibition. (A) Secreted levels of IL-3 in *Utx*^{WT} and *Utx*^{KO} MLL-AF9 leukemia cells treated with Menin inhibitor (MI-503) or vehicle (DMSO) after four or six days. Data are quantified as pg/mL of secreted cytokine per million cells (mean±SEM, n=3 replicates, *P*-value calculated by Student's t-test). **(B)** Secreted levels of IL-15 in *Utx*^{WT} and *Utx*^{KO} MLL-AF9 leukemia cells treated with Menin inhibitor (MI-503) or vehicle (DMSO) after four or six days. Data are quantified as pg/mL of secreted cytokine per million cells (mean±SEM, n=3 replicates, *P*-value calculated by Student's t-test). **(C)** Heatmap of cytokine array results from *Utx*^{WT} and *Utx*^{KO} MLL-AF9 leukemia cells treated with Menin inhibitor (MI-503) or vehicle (DMSO) after four or six days. Data are quantified as pg/mL of secreted cytokine per million cells and represent the mean of three biological replicates. Note that the very high levels of IFNβ-1 secretion relative to the rest of the cytokines measured affect the dynamic range of data visualization.

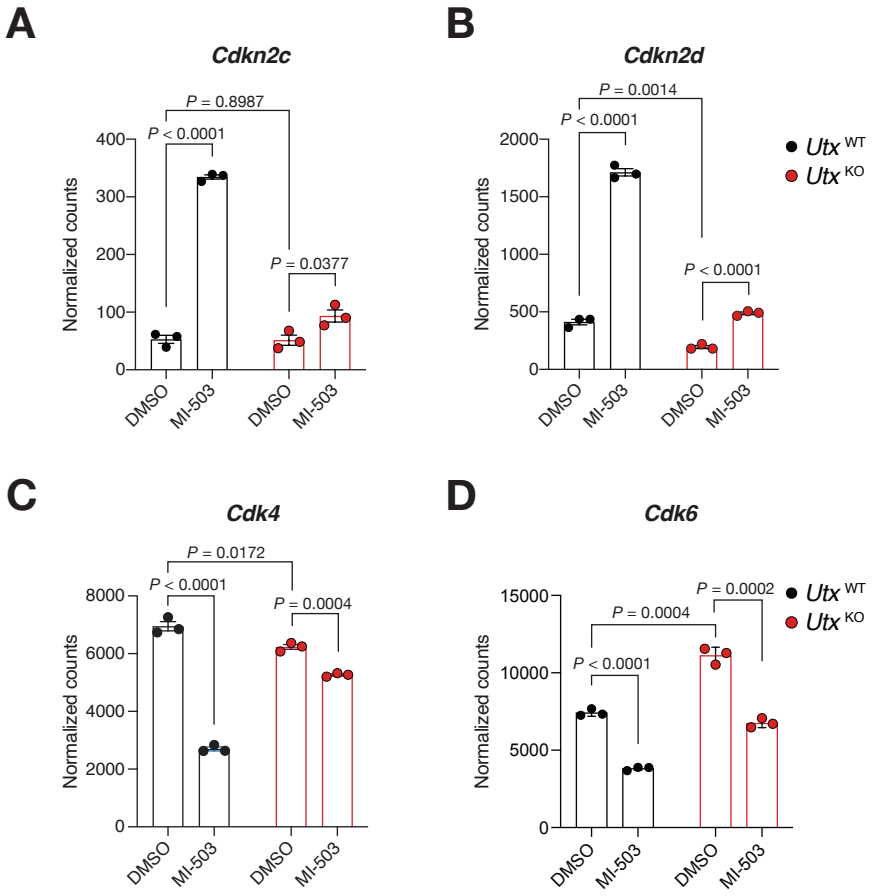

Extended Data Figure 20. Induction of the Menin-UTX molecular switch regulates expression of the CDK inhibitors *Cdkn2c/d*. (A) - (B) Mean normalized read counts of the cyclin-dependent kinases inhibitors, *Cdkn2c* and *Cdkn2d*, across three RNA-Seq replicate samples from *Utx*^{WT} (black) and *Utx*^{KO} (red) leukemia cells treated with DMSO or MI-503 for 96 hours. **(C) - (D)** Mean normalized read counts of the cyclin-dependent kinases, *Cdk4* and *Cdk6*, across three RNA-Seq replicate samples from *Utx*^{WT} (black) and *Utx*^{KO} (red) leukemia cells treated with DMSO or MI-503 for 96 hours.

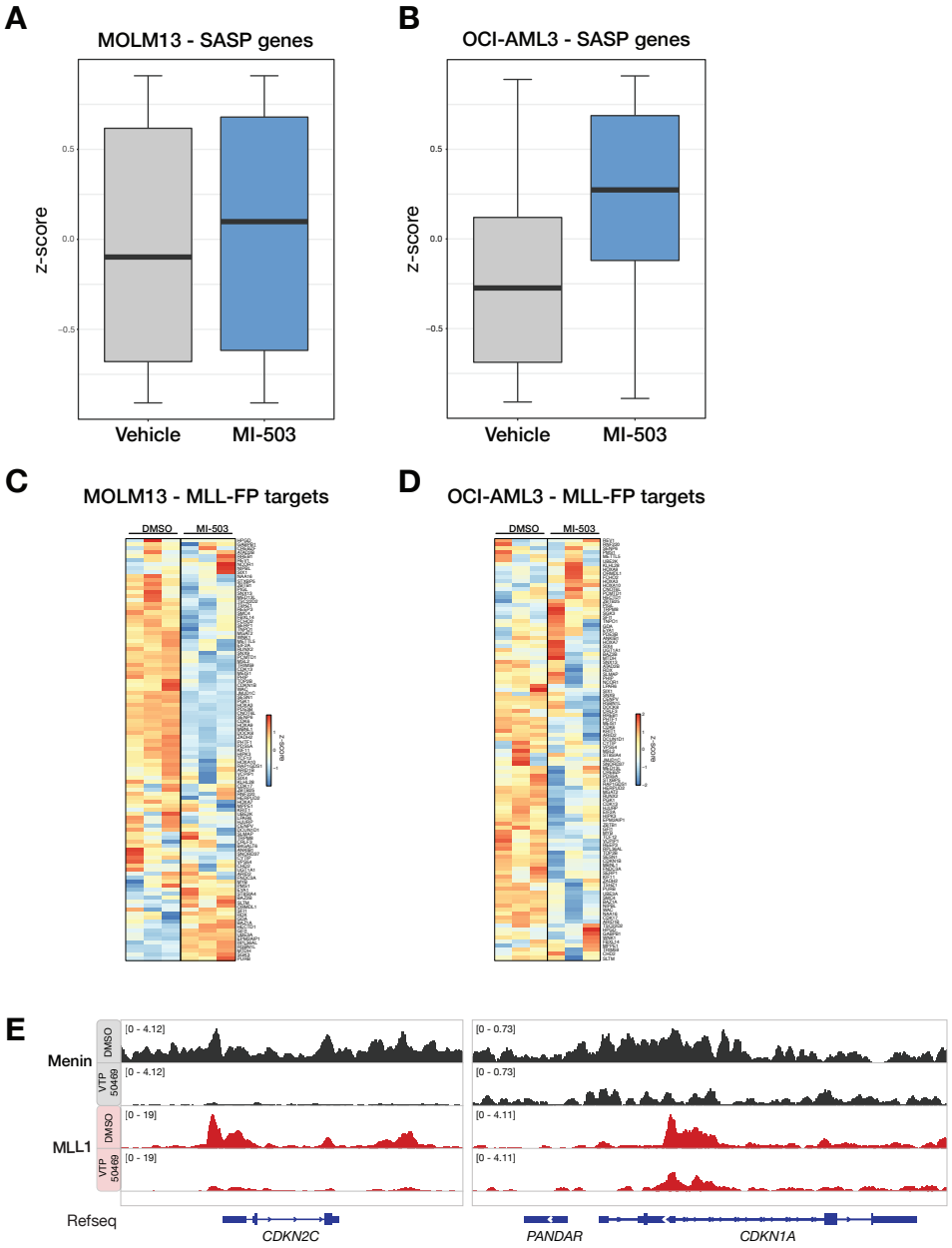

Extended Data Figure 21. Induction of the Menin-UTX molecular switch upon Menin-MLL1 inhibition in human leukemia cells. (A) Boxplot showing expression levels of SASP genes in MOLM13 human leukemia cells treated with DMSO or MI-503 for 96 hours. **(B)** Boxplot showing expression levels of SASP genes in OCI-AML3 human leukemia cells treated with DMSO or MI-503 for 96 hours. **(C)** Heatmap of Z-scores for expression of MLL-FP target genes from MOLM13 human leukemia cells treated with DMSO or MI-503 for 96 hours. **(D)** Heatmap of Z-scores for expression of MLL-FP target genes from OCI-AML3 human leukemia cells treated with DMSO or MI-503 for 96 hours. **(E)** Genome browser representation of ChIP-Seq normalized reads (average RPKM) for Menin (black) or MLL1 (red) at *CDKN2C* and *CDKN1A* loci from MOLM13 human leukemia cells treated with DMSO or VTP-50469 for 7 days.

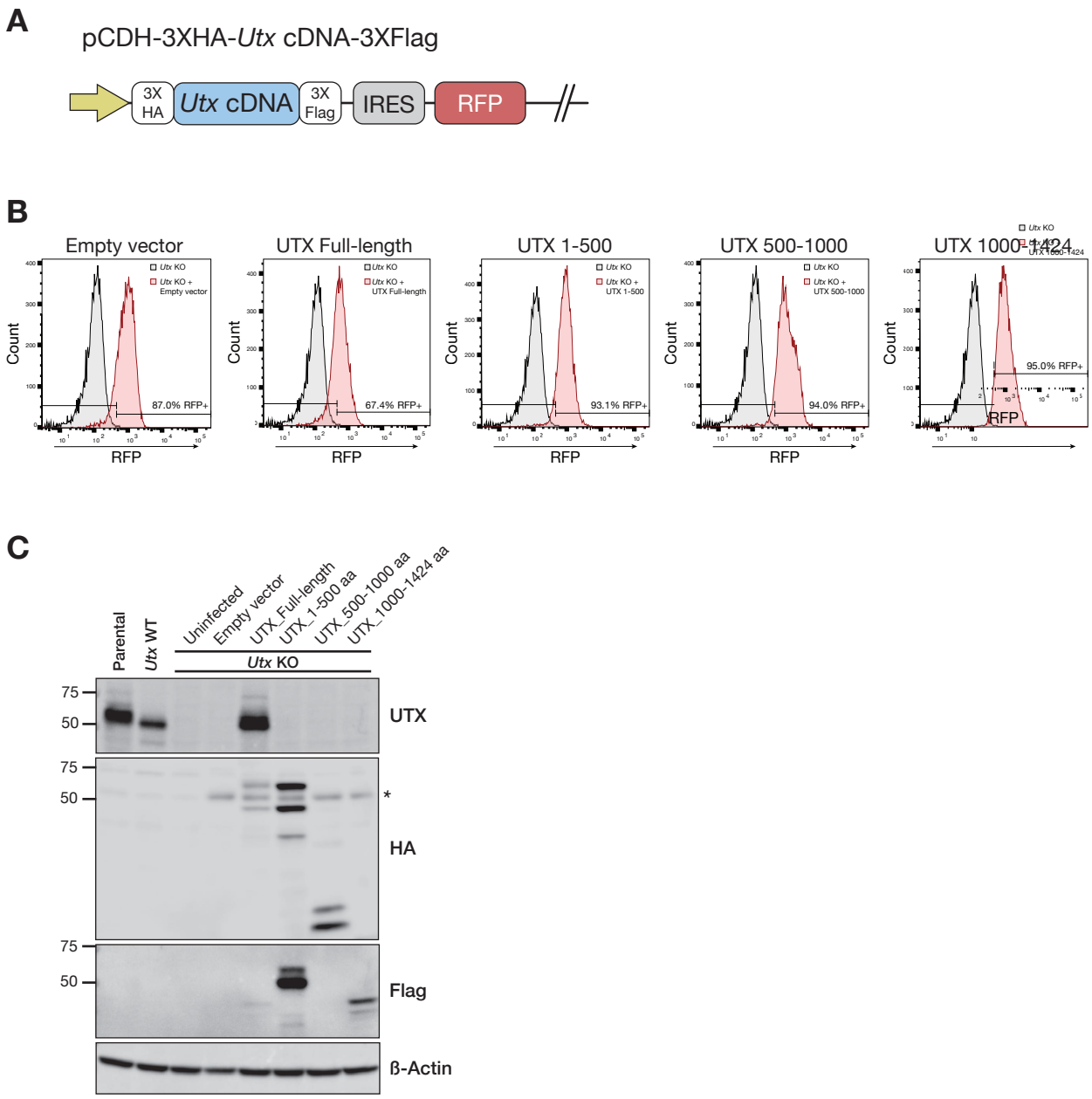

Extended Data Figure 22. Expression of UTX truncations in MLL-AF9 *Utx*-null leukemia cells. **(A)** Representation of the lentiviral vector used to stably co-express N-terminal HA-/C-terminal-Flag-tagged *Utx* cDNAs and the fluorescent protein RFP. **(B)** Flow cytometry plots showing RFP expression of the different mouse MLL-AF9 leukemia cell lines generated with the *Utx* truncations. **(C)** Immunoblotting validation of expression of the different *Utx* truncations in mouse MLL-AF9 leukemia cells.

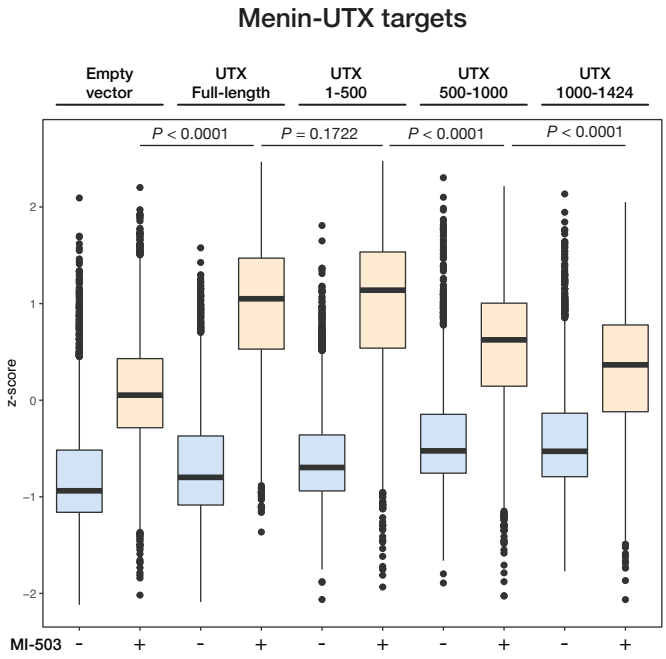

Extended Data Figure 23. Transcriptional characterization of the different Utx truncations in mouse MLL-AF9 leukemia cells. Boxplot showing expression levels of Menin-UTX target genes in mouse MLL-AF9 leukemia cells treated with DMSO or MI-503 for 96 hours.

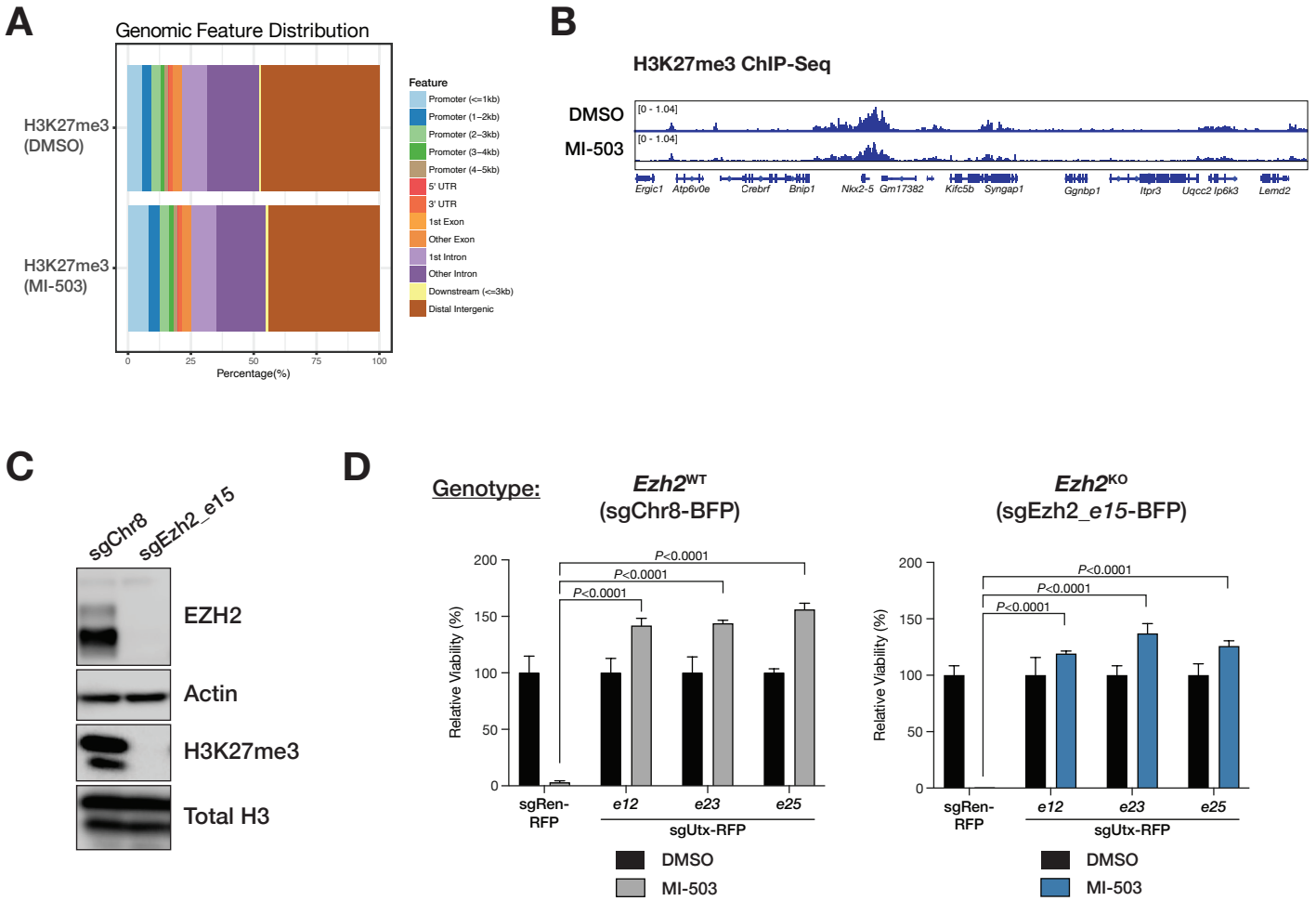

Extended Data Figure 24. UTX-dependent phenotypes are not associated with global changes in H3K27 methylation. (A) Genomic distribution of H3K27me3 ChIP-Seq peaks from mouse leukemia cells treated with DMSO or MI-503 for 96 hours. **(B)** Genome browser representation of ChIP-Seq normalized reads (average RPKM) for H3K27me3 from MLL-AF9 cells treated with DMSO or MI-503 for 96 hours. **(C)** Immunoblot analysis of EZH2, β-actin (loading control), H3K27me3, and total H3 (loading control) from *Ezh2*^{WT} and *Ezh2*^{KO} mouse MLL-AF9 leukemia cells. **(D)** Cell viability assay from mouse *Ezh2*^{WT} (left) and *Ezh2*^{KO} (right) MLL-AF9 leukemia cells treated with DMSO (vehicle, black) or MI-503 (red) after 96 hours (mean±SEM, n=3 infection replicates, *P*-value calculated by Student's t-test). sgCtrl, control sgRNA targeting a non-genic region on chromosome 8.

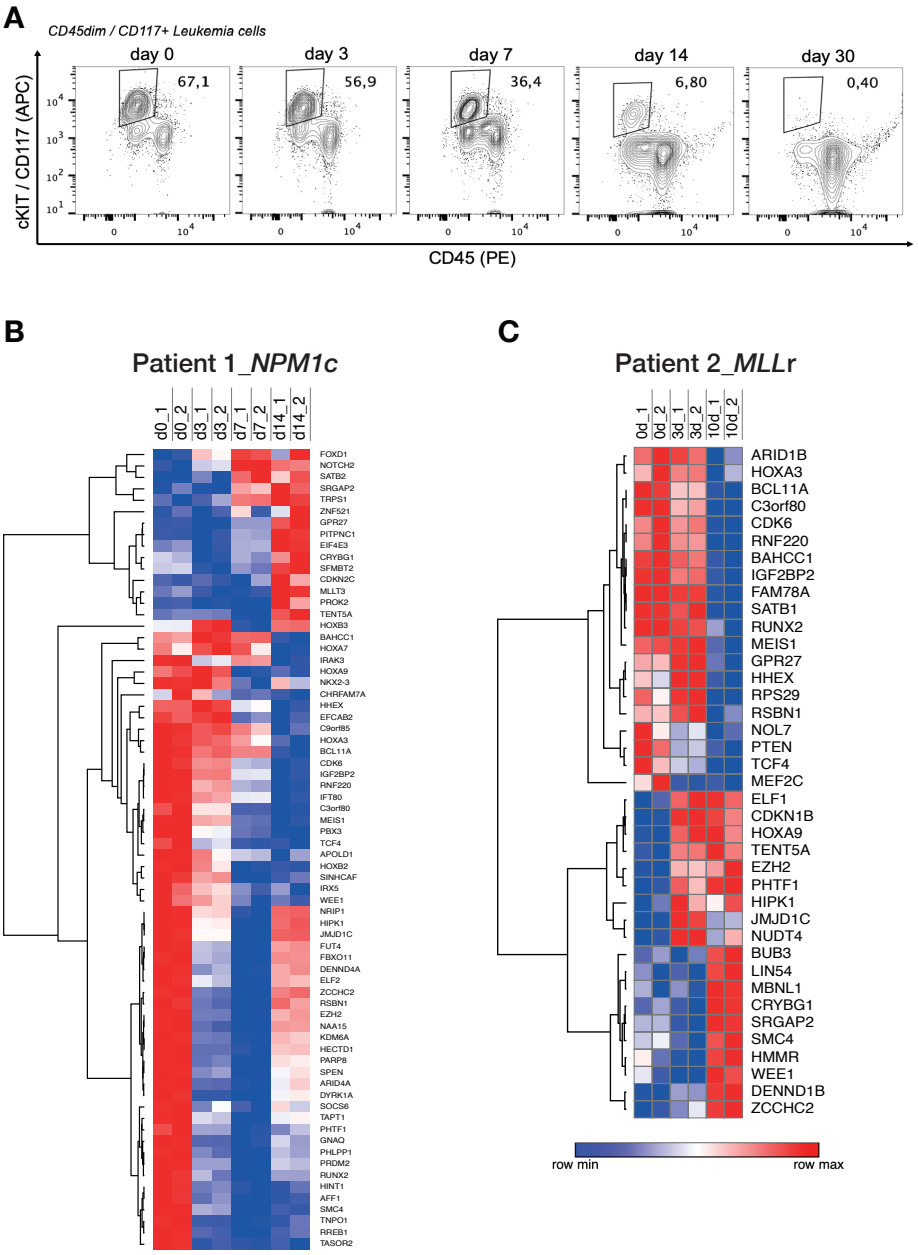

Extended Data Figure 25. Primary human AML samples from patients participating in the Syndax Phase I Menin-MLL inhibitor trial. (A) Immunophenotyping of primary human AML cells isolated from Patient 1 (*NPM1c* mutant AML). **(B)** Heatmap representation of Z-scores from longitudinal gene expression analysis of AML cells derived from Patient 1 (*NPM1c* mutant AML) treated with SNDX-5613. **(C)** Heatmap representation of Z-scores from longitudinal gene expression analysis of AML cells derived from Patient 2 (*MLL*-rearranged AML) treated with SNDX-5613.

A

PDX Sample	*MLL*-r	*MLL3* status
DFAM68555	MLL-AF9	wild-type
MSK042D	MLL-AF4	mutant

B

PDX sample	DNA sequencing	*MLL3* (*KMT2C*) alleles present
MLL-r, *MLL3*-WT (DFAM68555)	**GGT --> Gly (G)** 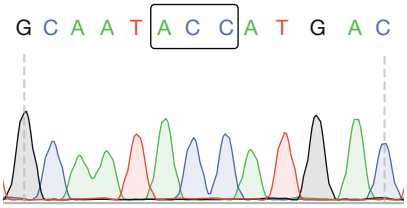	Two wild-type alleles (homozygote): 5'-GGT-3' (Position: 12,556-12,558)
MLL-r, *MLL3*-Mut (MSK042D)	**GGT --> Gly (G)** **GAT --> Asp (D)** 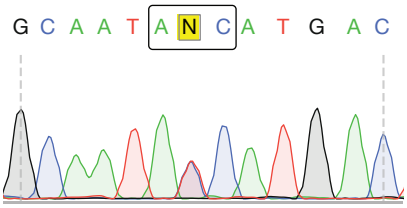	One wild-type + one mutant alleles (heterozygote): 5'-GGT-3' + 5'-GAT-3'

Extended Data Figure 26. Modeling of Menin-MLL1 inhibitor response in patient-derived xenografts. (A) Characteristics of PDX samples analyzed in this study. **(B)** Targeted sequencing validation of *MLL3* status in PDX samples.

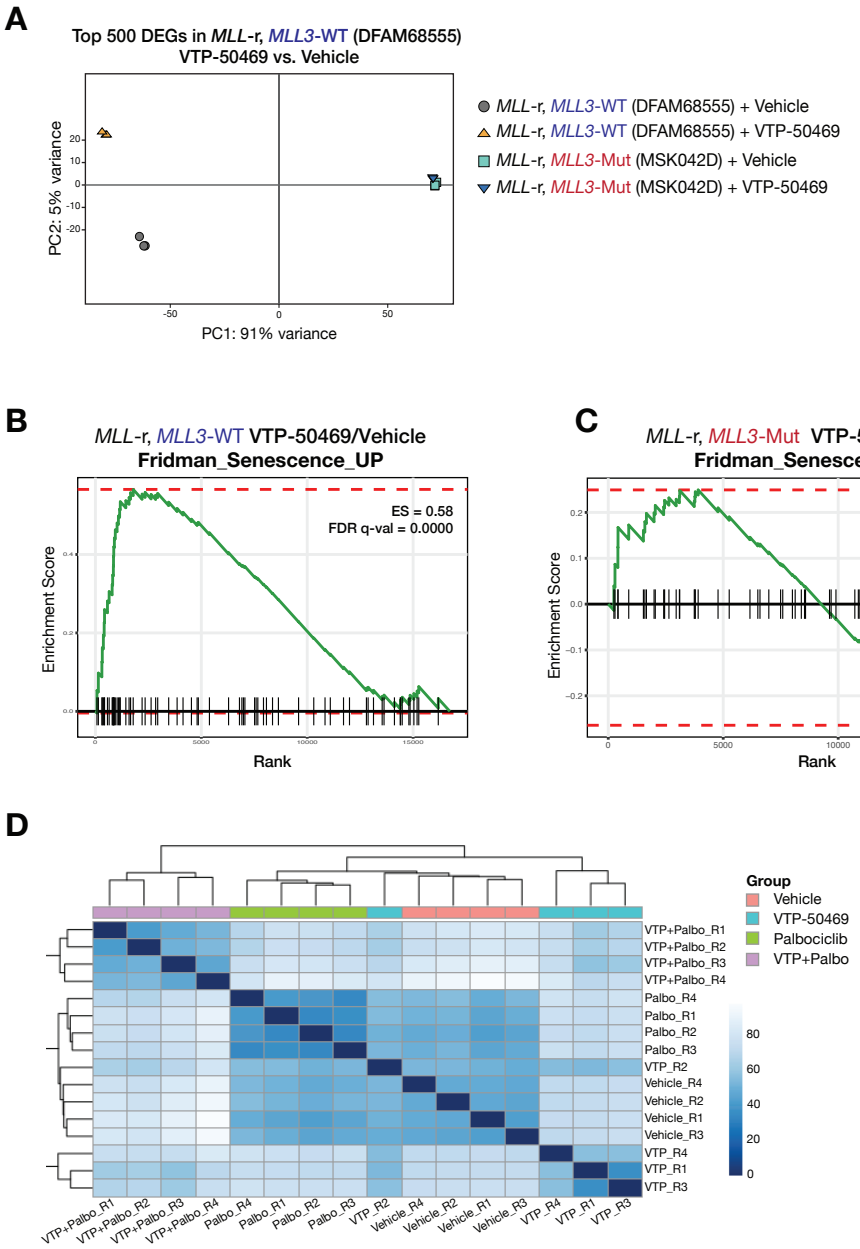

Extended Data Figure 27. Transcriptional characterization of Menin-MLL1 inhibitor response in patient-derived xenografts. (A) PCA using RNA-Seq gene expression data obtained from *MLL3*-WT (DFAM68555) and *MLL3*-Mutant (MSK042D) PDX samples treated with DMSO or VTP-50469. PCA was performed using the top 500 differentially-expressed genes upon treatment of MLL3-WT PDXs with VTP-50469. Note that *MLL3*-Mutant PDX samples are virtually overlapping independent of the condition, suggesting that the induction of the Menin-UTX molecular switch is impaired in the context of *MLL3* mutation. **(B)** GSEA showing that Menin-MLL inhibition using VTP-50469 leads to induction of cellular senescence in *MLL3*-WT PDX. **(C)** GSEA showing that Menin-MLL inhibition using VTP-50469 fails to induce cellular senescence in *MLL3*-Mutant PDX. **(D)** Distance matrix for expression of all genes from RNA-Seq data obtained from *MLL3*-Mutant (MSK042D) PDX samples treated with DMSO, VTP-50469, Palbociclib, or a combination of the two inhibitors.